# Laser-driven nonlinear cluster dynamics

Th. Fennel, K.-H. Meiwes-Broer, and J. Tiggesbäumker

*Institut für Physik, Universität Rostock, D-18051 Rostock, Germany*

P.-G. Reinhard

*Institut für Theoretische Physik, Universität Erlangen, D-91058 Erlangen, Germany*

P. M. Dinh and E. Suraud

*Laboratoire de Physique Théorique, Université Paul Sabatier, CNRS, F-31062 Toulouse Cedex, France*

(Published 8 June 2010)

Laser excitation of nanometer-sized atomic and molecular clusters offers various opportunities to explore and control ultrafast many-particle dynamics. Whereas weak laser fields allow the analysis of photoionization, excited-state relaxation, and structural modifications on these finite quantum systems, large-amplitude collective electron motion and Coulomb explosion can be induced with intense laser pulses. This review provides an overview of key phenomena arising from laser-cluster interactions with focus on nonlinear optical excitations and discusses the underlying processes according to the current understanding. A general survey covers basic cluster properties and excitation mechanisms relevant for laser-driven cluster dynamics. Then, after an excursion in theoretical and experimental methods, results for single-photon and multiphoton excitations are reviewed with emphasis on signatures from time- and angular-resolved photoemission. A key issue of this review is the broad spectrum of phenomena arising from clusters exposed to strong fields, where the interaction with the laser pulse creates short-lived and dense nanoplasmas. The implications for technical developments such as the controlled generation of ion, electron, and radiation pulses will be addressed along with corresponding examples. Finally, future prospects of laser-cluster research as well as experimental and theoretical challenges are discussed.

DOI: 10.1103/RevModPhys.82.1793

PACS number(s): 36.40.−c, 52.50.Jm

## CONTENTS



 

## I. INTRODUCTION

Clusters of atoms and molecules frequently appear as a novel state of matter on the nanometer scale. For example, different types of bonding or various structural and chemical features can be realized within the same material by just changing the particle size. The opportunity to vary, almost at will, the number of atoms in the clusters thus offers a unique avenue to explore the organization and properties of matter from a fundamental point of view (Haberland, 1994; Martin, 1996; Sugano and Koizumi, 1998; Alonso, 2006). This also applies to optical phenomena arising from small particles, e.g., due to surface plasmons (Kreibig and Vollmer, 1995), which fascinated scientists for a long time (Rayleigh, 1899; Mie, 1908). Today's lasers open an even more exciting perspective of cluster science, i.e., the opportunity to steer and resolve ultrafast dynamics on the nanoscale.

Due to the progress in laser technology (Keller, 2003; Rullière, 2005), well-controlled short and intense laser pulses can be routinely delivered these days. This opens the door to explore light-induced dynamical phenomena far beyond the analysis of ground-state properties. For example, the real-time analysis of nuclear and even electron motion becomes possible, as in the case of molecules or atoms (Zewail, 1994; Corkum and Krausz, 2007). When applied to clusters, short pulses controlled in amplitude and phase allow one to drive and resolve ion and electron dynamics on their natural time scales and under extreme conditions. For instance, electronic relaxation processes or the time evolution of collective modes can be studied with laser-excited clusters. As a more violent scenario, strong-field exposure transforms clusters into well-isolated nanometer-sized plasmas, with interesting prospects for pulsed particle, radiation, or even neutron sources. With the advent of vacuum ultraviolet (VUV) free electron lasers (FELs) (Feldhaus *et al.*, 2005), coherent multiphoton inner-shell excitations are accessible with intense femtosecond pulses. Inspired by such opportunities, the subject of laser-cluster interactions has spawned sustained interdisciplinary activities and experienced enormous developments over the last two decades. It holds the promise to deliver unprecedented insights into the nature of light-matter interactions in complex systems and stimulated challenging efforts in experiment and theory.

In this review we focus on the nonlinear response behavior of clusters subject to laser fields, concentrating on the nonrelativistic intensity regime. It is our aim, in close connection between theory and experiment, to discuss signatures and mechanisms for multiphoton as well as for strong-field excitations. Nevertheless, even single-photon absorption can lead to complex dynamics, e.g., due to electron correlations, structural transitions, or competing electronic decay channels. As a result, the response can go beyond a simple and direct mapping of ground-state properties. In any case, pronounced nonlinearities emerge when multiphoton absorption is involved. As a typical example within the still photon-dominated regime, above-threshold ionization (ATI) can be observed with clusters, showing additional finite-size and many-particle effects when compared to atomic systems. At higher intensities in the so-called field-dominated regime, the immediate excitation of several electrons and laser-driven collisions induce avalanche processes of highly nonperturbative nature. As a surprising feature, clusters efficiently absorb intense laser radiation (Ditmire *et al.*, 1997), with an energy capture per atom much higher than for atoms or bulk material (Batani *et al.*, 2001). Moreover, strong-field laser-cluster interactions lead to the emission of fast electrons (Springate *et al.*, 2003), multiply charged ions (Köller *et al.*, 1999), and high-energy photons (McPherson *et al.*, 1994), documenting the excitation of core electrons. When compared to atoms, the appearance intensities for these products are strongly reduced with clusters. The discussion of the underlying dynamics and appropriate theoretical treatments is the central topic of this review.

Different aspects of laser-excited clusters have previously been reviewed, such as the electronic structure of simple metal clusters (Brack, 1993; de Heer, 1993; Ekardt, 1999), low- and moderate-field dynamics (Reinhard and Suraud, 2003), ionization mechanisms in strong optical and VUV laser fields (Saalmann *et al.*, 2006), and excitations with ultraintense pulses (Krainov and Smirnov, 2002). The current paper aims to deliver a present-day view on cluster dynamics in optical laser fields, with emphasis on the strong-field regime, and incorporates recent findings regarding angular-resolved emission, electron acceleration, and processes behind very highly charged ions. Moreover, routes will be reviewed to resolve the cluster response in time by varying the pulse duration or using dual-pulse excitations. Special features of this review are the presentation of experimental and theoretical methods and the attempt of closely combining theory and experiment.

The text is organized as follows. Section II offers a quick outlook of the topic and discusses basic physical mechanisms. It provides some basic elementary stepping stones on which to build an understanding of the topic. Section III is a survey of available theoretical tools for describing cluster dynamics and tries to show how the various approaches may be linked together in terms of regimes for which they were primarily developed. Section IV focuses on experimental techniques, discussing cluster production and laser sources as a starter. Emphasis is put on the detection of emitted particles. Section V concentrates on the intermediate intensity domain in which photons still count. In this regime experiments have revealed detailed insight into the quantum nature of clusters and allow one to explore the onset of nonlinear behaviors. Section VI discusses the main topic of the paper and describes highly nonlinear strong-field induced dynamics where quantum effects are partially wiped out. After a survey of initial or original results in the field, a detailed analysis of systematic trends and present day more elaborate approaches are presented. This concerns in particular differential cross sections and time-resolved analyses. Finally, Sec. VII provides an outlook and proposes future directions of research in the

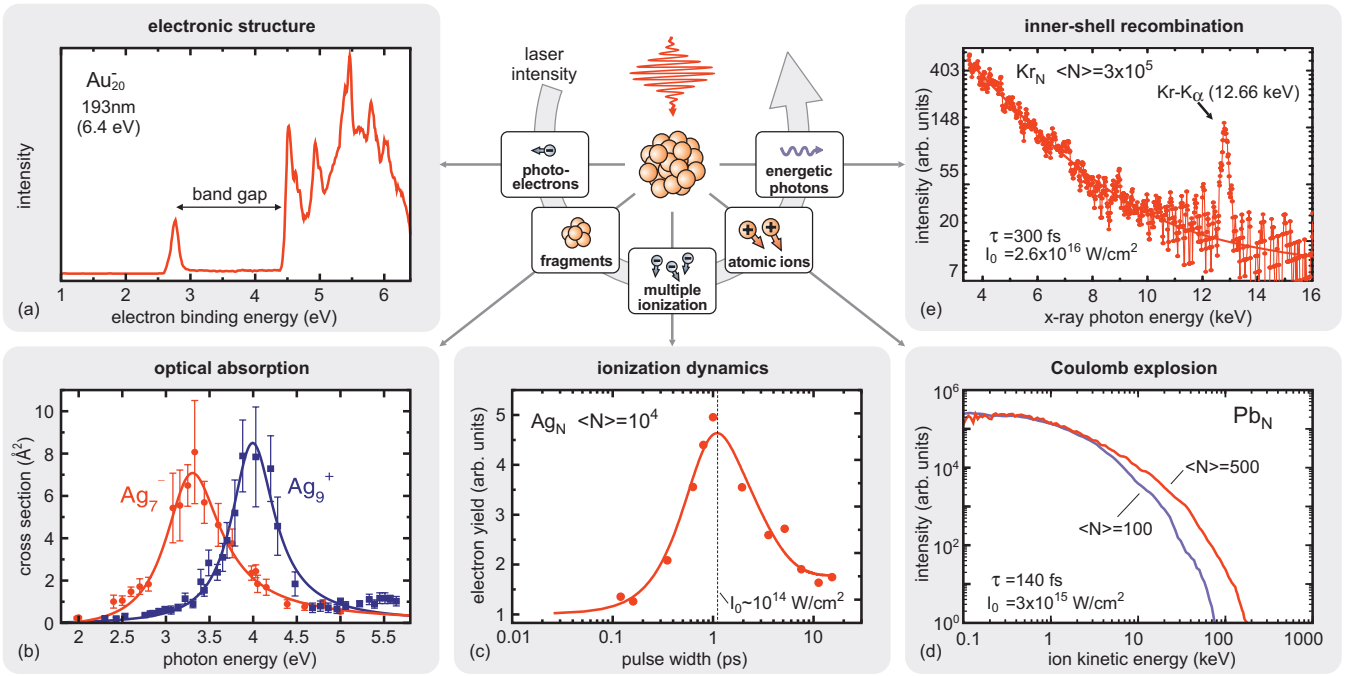


FIG. 1. (Color) Five decay channels of laser-excited clusters aside with properties or processes that may be resolved from their analysis (see text). (a) Electronic structure of negatively charged gold clusters with 20 atoms ($Au_{20}^-$) extracted from the photoelectron spectrum. From Li, Li, *et al.*, 2003. (b) Optical absorption of $Ag_7^-$ and $Ag_9^+$ as determined by photofragmentation. Adapted from Tiggesbäumker *et al.*, 1993, 1996. (c) Ionization dynamics of $Ag_N$ in intense laser pulses resolved by measuring the total electron yield as a function of pulse width at fixed pulse energy (Radcliffe, 2004); (d) Coulomb explosion of $Pb_N$ analyzed by recoil energy spectroscopy of emitted atomic ions. From Teuber *et al.*, 2001. (e) Inner-shell recombination in strongly excited krypton clusters measured by x-ray spectroscopy. From Issac *et al.*, 2004.

field. We discuss in particular the prospects of laser developments either in terms of pulse shaping of today's sources or by considering new types of lasers such as the x-ray free electron lasers (XFEL). We also comment on embedded and deposited clusters, avenues for high-energy particle acceleration with clusters, and point out some future challenges for theory.

## II. GENERAL SURVEY OF LASER-CLUSTER INTERACTIONS

Laser irradiation of clusters allows the investigation of a broad spectrum of dynamical processes, ranging from single-photon driven ionization to the strong-field-induced explosion of a nanometer-scaled plasma. Irrespective of the regime under consideration, the absence of dissipation into substrate material offers a clean analysis of reaction products, i.e., electrons, ions, cluster fragments, as well as photons. Depending on the cluster material and the chosen laser intensity, quite different properties and response mechanisms can be probed, as discussed throughout this review. Exemplarily, Fig. 1 shows a few response channels and properties that may be analyzed and can be viewed as a rough guideline.

As an example for electron emission in the single-photon regime, Fig. 1(a) shows an ultraviolet photoelectron spectroscopy (UPS) result on $Au_{20}^-$ obtained with low intensity laser excitation. The photoelectron energy spectrum images the electronic structure, i.e., binding energies and spectral occupation densities of single electron states, and contains comprehensive information on the system. The large band gap in Fig. 1(a), for example, reflects the high stability of the tetrahedral $Au_{20}$ (Li, Li, *et al.*, 2003). Besides structure analysis, photoelectron spectroscopy (PES) is a powerful tool for monitoring excited states and reaction dynamics (see Sec. V.A).

Laser-induced fragmentation may be analyzed to determine optical properties. Figure 1(b) displays the optical absorption cross section of size-selected silver clusters measured by photofragmentation (Tiggesbäumker *et al.*, 1993, 1996). The spectra exhibit a pronounced resonance, i.e., the Mie surface plasmon (see Secs. II.A and II.C). Collective excitations, as prime examples for multielectron effects, are not only relevant in the single-photon limit but are also important for the cluster response in the multiphoton and strong-field regimes as well (see Secs. V.B.1 and VI.B).

With increasing laser intensity, nonlinear and feedback effects begin to severely influence the cluster response, such as the electron emission. Figure 1(c) shows an example for larger silver clusters, where the measured total electron yield, i.e., the average cluster ionization, is plotted as a function of the temporal width of the laser pulse (Radcliffe, 2004). The strong variation with pulse duration reveals a pronounced ionization dynamics that can be related to the interplay of collective plasma heating and ultrafast relaxation of the ionic structure (see Sec. VI.B.1). In addition, as a result of

TABLE I. Basic atom, dimer, and bulk properties for four typical cluster materials. Bulk properties for carbon correspond to graphite which is close to the $C_{60}$ cluster and carbon nanotubes. The critical laser intensity is estimated with Eq. (6) (see Sec. II.C). The Wigner-Seitz radius $r_s$ characterizes the atomic density.

| | Na | Ag | C | Ar |
|---|---|---|---|---|
| Atom | | | | |
| Ionization potential[a] (eV) | 5.14 | 7.58 | 11.26 | 15.8 |
| $\varepsilon_{val}-\varepsilon_{core}$[a] (eV) | 26.0 | 53.9 | 8.21 | 232.6 |
| Valence level | 3*s* | 5*s* | 2*p* | 3*p* |
| Core level | 2*p* | 4*p* | 2*s* | 2*p* |
| Lowest dipole excitation[a] (eV) | 2.1 | 3.66 | 7.48 | 11.62 |
| Critical laser intensity (W/cm$^2$) | $3\times10^{12}$ | $1\times10^{13}$ | $6\times10^{13}$ | $2\times10^{14}$ |
| Dimer | | | | |
| Bond length[b,c,d] (Å) | 3.08 | 2.53 | 1.20 | 3.83 |
| Dissociation energy[b,d] (eV) | 0.76 | 1.69 | 6.3 | 0.012 |
| Bulk | | | | |
| Work function[b] (eV) | 2.75 | 4.26 | 4.8 | 15.8 |
| Cohesive energy[b] (eV) | 1.12 | 2.95 | 7.8 | 0.08 |
| Wigner-Seitz radius[b] (Å) | 2.10 | 1.59 | 1.21 | 2.21 |

[a]NIST.
[b]Weast (1988).
[c]Verma *et al.* (1983) and Beutel *et al.* (1993).
[d]Hirschfelder *et al.* (1954).

high charging of cluster constituents, atomic ions are accelerated to high kinetic energies by Coulomb explosion (see Secs. VI.A.2 and VI.A.3). Examples for ion energy spectra from intense laser excitation of lead clusters are shown in Fig. 1(d) (Teuber *et al.*, 2001) and document kinetic energies of up to hundreds of keV as well as a cluster size effect in the recoil energy. Within the strong-field-induced excitation process a hot and highly ionized nanoplasma is formed. Evidence for the presence of energetic electrons is given by the creation of inner-shell atomic vacancies in the cluster constituents, the recombination of which can be monitored by analyzing the extreme ultraviolet (EUV) and x-ray emission (see Secs. VI.A.4 and VI.B.2). The example in Fig. 1(e) shows energetic $K\alpha$ radiation at 12.6 keV resulting from irradiation of krypton clusters (Issac *et al.*, 2004). A detailed analysis of the EUV and x-ray emission can be used for monitoring ion charge state distributions.

The examples highlighted in Fig. 1 illustrate the wide spectrum of phenomena resulting from laser irradiation of clusters. Before analyzing particular response effects in more detail, a few basic facts about "protagonists" of such processes, i.e., clusters and lasers, will be recalled. In the following we furthermore remind basic mechanisms of energy absorption and ionization relying on both individual atomic and cooperative processes and provide a rough classification of different coupling regimes.

### A. Basic cluster properties and time scales

Cluster properties are strongly dependent on the type of their constituents. We consider four typical cluster materials: Na as a simple metal, Ag as a noble metal, C as a covalent material, and Ar as a rare-gas system. Table I recalls a few basic facts of these elements, e.g., the electronic core and valence levels and corresponding energy gaps. Since cluster properties are by nature also size dependent (number of constituents between a few and several thousand atoms), atomic, dimer, and bulk values are stated, which fix typical orders of magnitude.

For a given element, the atomic ionization potential (IP) and the bulk work function (WF) indicate the electronic stability of a corresponding atomic cluster with respect to optical excitation. Both IP and WF follow a similar trend over the given materials, i.e., increase from Na to Ar. Typically, metal clusters can be ionized or excited much easier, i.e., with lower photon energies or less intense radiation, than covalent or rare-gas systems. This trend is also reflected in the first atomic dipole transition (lowest dipole excitation). The IP further indicates the ionization behavior in strong fields as it determines the critical laser intensity required for atomic barrier suppression (see Sec. II.C for details).

Structural stability is not necessarily linked to that of the electronic system. This becomes evident after comparing dimer dissociation energies or bulk cohesive energies with the IP's, e.g., for C with Ar. Note that the bulk cohesive energies roughly reflect the binding energy per atom of the cluster, while the atomic Wigner-Seitz radius $r_s$ may be used to approximate the cluster radius ($R_{cl}\approx r_s N^{1/3}$). The values for the dimer bond length indicate typical interatomic distances.

In the visible and ultraviolet spectral range the optical response is mainly determined by valence electrons. In

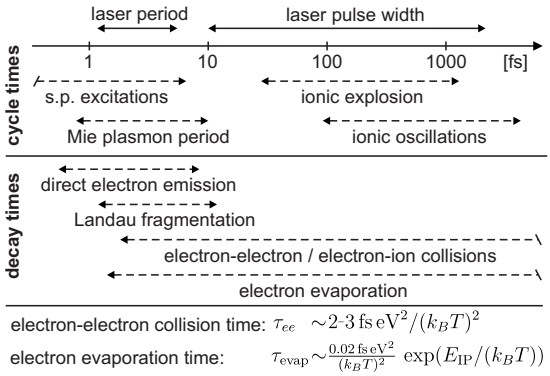


FIG. 2. Typical time scales for the dynamics, with sodium clusters as a prototype. On the top the ranges associated to fs lasers are depicted. Processes related to motion (cycle times) and lifetimes due to relaxation (decay times) are also indicated. Approximate expressions for electron-electron collisions ($\tau_{ee}$) and electron evaporation ($\tau_{\mathrm{evap}}$) are given at the bottom.

metal clusters, electron delocalization leads to a strong resonance, the Mie surface plasmon, as a unique feature of finite objects with subwavelength dimension. The resonance corresponds to a collective oscillation of the whole valence electron cloud against the ionic background. When considering schematically a cluster as a metallic drop (Mie, 1908), the Mie surface plasmon frequency of a neutral system can be given by (Brack, 1993; de Heer, 1993)

$$\omega_{\mathrm{Mie}} = e(4\pi\epsilon_0 m_e r_s^3)^{-1/2}, \tag{1}$$

with $r_s$ the effective Wigner-Seitz radius of conduction electrons, $e$ the elementary charge, $\epsilon_0$ the permittivity of vacuum, and $m_e$ the electron mass. For small $Na_N$, for example, the plasmon energy is $\hbar\omega_{\mathrm{Mie}} \approx 2.8$ eV (Schmidt and Haberland, 1999), while Eq. (1) predicts a value of 3.4 eV. This indicates that the actual Mie response depends on further details (finite size effects, geometrical structure, excitation, net charge, etc.), but Eq. (1) already provides a reasonable order of magnitude sufficient for many forthcoming discussions.

For considering reaction pathways and energy dissipation it is useful to compare relevant time scales. To that end we consider Na as a typical example for a metal cluster. Figure 2 provides a schematic overview over times related to laser characteristics, electronic and ionic motion, and lifetimes for relaxation processes. For the moment we ignore the extremely short times associated with core electrons. They certainly play an important role in intense laser fields but are usually dealt with in terms of simplified rate equations (see, e.g., Sec. III.C). The pulse duration of optical lasers may be varied over a wide range extending from fs to ps or even ns. We focus here on pulse widths of the order a few tens to a few hundred fs.

The shortest time scales in Fig. 2 are related to the electronic motion. The Mie plasmon period as the most basic one is of the order of fs [cf. Eq. (1)]. In the same range, but with a wider span from sub-fs to several fs, are cycle times for other single-particle excitations and direct electron escape, i.e., single-particle excitation into the continuum. Somewhat slower is the plasmon decay due to Landau fragmentation in analogy to Landau damping known from plasma physics (Lifschitz and Pitajewski, 1988). In clusters, Landau fragmentation results from the coupling of plasmons with energetically close single-particle excitations. Viewed in coordinate space, the fragmentation corresponds to collisions of electrons with the anharmonic potential at the cluster surface. The Landau relaxation time $\tau_L$ depends on cluster size and has, e.g., for $Na_N$, its lowest values for $N \approx 1000$ (Babst and Reinhard, 1997). For $N > 1000$ it can be estimated from the time between collisions of an electron with the cluster boundary ("wall friction") as $\tau_L \approx (r_s N^{1/3})/v_F$, where $v_F = (\hbar/m)(9\pi/4)^{1/3}/r_s$ is the Fermi velocity (Yannouleas *et al.*, 1990). For $N < 1000$, however, $\tau_L$ increases for smaller $N$ due to the reduced level density. The relaxation time $\tau_{ei}$ describes damping due to electron-ion collisions. The relaxation time is strongly temperature dependent (~30 fs for Na at 273 K), scales as $\tau_{ei} \propto T^{-1}$ at low temperature due to electron-phonon scattering (Ashcroft and Mermin, 1976), and follows $\tau_{ei} \propto T^{3/2}$ in a high-temperature plasma (Spitzer, 1956).

The most widely varying times are related to the collisional damping from electron-electron collisions and thermal electron evaporation. Both strongly depend on the internal excitation of the cluster, which may be characterized by an electronic temperature $T$. A simple connection between internal excitation energy per electron $\epsilon^* = E^*/N$ and temperature can be established by the Fermi gas model. For $k_BT \ll \epsilon_F$, $T$ can be estimated as $k_BT = 2(\epsilon_F\epsilon^*)^{1/2}/\pi$, where $\epsilon_F = \hbar^2(9\pi^2/4)^{2/3}/(2m_e r_s^2)$ is the Fermi energy. For the particular case of sodium at bulk density, we have $k_BT = (1.28\ \mathrm{eV} \times \epsilon^*)^{1/2}$. Electron-electron collisions are the key mechanism for electronic thermalization. The $T^{-2}$ law for the corresponding collision time in Fig. 2 is known from Fermi liquid theory (Kadanoff and Baym, 1962; Pines and Nozières, 1966). For low $T$, collisions are strongly suppressed due to the Pauli blocking of energetically available electronic states. At high $T$, electron collisions become competitive with Landau damping and sometimes even the dominating damping mechanism. Electron-electron collisions can be described with semiclassical models (see Sec. III.B.3).

An even more dramatic temperature (or excitation energy) dependence appears for the electron evaporation time, whose trend is dominated by the exponential factor $\exp(E_{\mathrm{IP}}/k_BT)$, where $E_{\mathrm{IP}}$ denotes the value of the ionization potential. The more detailed expression for the evaporation time given in Fig. 2 is based on the Weisskopf formulas (Weisskopf, 1937), $\tau_{\mathrm{evap}} \approx \pi\hbar^3/(8m_e r_s^2 N^{2/3})(k_BT)^{-2} \exp(E_{\mathrm{IP}}/k_BT)$, and a cluster size of $N = 100$. For this size the crossing point $\tau_{ee} \approx \tau_{\mathrm{evap}}$ occurs at a temperature of $k_BT = 0.7$ eV. This corresponds to a hot (nano)plasma where finite electron clouds are practically an unstable evaporative ensemble. In general, electron evaporation represents an efficient

cooling mechanism for highly excited clusters.

Ionic motion spans a wide range of long time scales. Vibrations, which may be measured by Raman scattering [see, e.g., Portales *et al.* (2001)], are typically in the meV regime, i.e., have cycle times of 100 fs to 1 ps. In small clusters, ionic vibrations can induce satellites in the optical spectrum (Ellert *et al.*, 2002; Fehrer *et al.*, 2006). Strong laser irradiation usually leads to large amplitude ionic motion and cluster explosion due to Coulomb pressure generated by ionization and thermal excitation. Electron-ion coupling due to Coulomb pressure proceeds at the electronic time scale, i.e., within a few fs. The effect on the ions, however, develops at slower scale, typically beyond 100 fs, due to the large ionic mass. The time scale of Coulomb explosion can be estimated by considering sudden ionization of cluster constituents to an average atomic charge state $\langle q\rangle$. In this case the cluster expands homogenously and doubles its radius after $\tau_{\mathrm{doub}} \approx 2.3(\sqrt{2\pi\epsilon_0}/e)m_{\mathrm{ion}}^{1/2} r_s^{3/2}/\langle q\rangle$, where $m_{\mathrm{ion}}$ is the ion mass and $r_s$ is the initial atomic Wigner-Seitz radius. For $Na_N$ this yields $\tau_{\mathrm{doub}} \approx 63\ \mathrm{fs}/\langle q\rangle$. As a consequence, strong ionization drives clusters apart quite rapidly, accompanied with strong changes in the optical properties. Corresponding signatures can be analyzed with pump-probe techniques (see Sec. VI.B). For excitations that do not induce explosion, the time scale of electron-ion thermalization reaches up to the ns range (Fehrer *et al.*, 2006). Ionic relaxation is even slower; e.g., thermal emission of a monomer can easily last $\mu$s.

As shown above, cluster dynamics comprises a large span of time scales, making their theoretical description a great challenge. Ionic motion may require a simulation time up to several ps while electronic times scale down to a small fraction of a fs have to be resolved. Theoretical approaches for a corresponding description are discussed in Sec. III. Relaxation processes at the ns scale, however, require more phenomenological approaches.

### B. Intense laser fields: Key parameters

We proceed with a summary of basic facts and key parameters of intense laser fields. In the nonrelativistic regime, laser pulses acting on atoms, molecules, or clusters can usually be described as a homogenous time-dependent electric field of the form

$$\vec{\mathcal{E}}(t) = \mathbf{e}_z \mathcal{E}_0 f(t)\cos[\omega_{\mathrm{las}} t + \varphi(t)], \tag{2}$$

where $\mathbf{e}_z$ denotes linear polarization in the $z$ direction, $\mathcal{E}_0$ is the peak field strength, $f(t)$ is the normalized temporal field envelope of the pulse, $\hbar\omega_{\mathrm{las}}$ is the photon energy of the carrier, and $\varphi(t)$ is an additional temporal phase. Any other polarization (linear or circular) can be described by superposition. The phase can be written as $\varphi(t) = \varphi_{ce} + (\beta/2)t^2 + (\gamma/3)t^3 + O(t^4)$, where $\varphi_{ce}$ is the carrier-envelope phase, $\beta$ and $\gamma$ denote linear and quadratic chirps, and the last term indicates higher-order chirp contributions. Furthermore, the instantaneous frequency reads $\omega_{\mathrm{inst}}(t) = \omega_{\mathrm{las}} + \dot{\varphi}(t)$ and the instantaneous pulse intensity is given by $I(t) = I_0 f(t)^2$, where $I_0 = c\epsilon_0 \mathcal{E}_0^2/2$ is the peak intensity and $c$ is the vacuum speed of light. Typically, the pulse duration $\tau$ is given as the full width at half maximum (FWHM) of the temporal intensity profile. A common temporal pulse profile is a Gaussian field envelope, which then reads $f(t) = \exp(-2\ln 2 t^2/\tau^2)$. In absence of chirp, the bandwidth $\Delta\omega$ (FWHM) of the corresponding spectral intensity profile is related to the temporal pulse width via the time-bandwidth product $\tau_0 \Delta\omega/2\pi = 0.441$. Increasing the pulse duration by dispersive pulse stretching to $\tau$ induces a linear chirp of $\beta = \pm 4\ln 2\sqrt{s^2-1}/s^2\tau_0^2$, where $s = \tau/\tau_0 \geqslant 1$ is the stretching factor with respect to the bandwidth-limited pulse. The chirp direction (up or down) depends on the sign of the group velocity dispersion of the optical element. However, it should be noted that the exact forms of $f(t)$ and $\varphi(t)$ are not always easy to ascertain experimentally. Nonetheless, the pulse duration can nowadays be varied very flexibly over a wide range, e.g., between a few fs up to ns for optical lasers.

In the dipole approximation and using the length gauge, the coupling of the pulse to an electron at position $\mathbf{r}$ can be described by an external potential

$$V_{\mathrm{las}}(\mathbf{r},t) = e\vec{\mathcal{E}}(t)\cdot\mathbf{r}. \tag{3}$$

Therefore the system size has to be well below the wavelength $\lambda = 2\pi c/\omega_{\mathrm{las}}$, which is well justified for nm clusters and excitation in the optical domain ($\lambda \sim 1\ \mu$m). The dipole approximation becomes questionable for UV photons and very large clusters but will be valid in most cases considered.

To classify coupling regimes it is useful to consider a freely oscillating electron (pure quiver motion, no drift velocity) in the laser field. The cycle averaged kinetic energy defines the ponderomotive potential, which reads

$$U_p = \frac{e^2\mathcal{E}_0^2}{4m_e\omega_{\mathrm{las}}^2} \tag{4}$$

at the pulse peak. The ponderomotive potential can be expressed more conveniently by $U_p = 9.33\times10^{-14}\ \mathrm{eV} \times I_0[\mathrm{W/cm^2}](\lambda[\mu\mathrm{m}])^2$. Figure 3 displays the dependence of $U_p$ in the frequency-intensity plane along with the characteristic parameter regions which can be realized with high intensity laser sources. As a rule of thumb, regimes of photon- and field-dominated coupling are separated by a $U_p$ that equals the typical electron binding energy in the considered system, as schematically shown in Fig. 3. This condition is related to the Keldysh parameter, as discussed in Sec. II.C. Figure 3 further shows the enormous flexibility of optical lasers to produce high intensities up to the relativistic limit where $U_p$ becomes non-negligible compared to the electron rest energy. In this review, however, we focus on intensities for which relativistic effects and the magnetic field of the pulses may be neglected. Compared to optical lasers, VUV-FELs and XFELs cover a fundamentally different regime, i.e., photon-driven dynamics at high intensities due to the low ponderomotive potential [see Saalmann *et al.* (2006) and Sec. VII.B].

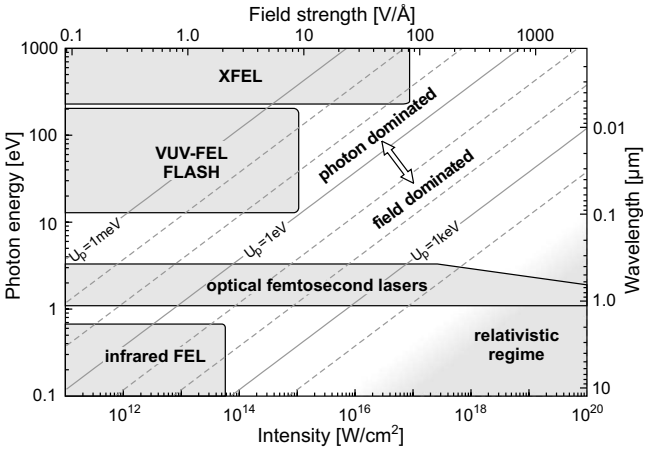


FIG. 3. Intensity-frequency regimes attainable with different high intensity laser systems (shaded blocks). Corresponding wavelengths and electric field strengths are displayed on the additional scales. Lines indicate regions of constant ponderomotive potential $U_p$. The transition from photon- to field-dominated coupling is given by $U_p = E_{IP}$, as schematically depicted for an IP of a few eVs. VUV-FEL, vacuum ultraviolet free electron laser; XFEL, x-ray free electron laser.

### C. Ionization and heating mechanisms in clusters

Several basic ionization and energy absorption mechanisms are of relevance for describing laser irradiated particles and will be introduced below. Departing from concepts for atomic and molecular systems we move on to cooperative and collective effects which stem from the many-particle nature of clusters.

On the atomic level, two fundamentally different photoionization processes may be considered. The first is vertical excitation of a bound electron by single-photon or multiphoton absorption in a rapidly oscillating laser field [see multiphoton ionization (MPI) in Fig. 4(a)]. This mechanism proceeds over many laser cycles and prevails for weak and moderate fields in the so-called perturbative domain. A MPI process of order $\nu$ is characterized by the reaction rate $\Gamma_\nu = \sigma_\nu I^\nu$, where $\sigma_\nu$ is the corresponding cross section. MPI, which may be enhanced when intermediate resonant states are available, can promote electrons far beyond the continuum threshold, leading to characteristic peaks separated by units of the photon energy in the electron energy spectrum. This effect, termed ATI, is well known from atoms and also appears in clusters (see Sec. V.B.2). The second mechanism is optical field ionization (OFI). Here the laser acts as a quasistationary electric field. For sufficiently strong fields, bound electrons tunnel through the barrier emerging from the combined potential of the residual $q$-charged ion and the laser field, i.e., $V(x) \propto -a/|z| - z$, with $a = qe^2/4\pi\epsilon_0\mathcal{E}_0$. This is schematically shown in Fig. 4(a) (dashed curve). The probability for atomic tunneling ionization can be described by the well-known Ammosov-Delone-Krainov (ADK) rates (Ammosov *et al.*, 1986).

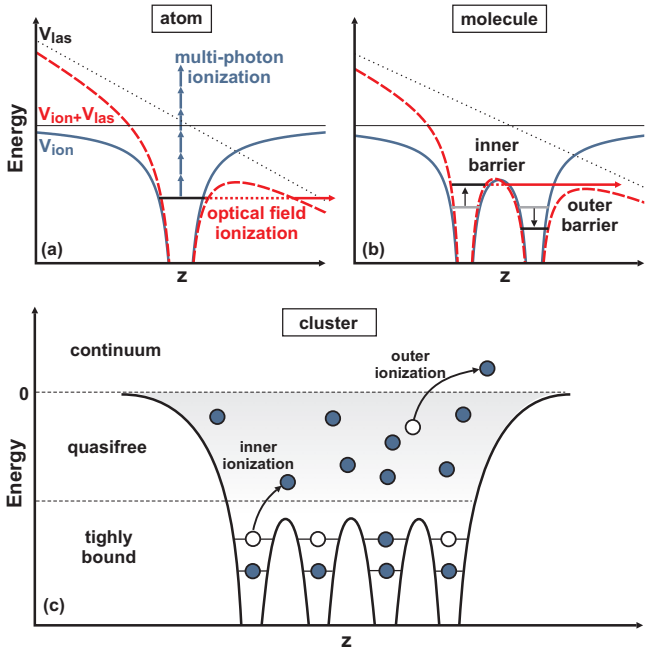


FIG. 4. (Color) Schematic view of ionization mechanisms in atoms, molecules, and clusters. (a) and (b) Potentials of the unperturbed ions $V_{ion}$, the laser $V_{las}$, and their effective sum. In (a) the pathways for MPI and OFI of a bound electron are indicated, while (b) depicts the CREI mechanism. The vertical arrows in (b) indicate the Stark shift. (c) Inner and outer ionization of a cluster based on an effective potential.

A useful measure for the significance of MPI over OFI is the Keldysh adiabaticity parameter (Keldysh, 1965)

$$\gamma = \sqrt{\frac{E_{IP}}{2U_p}}, \tag{5}$$

which compares the IP with the peak kinetic energy of a freely quivering electron ($2U_p$). Single-photon or multiphoton ionization dominates for $\gamma \gg 1$, where the quiver energy is small compared to the IP. For $\gamma \lesssim 1$, the binding energy can be overcome within a single laser cycle and OFI is promoted. An equivalent expression for the Keldysh parameter is $\gamma = \omega_{las}\tau_{tunnel}$, which gives a ratio of the tunneling time $\tau_{tunnel} = \sqrt{2E_{IP}m_e/e^2\mathcal{E}_0^2}$ and the optical period. Optical field ionization dominates if the tunneling time is comparable to or smaller than the optical period; MPI is the leading process otherwise.

Within the tunneling regime ($\gamma \lesssim 1$), the ionization probability in one optical cycle approaches unity if the potential barrier can be fully suppressed. For an atomic system, this so-called barrier suppression ionization (BSI) roughly sets in at the threshold intensity

$$I_{BSI} = \frac{\pi^2 c\epsilon_0^3}{2e^6}\frac{E_{IP}^4}{q^2} \approx 4\times 10^9 \frac{(E_{IP}[\mathrm{eV}])^4}{q^2}[\mathrm{W/cm^2}], \tag{6}$$

which reasonably predicts ion appearance intensities in atomic gases (Augst *et al.*, 1989). Note that Eq. (6) was used to determine the critical intensities in Table I.

The above considerations apply to isolated atoms where the laser parameters govern the dynamics. For extended systems, i.e., from the molecular level on, structural details become increasingly important. Ionization barriers are influenced by the fields from neighboring ions, which, for example, give rise to charge-resonance-enhanced ionization (CREI) well known from strong-field ionization of diatomic molecules (Seideman *et al.*, 1995; Zuo and Bandrauk, 1995). Within this process, an appropriate internuclear separation results in a simultaneous lowering or suppression of inner and outer potential barriers with respect to the Stark-shifted electronic states [see Fig. 4(b)], giving rise to an enhanced ionization rate. For larger or smaller separations either the inner or outer barriers increase and the ionization probability is reduced. As a truly cooperative effect, CREI has been considered also for very small clusters (Véniard *et al.*, 2001; Siedschlag and Rost, 2002) (see Sec. VI.B.1).

Very convenient for describing charging dynamics in larger systems is the concept of inner and outer ionizations (Last and Jortner, 1999). As indicated in Fig. 4(c), electrons in the cluster may be classified into tightly bound, quasifree, and continuum electrons. Within this picture, *inner ionization* describes the excitation of tightly bound electrons to the conduction band; i.e., electrons are removed from their host ion but reside within the cluster. Correspondingly, the final excitation into the continuum and the subsequent escape from the system are termed *outer ionization*, which contributes to the net ionization of the system. At moderate laser intensities, systems with initially delocalized electrons, such as metallic particles, may undergo outer ionization only. In any case the energy span between the thresholds for inner and outer ionizations grows with cluster charge [cf. Fig. 4(c)], underlining the growing importance of quasifree electrons for the interaction dynamics. Besides purely laser-induced MPI and OFI, ionization can be driven by cluster polarization (field amplification) or cluster space-charge fields subsequent to strong ionization. In addition, quasifree electrons can drive electron impact ionization (EII) as may be described by semiempirical cross sections (Lotz, 1967). The onset and self-amplification of such additional processes are frequently termed *ionization ignition* (Rose-Petruck *et al.*, 1997).

The presence of a *nanoplasma*, i.e., of quasifree electrons and (multi)charged atomic ions in the cluster, has substantial impact on the energy capture from a laser pulse. If collective effects are negligible, electrons can acquire energy from the laser field via inverse bremsstrahlung (IBS), i.e., by absorbing radiation energy during scattering in the Coulomb field of the ions. IBS relies on the conversion of laser-driven electron motion into thermal energy because of directional momentum redistribution within elastic collisions and is a basic volume-heating effect in underdense plasmas (Krainov, 2000). Considering a fixed collisional dephasing time $\tau_{\mathrm{coll}}$ (inverse collision frequency), the IBS heating rate per electron in terms of the ponderomotive potential reads

$$\left\langle \frac{dE}{dt} \right\rangle_{\mathrm{IBS}} = 2U_p \frac{\tau_{\mathrm{coll}}\omega_{\mathrm{las}}^2}{\tau_{\mathrm{coll}}^2\omega_{\mathrm{las}}^2 + 1}. \tag{7}$$

Whereas the heating rate becomes independent of $\omega_{\mathrm{las}}$ in the low-frequency case (dc limit), a $U_{\mathrm{p}}/\tau_{\mathrm{coll}}$ dependence is found for $\tau_{\mathrm{coll}}\omega_{\mathrm{las}} \gg 1$. It should be noted that the collisional relaxation time, which is a function of electron temperature (cf. Sec. II.A) and becomes frequency dependent ($\tau_{\mathrm{coll}} \propto \omega_{\mathrm{las}}^{2/3}$) for short-wavelength laser excitation, is in general difficult to obtain. For laser-irradiated clusters, pure IBS heating dominates the energy capture of quasifree electrons only at laser frequencies far above the Mie plasmon frequency. If the laser frequency becomes comparable to or smaller than $\omega_{\mathrm{Mie}}$, the collective response of quasifree electrons in the cluster has to be taken into account. Surface charges from the laser-driven collective electron displacement induce polarization fields, which strongly modify the effective field in the cluster in amplitude and phase. For a spherical plasma and sufficiently small displacements the corresponding restoring force is linear; i.e., the absorption rate per electron for collective IBS heating is described by a Lorentz profile,

$$\left\langle \frac{dE}{dt} \right\rangle_{\mathrm{Res}} = 2U_p \frac{\tau_{\mathrm{coll}}\omega_{\mathrm{las}}^4}{\tau_{\mathrm{coll}}^2(\omega_{\mathrm{Mie}}^2 - \omega_{\mathrm{las}}^2)^2 + \omega_{\mathrm{las}}^2}. \tag{8}$$

This expression is equivalent to the heating rate assumed in Ditmire's nanoplasma model (cf. Sec. III.C). Whereas the absorption rates in Eqs. (7) and (8) meet in the high-frequency limit, IBS heating is strongly suppressed for $\omega_{\mathrm{las}} \ll \omega_{\mathrm{Mie}}$ due to efficient screening of the external field by the collective electron displacement. Most importantly, excitation with $\omega_{\mathrm{las}} \approx \omega_{\mathrm{Mie}}$ leads to plasmon-enhanced energy absorption in Eq. (8) [cf. the cross sections in Fig. 1(b)]. Resonant collective driving of cluster electrons can produce strong field amplification that supports cluster ionization and direct acceleration of electron (Reinhard and Suraud, 1998; Fennel, Döppner, *et al.*, 2007).

It should be noted that in the above discussion the absorption rates have been assumed to scale linearly with intensity ($\propto U_p$) [cf. Eqs. (7) and (8)]. This requires that the dephasing time and the plasmon frequency are constants. In strong fields, however, the large quiver amplitudes actively modify the nanoplasma properties. Hence, both the dephasing time and the plasmon frequency become functions of intensity which introduces additional nonlinear terms.

Another important aspect for the cluster response to strong optical laser fields is the time dependence of the plasmon energy. The plasmon energy scales as $\omega_{\mathrm{Mie}} \propto \sqrt{\rho_{\mathrm{bg}}(t)}$, where $\rho_{\mathrm{bg}}$ is the ion-background charge density. In early stages of the interaction $\rho_{\mathrm{bg}}$ is usually too high for being in resonance with the driving IR field; i.e., the system is *overcritical*. This is the case in metal- and, already after moderate inner ionization, in rare-gas clusters and leads to strongly suppressed IBS heating as explained above. Less efficient surface heating effects such as vacuum heating or Brunel heating (Brunel, 1987;

Taguchi *et al.*, 2004) remain active in this overcritical state. Therefore electrons that are pulled away from the surface by the laser field are accelerated outside and contribute their acquired energy upon recollision with the cluster. In any case, as a result of moderate charging and heating, Coulomb forces due to ionization and thermal electron pressure eventually induce an expansion of the cluster. Corresponding time scales are typically between a few tens of fs to some ps (see Sec. II.A for an estimate of the radius doubling time for pure Coulomb explosion). With cluster expansion the frequency of the collective mode decreases and transiently matches the laser frequency at a certain time, producing a short-lived but strong absorption enhancement [cf. Eq. (8)]. This idea is a central element of the hydrodynamic approach proposed by Ditmire *et al.* (1996) (see Sec. III.C), however, characterizing the resonance condition in terms of a critical electron density. The latter is justified only for nearly charge neutral systems, such as very large clusters. Since, according to the harmonic potential theorem (Dobson, 1994), the ionic background creates the restoring force for quasifree electrons, the background charge density is the more general parameter also applicable to charged systems. Nonetheless, for sufficiently long pulses the transient resonance induces efficient heating of quasifree electrons and, as a consequence, strongly supports outer ionization and cluster Coulomb explosion. At high laser intensity, this delayed resonant coupling is important irrespective of the cluster material and leaves clear signatures in the absorption as well as in emission spectra (see Sec. VI.B.1).

### D. Classification of coupling regimes

While the relative importance of the above mechanisms depends on the specific scenario, regimes can be identified where particular processes prevail. However, such classification cannot be achieved based on a single parameter such as laser intensity. While very low intensities lead to linear and very high ones to nonlinear behavior, other laser characteristics or cluster properties determine the nature of the response for intermediate cases. We discuss a rough sorting of regimes used throughout this paper.

The *linear regime* is the domain of weak laser fields associated with single-photon processes and large values of $\gamma$ [cf. Eq. (5)]. The mechanisms are sensitive predominantly to the laser frequency. The prevailing examples are optical response spectra. As this is a key tool, there is a large body of reviews and books [see, e.g., Brack (1993), de Heer (1993), Haberland (1994), and Kreibig and Vollmer (1995)]. Early cluster experiments often used ns pulses for studies on structure or low-energy dynamics (Haberland, 1994; Näher *et al.*, 1997). Another typical process is single-photon ionization which can be analyzed by photoelectron spectroscopy [see Fig. 1(a) and Sec. V.A].

The *multiphoton regime* is associated with moderate laser intensities where processes induced by the absorption of multiple photons begin to show up ($I \sim 10^8$–$10^{13}$ W/cm$^2$ depending on material and frequency). Each laser parameter, i.e., frequency, field strength, and pulse profile, becomes equally important. Typical examples are second harmonic generation (Götz *et al.*, 1995; Klein-Wiele *et al.*, 1999) and multiphoton ionization. Of particular interest are cases where a multiple of the photon energy can excite an intermediate state of the system. Then, besides direct MPI, a sequential ionization from the (long-living) intermediate state becomes possible (Pohl *et al.*, 2001). Another example is above-threshold ionization. Processes emerging in the multiphoton regime are discussed in Sec. V.B.

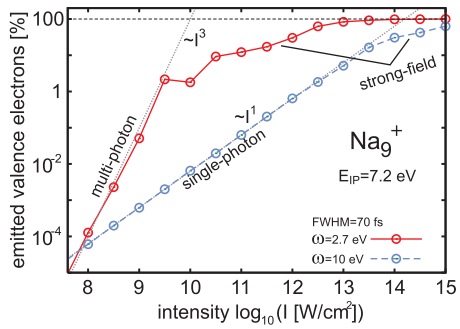


FIG. 5. (Color) Ionization of $Na_9^+$ as a function of laser intensity for excitation by 70 fs cos$^2$-shaped laser pulses for two frequencies (as indicated). As the ionization potential is 7.2 eV, three photons of $\hbar\omega_{las}=2.7$ eV are required to lift an electron into the continuum (multiphoton ionization) while one photon suffices for $\hbar\omega_{las}=10$ eV (linear behavior). At high intensity both cases become nonperturbative, indicating strong-field conditions. Note that $\hbar\omega_{las}=2.7$ eV is close to the Mie plasmon of $Na_9^+$, which leads to the early onset of the strong-field response in this case. Calculations are done in TDLDA.

At sufficiently high intensity, laser irradiation produces large ionization and strong heating ($I \sim 10^{12}$–$10^{19}$ W/cm$^2$). The excitation of many electrons and distinct feedback effects on the response indicate the so-called *strong-field domain* where the dynamics cannot be treated perturbatively. Typically, the excitation leads to cluster Coulomb explosion accompanied by emission of energetic particles, i.e., electrons and ions, as well as photons. The emitted ions usually carry higher charges than in the case of irradiation of single atoms which underlines the impact of cooperative processes. Moreover, the reactions proceed somehow similar for different cluster materials (from metals to rare gases) since electrons from atomic shells are activated and the transient nanoplasma determines the dynamics. Such highly nonlinear processes are discussed in Sec. VI.

A possible marker for the actual regime is the total ionization yield as a function of laser intensity. Lowest-order perturbation theory predicts that the yield scales with $\propto I^\nu$, where $\nu$ is the number of photons required to overcome the ionization potential. Figure 5 gives an example for $Na_9^+$ excited with 70 fs laser pulses and shows the intensity-dependent electron yield for two different laser frequencies. The slope at low intensities agrees

TABLE II. Hierarchy of approaches for the description of electrons and ions in a cluster. Acronyms are defined in the text. The range of applications is listed in the column "Regime" where structure is abbreviated as S, excitation spectra (optical response) as E, and dynamics as D. The label D* indicates the capability to describe electron emission and E* stands for excitation energy.

| Approach | Scheme | System | $N$ | $E^*/N$ (eV) | Regime | Examples |
|---|---|---|---|---|---|---|
| | | Approximations for the electron system | | | | |
| *Ab initio* | Full TDSE | He | 2 | | S D | Parker *et al.*, 2003 |
| | QMC | $C_N$ | $\lesssim 60, \infty$ | 0 | S (D) | Ceperley and Alder, 1980 |
| | | Pure $e^-$ | | | | Parker *et al.*, 1996; Needs *et al.*, 2002 |
| | CI | Any | | | S E | Krause *et al.*, 2005; Schlegel *et al.*, 2007 |
| | MCTDH, MCTDHF | Any | | | S E | Caillat *et al.*, 2005; Nest *et al.*, 2005 |
| Quantum DFT | Basis expansion, all electrons | Any | $\lesssim 50$ | 0 | S E | Guan *et al.*, 1995; Matveev *et al.*, 1999 |
| | Basis expansion, pseudopotentials | Any | $\lesssim 200$ | $\lesssim 0.1$ | S E D | Saalmann and Schmidt, 1996; Matveev *et al.*, 1999 |
| | Coordinate space grid, pseudopotentials | Any | $\lesssim 200$ | $\lesssim 1$ | S E D* | Yabana and Bertsch, 1996; Calvayrac *et al.*, 2000 |
| Semiclassical DFT | Vlasov | Clusters | $\lesssim 5000$ | $>0.1$ | S D* | Feret *et al.*, 1996; Fennel *et al.*, 2004 |
| | VUU | | | | S D* | Domps *et al.*, 1998a; Köhn *et al.*, 2008 |
| | Thomas-Fermi | Any | $\lesssim 10^6$ | $>0.1$ | S D | Blaise *et al.*, 1997; Domps *et al.*, 1998b |
| Classical | MD | Any | $\lesssim 10^6$ | $>0.1$ | D | Rose-Petruck *et al.*, 1997; Ditmire, 1998 |
| | Rate equations | Any | $>10^4$ | $>1$ | D | Ditmire *et al.*, 1996; Milchberg *et al.*, 2001 |
| | | Approximations for the ionic system | | | | |
| Quantum | Full TDSE | $H_2^+$ | 1+2 | Any | D | Saugout *et al.*, 2007 |
| Nonadiabatic | MD | Any | $\lesssim 10^6$ | Any | S E D | Calvayrac *et al.*, 2000 |
| BO | MD, QM | Any | $\lesssim 10^6$ | $E^*_{\rm ion} < E^*_{\rm el}$ | D | Bréchignac *et al.*, 1994 |

with the $I^\nu$ law, yielding $\nu=3$ (multiphoton) for the lower frequency and $\nu=1$ (single photon) for the higher frequency. However, the curves turn over at higher intensities where sorting in orders of photons becomes obsolete (breakdown of perturbation theory). One approaches the strong-field domain. Note that the two laser frequencies perform in a very different way. With $\hbar\omega_{\rm las}=10$ eV excitation, the yield follows the linear behavior and becomes nonperturbative at rather large intensities. With the lower frequency the ionization is a three-photon process and the transition to the nonlinear regime evolves at a much lower intensity. Two effects contribute in the latter case: the near-resonance excitation of the Mie plasmon (Reinhard and Suraud, 1998) and the stronger impact of optical field effects at lower Keldysh parameters.

## III. THEORETICAL TOOLS FOR CLUSTER DYNAMICS

### A. Approaches in general

Clusters are complex systems and their theoretical description requires approximations to the full quantum-mechanical many-body problem—the more so for truly dynamical situations. As approximations are always a compromise between feasibility and demands, there exists a rich spectrum of methods. Table II provides an overview of commonly applied methods; in the upper part for electrons and in the lower part for the ions. Keywords, numbers, and citations are guidelines and by no means exhaustive. They should be understood as examples and estimates of orders of magnitude. For *ab initio* methods some entries for typical sizes and excitation energies $E^*$ are left open as they have, in principle, a large range of validity but are in practice limited by quickly growing numerical expense.

The class of *ab initio* theories covers a large range of treatments depending on the size of the underlying basis space, in particular for the configuration interaction (CI) and the multiconfigurational time-dependent Hartree (MCTDH) or multiconfigurational time-dependent Hartree-Fock (MCTDHF) approaches. The most general methods, i.e., the exact solution of the time-dependent Schrödinger equation (TDSE) and the quantum Monte Carlo (QMC) method, are still restricted to

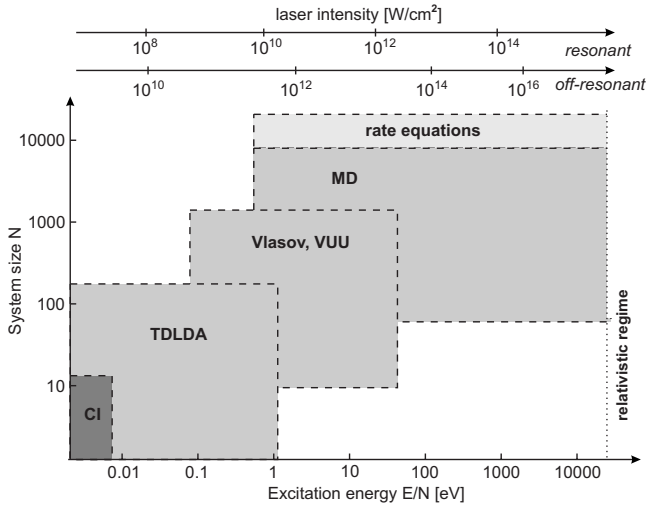


FIG. 6. Schematic view of applicability regimes for different approaches in a landscape of system size vs excitation energy. The excitation energy can be loosely related to typical laser intensities in the optical range, as indicated by the intensity scales on top for resonant or nonresonant condition.

very few electrons and presently not applicable to clusters. The vast majority of theoretical investigations of cluster dynamics with quantum aspects rely on density-functional theory (DFT) based methods, with quantum mechanical (QM) or semiclassical propagation, where the latter means Vlasov or Vlasov-Uehling-Uhlenbeck (VUU) schemes. These will be reviewed in Secs. III.B.1–III.B.3. Violent processes exceed the capability of DFT methods and are treated in a purely classical manner either with molecular dynamics (MD) or, more simple, with rate equations. We sketch both methods in Secs. III.B.4 and III.C.

The large ionic mass usually permits their classical propagation by MD. This may be performed simultaneously with the (nonadiabatic) electron cloud or in the Born-Oppenheimer (BO) approximation if the electrons follow adiabatically the ion field. Light elements (particularly H and He) often call for a quantum-mechanical treatment for the ions. A full quantum treatment, including all electrons and ions, is extremely demanding and has not yet been applied to clusters. However, a QM treatment of He atoms has been widely used for He clusters (Serra *et al.*, 1991; Weisgerber and Reinhard, 1992) and for He material in contact with metal clusters (Ancilotto and Togio, 1995; Nakatsukasa *et al.*, 2002).

Figure 6 complements Table II in sketching the regimes of applicability of theoretical models in the plane of excitation and particle number. As the decision for a method depends on several other aspects (e.g., demand on precision, material, and time span of simulation), the boundaries of the regimes are to be understood as very soft with large zones of overlap between the models. Note also the two intensity scales on top in Fig. 6, which indicate that limitations are also sensitive to the nature of the system response, i.e., resonant or nonresonant. The distinction has to be kept in mind when discussing specific systems.

The limitations for CI (and other *ab initio* methods) are purely a matter of practicability. The time-dependent local density approximation (TDLDA) is limited in system size for practical reasons and in excitation energy for physical ones because of the missing dynamical correlations from electron-electron collisions. The upper limits of VUU are also of purely practical nature, while the lower limits are principle ones, e.g., the negligence of shell effects, tunneling, and interference. The same holds for MD and rate equations. The upper limits in energy and/or laser intensity are given by the onset of the relativistic regime, where retardation effects within the coupling begin to severely influence the dynamics. For the particle size, a general upper limit results from the application of the dipole approximation, which typically breaks down beyond some 10 000 atoms. In larger systems the field propagation effects (attenuation, diffraction, and reflection) need to be taken into account.

### B. Effective microscopic theories

Since a fully *ab initio* treatment of cluster dynamics is hardly feasible, simplifications are necessary by eliminating the details of many-body correlations. This naturally leads to a description in terms of single-particle states which is well manageable and still maintains crucial quantum features. The eliminated degrees of freedom are moved to an effective interaction to be used in the reduced description. This leads into the realm of DFT (Dreizler and Gross, 1990). Time-dependent density-functional theory (TDDFT), i.e., its dynamical extension (Runge and Gross, 1984; Gross *et al.*, 1996), is widely employed in cluster dynamics (Reinhard and Suraud, 2003) and still under development [see, e.g., Marques *et al.* (2006)]. This section provides an overview over the typical approaches used for cluster dynamics these days. We begin with the discussion of the energy functionals, proceed with quantum and semiclassical DFT methods, and conclude with the most simplified treatment, i.e., molecular dynamics.

#### 1. The energy functional

Since DFT relies on a variational formulation, it aims at well-controlled approximations. The starting point is an expression for the total energy of electrons and ions from which all static and dynamic equations can be derived. Approximations are made only at one place, namely, within this energy functional, and everything else follows consistently. Typical energy functionals used in cluster physics (and many other fields) are summarized in Table III.

Key to success (or failure) is the choice of a reliable functional for exchange and correlations. There are several well-tested functionals within LDA [see, e.g., Perdew and Wang (1992)]. These are the workhorses in cluster dynamics. Higher demands, in describing molecular bonding of covalent materials require more elaborate functionals including gradients of the density, as in the generalized gradient approximation (Perdew *et al.*,

TABLE III. Composition of the basic energy functional for electrons, ions, and their coupling $E=E^{\mathrm{ion}}+E^{\mathrm{coup}}+E^{\mathrm{el}}$. The ions are described as classical particles with coordinates $\mathbf{R}_I$ and momenta $\mathbf{P}_I$, $I=1,\ldots,N_{\mathrm{ion}}$, and correspond to the nuclear centers and the deeper lying inert core electrons. The coupling to electrons is mediated by pseudopotentials $V_I^{\mathrm{PsP}}$ which are designed to also incorporate the impact of core electrons on active electrons. $V_I^{\mathrm{PsP}}$ counterweight the Coulomb singularity of point charges (see Coulomb coupling term) and install effectively a soft inner charge distribution for the ion. We show here a local pseudopotential which applies throughout all approaches. Nonlocal versions are often used in connection with QM electron wave functions. Electrons can be treated at various levels of approximation. The QM stage employs single-electron wave functions $\varphi_\alpha$, where $\alpha=1,\ldots,N_{\mathrm{el}}$. The semiclassical Vlasov description replaces an orbital based treatment by a phase-space function $f(\mathbf{r},\mathbf{p})$. In both cases, the Coulomb exchange term and correlations are approximated by effective functionals, usually in local density approximation (LDA) and optionally augmented by a self-interaction correction (SIC). The fully classical level treats electrons as point particles with specifically tuned effective interaction potentials, e.g., by assuming a charge distribution $g(r)$ having a finite width and optionally by adding an additional short range interaction term $V_{\mathrm{sr}}$ to effectively account for Pauli blocking effects. The total electronic density $\rho(\mathbf{r})$ is computed differently when going from the QM over Vlasov to the MD approaches. Note that the current $\mathbf{j}(\mathbf{r})$ is defined analogously to the density.

| Type | Central variables | | Kinetic ($E_{\mathrm{kin}}$) | | Coulomb ($E_{\mathrm{Coul}}$) | | Effective ($E_{\mathrm{eff}}$) | | External ($E_{\mathrm{ext}}$) |
|---|---|---|---|---|---|---|---|---|---|
| Ions | $\{\mathbf{R}_I,\mathbf{P}_I\}$ | $E^{\mathrm{ion}}=$ | $\sum_I \frac{\mathbf{P}_I^2}{2M_I}$ | + | $\frac{e^2}{8\pi\epsilon_0}\sum_{I,J}^{I\neq J}\frac{q_I q_J}{\lvert\mathbf{R}_I-\mathbf{R}_J\rvert}$ | | | + | $E_{\mathrm{ext}}^{\mathrm{ion}}(\mathbf{R}_I,\mathbf{P}_I)$ |
| Coupling | | $E^{\mathrm{coupl}}=$ | | | | | $\sum_I \int d^3\mathbf{r}\rho(\mathbf{r})V_I^{\mathrm{PsP}}(\lvert\mathbf{r}-\mathbf{R}_I\rvert)$ | | |
| | | | Quantum mechanical | | | | | | |
| Electrons | $\{\varphi_\alpha(\mathbf{r})\}$ | $E^{\mathrm{el}}=$ | $\sum_\alpha \langle\varphi_\alpha\lvert\frac{\hat{p}^2}{2m}\rvert\varphi_\alpha\rangle$ | + | $\frac{e^2}{8\pi\epsilon_0}\int d^3\mathbf{r}d^3\mathbf{r}'\frac{\rho(\mathbf{r})\rho(\mathbf{r}')}{\lvert\mathbf{r}-\mathbf{r}'\rvert}$ | + | $E_{\mathrm{xc}}(\rho)-E_{\mathrm{xc}}^{(\mathrm{SIC})}(\rho_\alpha)$ | + | $E_{\mathrm{ext}}^{\mathrm{el}}(\rho,\mathbf{j})$ |
| | | | $\rho(\mathbf{r})=\sum_\alpha\lvert\varphi_\alpha(\mathbf{r})\rvert^2$ | | | | | | |
| | $\Downarrow$ | | Vlasov approximation for electrons | | | | | | |
| | $f(\mathbf{r},\mathbf{p})$ | $E^{\mathrm{el}}=$ | $\int d^3\mathbf{r}d^3\mathbf{p}\frac{p^2}{2m}f(\mathbf{r},\mathbf{p})$ | + | $\frac{e^2}{8\pi\epsilon_0}\int d^3\mathbf{r}d^3\mathbf{r}'\frac{\rho(\mathbf{r})\rho(\mathbf{r}')}{\lvert\mathbf{r}-\mathbf{r}'\rvert}$ | + | $E_{\mathrm{xc}}(\rho)$ | + | $E_{\mathrm{ext}}^{\mathrm{el}}(\rho,\mathbf{j})$ |
| | | | $\rho(\mathbf{r})=\int d^3\mathbf{p}f(\mathbf{r},\mathbf{p})$ | | | | | | |
| | $\Downarrow$ | | Molecular dynamics for electrons | | | | | | |
| | $\{\mathbf{r}_\alpha,\mathbf{p}_\alpha\}$ | $E^{\mathrm{el}}=$ | $\sum_\alpha \frac{p_\alpha^2}{2m}$ | + | $\frac{e^2}{8\pi\epsilon_0}\int d^3\mathbf{r}d^3\mathbf{r}'\frac{\rho(\mathbf{r})\rho(\mathbf{r}')}{\lvert\mathbf{r}-\mathbf{r}'\rvert}$ | + | $\sum_{\alpha\beta}^{\alpha\neq\beta}V_{\mathrm{sr}}(\mathbf{r}_\alpha,\mathbf{p}_\alpha,\mathbf{r}_\beta,\mathbf{p}_\beta)$ | + | $E_{\mathrm{ext}}^{\mathrm{el}}(\mathbf{r}_\alpha,\mathbf{p}_\alpha)$ |
| | | | $\rho(\mathbf{r})=\sum_\alpha g(\lvert\mathbf{r}-\mathbf{r}_\alpha\rvert)$ | | | | | | |

1996). And even these turn out to be insufficient in some dynamical situations. The spurious self-interaction spoils ionization potentials and related observables. This can be cured to some extent by a self-interaction correction (sic) or an appropriate approximation to it [for a discussion in the cluster context see Legrand *et al.* (2002)].

Recent developments in TDDFT employ the full exchange term and try to simplify that by optimized effective (local) potentials (Della-Sala and Görling, 2003; Kümmel and Kronik, 2008). This is still in an exploratory stage and schemes applicable in large-scale dynamical calculations have yet to be developed.

Another source of *effectiveness* is the use of pseudopotentials for ions containing inert core electrons (Szasz, 1985)—a well-settled topic for static problems. Dynamical applications require one to consider the polarizability of core electrons, e.g., in noble metals (Serra and Rubio, 1997). This can be done by augmenting the pseudopotentials with polarization potentials as done in mixed quantum-mechanical molecular dynamic approaches (Gresh *et al.*, 1999) [for a cluster example see Fehrer *et al.* (2005)].

Table III includes the step down to a fully classical treatment (MD for electrons). This level develops its effective interactions on an independent route, i.e., by explicit adjustment of the effective interactions to basic atomic, molecular, or bulk properties (see Sec. III.B.4).

#### 2. Time-dependent density-functional theory

The time-dependent Kohn-Sham (KS) equations coupled with ionic MD are derived by variation of the given energy (see Table III) with respect to the single-electron wave functions $\varphi_\alpha^\dagger$ and to the ionic variables [for details see, e.g., Reinhard and Suraud (2003)]. They read

$$i\hbar\partial_t\varphi_\alpha = \hat{h}_{\rm KS}\varphi_\alpha, \quad \hat{h}_{\rm KS} = \frac{\delta E}{\delta\varphi_\alpha^\dagger}\frac{1}{\varphi_\alpha}, \tag{9a}$$

$$\partial_t \mathbf{R}_I = \nabla_{\mathbf{P}_I} E, \quad \partial_t \mathbf{P}_I = -\nabla_{\mathbf{R}_I} E. \tag{9b}$$

Since by far most applications employ the LDA, the electronic part is called TDLDA. The electronic part is coupled to MD for the ions, yielding together TDLDA-MD. This treatment where electronic and ionic dynamics are propagated simultaneously is compulsory for strong electronic excitations.

There are many situations where rather slow ionic motion dominates and the electron cloud acquires only little excitation energy. Then, one can switch to the adiabatic Born-Oppenheimer (BO) picture,

$$\varepsilon_\alpha\varphi_\alpha^{(\mathbf{R}_I)} = \hat{h}_{\rm KS}\varphi_\alpha^{(\mathbf{R}_I)} \Rightarrow E_{\rm BO}(\varphi_\alpha^{(\mathbf{R}_I)}, \mathbf{R}_I, \mathbf{P}_I), \tag{10a}$$

$$\partial_t \mathbf{R}_I = \nabla_{\mathbf{P}_I} E_{\rm BO}, \quad \partial_t \mathbf{P}_I = -\nabla_{\mathbf{R}_I} E_{\rm BO}. \tag{10b}$$

It is assumed that the electronic wave functions are always relaxed into the (electronic) ground state for a given ionic configuration and its energy expectation value produces a Born-Oppenheimer energy $E_{\rm BO}$ which depends effectively only on ionic variables [see Eq. (10a)]. The ionic energy $E_{\rm BO}$ is then used in a standard ionic MD [see Eq. (10b)]. The method allows one to use larger time steps because only the slow ionic motion has to be treated explicitly. On the other hand, full electronic relaxation takes many static steps and it thus depends on the particular application whether BO-MD is advantageous or not.

The stationary limit of TDLDA (electronic part) is obvious; it is given by Eq. (10a). The situation is more involved for the ions. A stationary point is defined by $\partial_t \mathbf{P}_I = 0$ and may be reached by following the steepest gradient of the potential field. However, the ionic energy landscape is swamped by competing local minima. A straightforward gradient path will end up in some minimum but not easily in the lowest one, i.e., the ground state. One needs to employ stochastic methods, such as simulated annealing and Monte Carlo sampling, to explore the high-dimensional landscape of the ionic energy surface [for details see Press *et al.* (1992)].

The most time consuming part in TDLDA-MD, i.e., Eqs. (9), is electron propagation. There are basically two different approaches: basis expansion or coordinate-space grid representation (see Table II, and references therein). Basis expansions are more efficient in handling different length scales as typical for covalent systems. Coordinate-space grids, on the other hand, are more adapted for the treatment of highly excited systems where electron emission plays a crucial role. In the latter, absorbing boundary conditions can easily be implemented to avoid unphysical backscattering for the analysis of photoelectron spectra and angular distributions [see, e.g., Calvayrac *et al.* (2000) and Pohl *et al.* (2004b)]. An efficient means to find the electronic ground state is the accelerated gradient iteration (Blum *et al.*, 1992). Time stepping is usually based on a Taylor expansion of the time evolution operator. An efficient alternative is the time-splitting method which proceeds by interlaced kinetic and potential evolution (Feit *et al.*, 1982; Calvayrac *et al.*, 2000). The ionic MD usually employs the velocity-Verlet algorithm [see, e.g., Press *et al.* (1992)]. Ground-state configurations are best searched for by stochastic methods as mentioned.

#### 3. Semiclassical approaches

As the particle number and excitation energy grow, an orbital-based treatment of the electronic degrees of freedom becomes practically unfeasible and further approximations have to be made. Less demanding are semiclassical time-dependent density-functional methods, which describe the evolution of the one-body electron phase-space distribution or the electron density and average local currents. The price for such simplification is the loss of the quantized electronic level structure, interference effects, and single electron-hole excitations. However, as these contributions become less important for larger systems with sufficiently narrow energy levels and high excitations, semiclassical methods provide a powerful tool to explore strongly nonlinear laser-cluster dynamics.

A semiclassical equation of motion for the one-particle electron phase-space density $f(\mathbf{r},\mathbf{p})$ as an approximation to quantal mean-field dynamics can be found from the well-known $\hbar \to 0$ expansion [see, e.g., Bertsch and Das Gupta (1988), Domps *et al.* (1997),

Plagne *et al.* (2000), Fennel *et al.* (2004), and Fennel and Köhn (2008)]. This to lowest order yields the Vlasov equation

$$\frac{\partial}{\partial t}f + \frac{\mathbf{p}}{m}\cdot\nabla_{\mathbf{r}}f - \nabla_{\mathbf{p}}f\cdot\nabla_{\mathbf{r}}V_{\mathrm{mf}}(\mathbf{r},t) = 0, \tag{11}$$

which is widely used in plasma physics. The effective electron mean-field interaction potential $V_{\mathrm{mf}}(\mathbf{r},t)$ in Eq. (11) follows from the variation of the potential energy of the electrons $E_{\mathrm{pot}}^{\mathrm{el}} = E_{\mathrm{Coul}}^{\mathrm{el}} + E_{\mathrm{xc}}^{\mathrm{el}} + E^{\mathrm{coupl}} + E_{\mathrm{ext}}^{\mathrm{el}}$ (cf. Table III) with respect to the local electron density $\rho(\mathbf{r},t)$, i.e., by $V_{\mathrm{mf}} = \delta E_{\mathrm{pot}}^{\mathrm{el}}/\delta\rho$. Ionic motion may be described in the same way as for TDLDA-MD [see Eqs. (9)]. Quantum effects, such as exchange and correlation in LDA, are now solely contained in the effective potential and the initial conditions for the distribution function. The latter can be determined from the self-consistent Thomas-Fermi ground state (Thomas, 1927; Fermi, 1928) according to $f^0(\mathbf{r},\mathbf{p}) = 2/(2\pi\hbar)^3\Theta(p_F(\mathbf{r}) - p)$, where $\Theta$ is the Heaviside function, $p_F(\mathbf{r}) = \sqrt{2m[\mu - V_{\mathrm{mf}}(\mathbf{r})]}$ is the local Fermi momentum, and $\mu$ is the chemical potential. The Thomas-Fermi-Vlasov dynamics resulting from the propagation of the initial distribution $f^0(\mathbf{r},\mathbf{p})$ according to Eq. (11) constitutes the semiclassical counterpart of TDLDA.

A generic limitation of mean-field approaches, such as TDLDA and Vlasov, is the negligence of electron-electron collisions. This deficiency may become significant for strong departure from the ground state because of considerably weakened Pauli blocking. In the semiclassical formulation, binary collisions can be incorporated with a Markovian collision integral of the Uehling-Uhlenbeck type (Uehling and Uhlenbeck, 1933) [see Bertsch and Das Gupta (1988), Calvayrac *et al.* (2000), and Köhn *et al.* (2008)]. This results in the VUU equation,

$$\frac{\partial}{\partial t}f + \frac{\mathbf{p}}{m}\cdot\nabla_{\mathbf{r}}f - \nabla_{\mathbf{p}}f\cdot\nabla_{\mathbf{r}}V_{\mathrm{mf}}(\mathbf{r},t) = I_{\mathrm{UU}},$$

with

$$I_{\mathrm{UU}}(\mathbf{r},\mathbf{p}) = \int d\Omega d^3\mathbf{p}_1 \frac{|\mathbf{p}-\mathbf{p}_1|}{m}\frac{d\sigma(\theta,|\mathbf{p}-\mathbf{p}_1|)}{d\Omega} \times[f_{\mathbf{p}'}f_{\mathbf{p}_1'}(1-\tilde{f}_{\mathbf{p}})(1-\tilde{f}_{\mathbf{p}_1}) - f_{\mathbf{p}}f_{\mathbf{p}_1}(1-\tilde{f}_{\mathbf{p}'})(1-\tilde{f}_{\mathbf{p}_1'})]. \tag{12}$$

The collision term embodies a local gain-loss balance for elastic electron-electron scattering $(\mathbf{p},\mathbf{p}_1)\leftrightarrow(\mathbf{p}',\mathbf{p}_1')$ determined by the differential cross section $d\sigma(\theta,|\mathbf{p}_{\mathrm{rel}}|)/d\Omega$, the local phase-space densities $f_{\mathbf{p}} = f(\mathbf{r},\mathbf{p})$, and the Pauli blocking factors in given in parentheses as functions of the relative phase-space occupation for paired spins $\tilde{f}_p = (2\pi\hbar)^3 f_p/2$. The velocity-dependent scattering cross section can be calculated for a screened electron-electron potential using standard quantum scattering theory (Domps *et al.*, 2000; Köhn *et al.*, 2008). Since the collision term in the VUU description vanishes in the ground state because of the blocking factors, the Vlasov dynamics is recovered asymptotically in the limit of weak perturbation. Commonly, the Vlasov as well as the VUU equations are solved with the test particle method only for valence electrons, while core electrons are described with ion pseudopotentials [see, e.g., Giglio *et al.* (2002); Fennel *et al.* (2004), and Köhn *et al.* (2008)].

Further simplifications can be deduced from hydrodynamic considerations (Bloch, 1933; Ball *et al.*, 1973), i.e., by assuming local equilibrium and a slowly varying irrotational velocity field. In this case, the electronic dynamics can be solely described by the time-dependent electron density $\rho(\mathbf{r},t)$ and a velocity field $\mathbf{v}(\mathbf{r},t)$. The corresponding equations of motion follow from a variational principle (Domps *et al.*, 1998b), leading to a standard hydrodynamic problem for an inviscid fluid,

$$\frac{\partial}{\partial t}\rho = -\nabla\cdot(\rho\mathbf{v}), \tag{13a}$$

$$\frac{\partial}{\partial t}\mathbf{v} = -\mathbf{v}\nabla\cdot\mathbf{v} - \frac{1}{m}\nabla(V_{\mathrm{kin}}[\rho] + V_{\mathrm{mf}}[\rho]), \tag{13b}$$

where $V_{\mathrm{kin}}$ and $V_{\mathrm{mf}}$ are the potentials of the internal kinetic energy characterizing the local equilibrium and the interaction energy. The continuity equation [Eq. (13a)] and the Euler equation [Eq. (13b)] describe the conservation of mass and momentum explicitly, while the equation of state is implicit in the self-consistent potentials. Analogous to $V_{\mathrm{mf}}$, $V_{\mathrm{kin}}$ results from variation of the now density-dependent internal kinetic energy. Within the time-dependent Thomas-Fermi (TDTF) approach, the internal kinetic energy is described in the Thomas-Fermi approximation by $V_{\mathrm{kin}}^{\mathrm{TF}}(\mathbf{r},t) = (\hbar^2/2m)[3\pi^2\rho(\mathbf{r},t)]^{2/3}$. TDTF represents the simplest semiclassical time-dependent density-functional approach. The reduction to the propagation of four scalar fields (density plus three velocity components) simplifies the numerical treatment, which is particularly appealing for the study of large systems. For application to metal clusters, see, e.g., Domps *et al.* (1998b). However, as deformations of the local Fermi sphere are neglected (local equilibrium), TDTF is not capable of describing thermal excitations or highly nonlinear dynamics.

#### 4. Classical molecular dynamics

A basic limitation of DFT treatments, quantum or semiclassical, lies in the fact that they are of mean-field nature and thus neglect the effect of fluctuations even if thermalization due to electron-electron collisions can be accounted for approximately in the semiclassical case. While mean-field treatments provide a fully acceptable approach for moderately perturbed systems, they cannot account for the large microfield fluctuations arising from strong-field laser excitation. Exploring these fluctuations on a microscopic basis requires the construction of a statistical ensemble of possible trajectories, which exceeds standard mean-field capabilities. However, even if the approximate description of strong-field-induced clus-

ter dynamics with the instantaneous ensemble average provided by mean-field DFT methods may be sufficient, technical difficulties hamper their application to realistic systems in this case. The problem arises if energetic quasifree electrons and strongly bound electrons become involved at the same time, which is the typical situation in cluster ionization dynamics in strong fields where highly charged ions are produced. Hence, different sets of scale in terms of distances and energies need to be resolved numerically, which quickly becomes prohibitive.

Presently, the single practical solutions to microscopically resolve ionization dynamics leading to high atomic charge states are classical MD techniques. Numerous groups have developed corresponding methods over the years where quasifree electrons and ions are described purely in a classical way (Rose-Petruck *et al.*, 1997; Ditmire, 1998; Last and Jortner, 1999, 2000; Ishikawa and Blenski, 2000; Siedschlag and Rost, 2002, 2004; Toma and Muller, 2002; Saalmann and Rost, 2003; Bauer, 2004a; Jurek *et al.*, 2004; Jungreuthmayer *et al.*, 2005; Belkacem *et al.*, 2006a, 2006b; Fennel, Ramunno, and Brabec, 2007).

Once inner ionized, electrons are explicitly followed according to classical equations of motion under the influence of the laser field and their mutual Coulomb interaction. A striking advantage of the classical treatment is the account of the classical microfield and many-particle correlations. Nevertheless, there are some difficulties to be circumvented. First, the Coulomb interaction has to be regularized in order to restore the stability of the classical Coulomb system and to avoid classical electron-ion recombination below the atomic energy levels. This is usually done by smoothing the Coulomb interaction, e.g., by inserting a cutoff (Ditmire *et al.*, 1998) or by attributing an effective width to the particle (Belkacem *et al.*, 2006b; Fennel, Ramunno, and Brabec, 2007). The second problem concerns the computational costs. Standard MD simulations scale with the square of the particle number due to the direct treatment of the two-body interactions. For clusters beyond a few thousands of atoms this may easily become prohibitive and more elaborate algorithms such as hierarchical tree codes or electrostatic particle-in-cell (PIC) methods can be used (Barnes and Hut, 1986; Pfalzner and Gibbon, 1996). Such methods indeed allow the treatment of large clusters on sufficiently long times (Saalmann and Rost, 2003, 2005; Jungreuthmayer *et al.*, 2005; Krishnamurthy *et al.*, 2006; Kundu and Bauer, 2006; Saalmann *et al.*, 2006; Petrov and Davis, 2008). Another option for describing large clusters, even at very high laser intensity including relativistic effects, is the electromagnetic PIC code [see, e.g., Jungreuthmayer *et al.* (2004) and Fukuda *et al.* (2006)].

Inner ionization can be treated in various nonexplicit ways. Since deeply bound electrons are associated with large energies and short time scales (typically in the attosecond domain), they are not propagated explicitly in most cases. An exception can be found in Belkacem *et al.* (2006a, 2006b). In general, however, statistical approaches relying on probabilistic estimates of inner ionization are used. Common strategies for describing atomic field ionization are the consideration of barrier-suppression ionization or the application of tunnel ionization rates (see Sec. II.B). Collisional ionization may be modeled with the semiempirical Lotz cross sections (Lotz, 1967). However, this implies that ionization rates, which may be altered by many-particle effects in the systems, become a crucial ingredient of the dynamics.

### C. Rate equations and the nanoplasma model

The last step in the hierarchy of approaches from the most microscopic to the most macroscopic ones is the rate equation models, which describe the system in terms of a limited set of averaged global variables. Their time evolution is obtained from a few equations accounting for the major couplings, i.e., the interactions with the laser field and the internal electronic and ionic processes. Such a description is based on a continuum picture and thus requires the clusters to be sufficiently large.

The original formulation of a corresponding model for strong-field cluster dynamics was done by Ditmire *et al.* (1996) and is known as the *nanoplasma model*. This name reflects the assumption that rapid inner ionization of clusters exposed to intense laser fields creates a strongly charged but quasihomogeneous plasma. The typical cluster size domain for which such a picture applies is the nanometer range, whence the denomination. The assumption of a homogeneous plasma requires clusters of sizes larger than the Debye length $\lambda_D = \sqrt{\epsilon_0 k_B T/e^2\rho}$ of the system. A typical density of $\rho \sim 10^{23}$ cm$^{-3}$ and temperature of $T \sim 1$ keV lead to $\lambda_D \sim 5$ Å.

The basic dynamical degrees of freedom in the nanoplasma model are $N_j$ the number of ions in charge state $j$, $N_e$ the number of "free" (inner ionized) electrons, $E_{\rm int}$ the internal energy of the electron cloud, and $R$ the radius of the cluster. The global character of these variables implies that ions, electrons, and energy are distributed homogeneously in a sphere of radius $R$. The evolution of ion numbers $N_j$ follows the rate equation

$$\frac{dN_j}{dt} = W_j^{\rm tot} N_{j-1} - W_{j+1}^{\rm tot} N_j, \tag{14}$$

where $W_j^{\rm tot}$ is the ionization rate for ions in charge state $N_j$ accounting for tunneling and impact ionization. While tunnel ionization dominates early stages of the evolution, collisional ionization takes the lead at later times. The electron number $N_e$ evolves according to

$$\frac{dN_e}{dt} = \sum_j j\frac{dN_j}{dt} - \frac{dQ}{dt}, \tag{15}$$

where $Q$ is the total net charge of the cluster whose change is determined by the integrated net flow through the cluster surface. The evolution of the cluster radius

$$\frac{\partial^2 R}{\partial t^2} = \frac{p_C + p_H}{n_i m_i} \frac{5}{R} \tag{16}$$

is determined by the total pressure, which is composed of Coulomb pressure $p_C$ due to net charge and thermal pressure $p_H$ of the hot electron gas (treated as an ideal gas of temperature $T_e$ and internal energy $E_{\rm int} = 3N_e kT_e/2$). Here $n_i$ and $m_i$ denote the number density and the mass of the ions.

The internal energy $E_{\rm int}$ of the electron cloud follows as

$$\frac{dE_{\rm int}}{dt} = P_{\rm abs} - \frac{2E_{\rm int}}{R}\frac{\partial R}{\partial t} - \sum_j E_{\rm IP}^{(j)} \frac{\partial N_j}{\partial t} - P_{\rm loss}, \tag{17a}$$

$$P_{\rm abs} = -\frac{V\epsilon_0}{2} \mathcal{E}_{\rm int}^2 \, {\rm Im}[\epsilon(\omega_{\rm las})], \tag{17b}$$

due to absorption of electromagnetic energy ($P_{\rm abs}$), to cooling through global expansion ($\partial R/\partial t$ term), to ionization processes ($\partial N_j/\partial t$ term), and to energy loss by electron flow through the cluster surface ($P_{\rm loss}$). Here $E_{\rm IP}^{(j)}$ are ionization potentials of ions with charge state $j$. The cycle-averaged heating rate $P_{\rm abs}$ involves the volume $V$ and the internal electric field amplitude in a dielectric sphere $\mathcal{E}_{\rm int} = 3\mathcal{E}_0 f(t)/|2+\epsilon(\omega)|$, where $\mathcal{E}_0 f(t)$ is the vacuum laser field envelope. The dielectric constant $\epsilon(\omega)$ is usually taken from the Drude model $\epsilon(\omega) = 1 - \omega_p^2/\omega(\omega + i\nu)$, with $\omega_p^2 = n_e e^2/m_e\epsilon_0$ the plasma (or volume plasmon) frequency and the collision frequency $\nu$ for electron-ion scattering. With these assumptions, the cycle-averaged heating rate is equivalent to Eq. (8) in Sec. II.C and exhibits a resonance when the electronic density fulfills $n_e = 3n_e^{\rm crit}$, where $n_e^{\rm crit} = m_e\epsilon_0\omega^2/e^2$ is called critical density. This condition reflects the Mie plasmon resonance of a neutral spherical particle (Kreibig and Vollmer, 1995) (see Secs. II.A and II.C).

Equations (14)–(16), (17a), and (17b) constitute the dynamics of the nanoplasma model. In spite of its simplicity, the model contains the basic competing processes in the dynamics of the irradiated cluster in a nanoplasma state. The model is technically simple but requires several empirical ingredients, such as, e.g., the various ionization rates. It also involves strong simplifications such as a thermal electron distribution, a heating rate that scales linearly with intensity and crude treatment of space-charge effects and electron emission. Nevertheless, it was applied to many experimental results with some successes and its original formulation was extended in several respects.

The original model may be questioned at various places, e.g., regarding the assumption of homogeneous distributions of all species in the cluster. This constraint was relaxed by Milchberg *et al.* (2001) by considering a radius-dependent distribution. Further, the damping effect of the cluster surface is neglected. The damping effect can be introduced using a modified collision frequency $\nu = \nu_{\rm ei} + Av/R$, which contains electron-ion collisions through ($\nu_{ei}$) and an additional term for surface-induced Landau damping $Av/R$ ($v$ average electron velocity; $A$ model parameter close to unity). The surface contribution has been shown to play an important role for energy absorption (Megi *et al.*, 2003). Recently detailed cross sections were computed to include high-order ionization transitions involving intermediate excited states for describing x-ray emission from Ar clusters (Micheau *et al.*, 2007). Another important contribution is the lowering of ionization thresholds in the cluster due to plasma screening effects (Gets and Krainov, 2006), which was shown to significantly alter the ion charge distribution as well as the heating dynamics (Hilse *et al.*, 2009).

One should also note that the nanoplasma model, as a statistical continuum picture, may only describe the gross features of the interaction of intense lasers with clusters. In particular, it cannot access experimental results beyond average values. The model may thus fail in describing the profiles or far tails of, e.g., ion charge state or energy distributions. More detailed insight can, for example, be gained from MD simulations. Nonetheless, even in its crudest version the nanoplasma model may serve as an acceptable starting point for insights into the time evolution of charging or the explosion dynamics for large (nanometer) clusters.

## IV. EXPERIMENTAL METHODS

With modern molecular beam machines, the variety of radiation sources from the infrared to the x-ray regime, and the multiply parallel detection and data processing possibilities, challenging and highly sophisticated experiments on clusters can be performed. It is possible to prepare targets with narrow size distribution or even completely size selected partially at low or ultralow temperature. Vast literature exists on cluster production, e.g., Echt and Recknagel (1991), Haberland (1994), Milani and Ianotta (1999), Pauly (2000), and Whaley and Miller (2001). Optical single- or many-electron excitation, in some cases also being followed by a probing ultrashort light pulse, has led to far-reaching insight into fundamental processes of the light-matter interaction in clusters. In this section, rather than covering the vast multitude of experimental methods, we review selected current techniques used for probing dynamics on free clusters.

### A. Generation of cluster beams

*Rare-gas* or *molecular clusters* are produced from an adiabatic expansion through a continuously working or pulsed nozzle with nozzle diameters ranging from a few to 500 $\mu$m, usually restricted by the pumping speed of the apparatus. Mixed clusters are generated by a coexpansion of a gas mixture or using a pick-up technique with a cross jet. The cluster size may be varied by changing the nozzle temperature or the stagnation pressure. Typically, the width $\Delta N$ (FWHM) of the size distribution roughly equates the average number $\langle N \rangle$ of atoms per

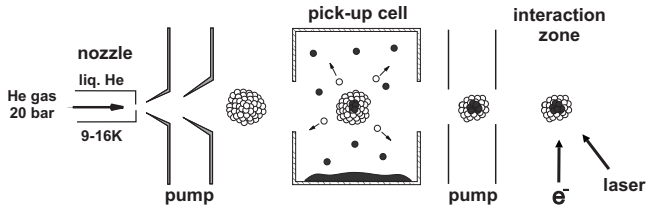


FIG. 7. Schematic of a He droplet pickup cluster beam machine. Atoms from the vapor in the pickup cell can be loaded into the droplets at 0.4 K. From Diederich *et al.*, 2005.

cluster. Semiempirical scaling laws have been derived by Hagena (1974, 1981, 1987) from general considerations about condensation kinetics. In this description, which has been simplified by Wörner *et al.* (1989), $\langle N\rangle$ scales with the "condensation parameter"

$$\Gamma^* = k\frac{p_0[\text{mbar}](d[\mu\text{m}])^{0.85}}{(T_0[\text{K}])^{2.2875}}, \tag{18}$$

where $p_0$ is the stagnation pressure, $T_0$ is the nozzle temperature, and $d$ is the effective nozzle diameter. The gas-dependent constants $k$ can be calculated from the molar enthalpy at zero temperature and the density of the solid according to Hagena (1987). If $p_0$ is given in mbar, $d$ in $\mu$m, $T_0$ in Kelvin, $k$ ranges from 185 (Ne), 1646 (Ar), 2980 (Kr) to 5554 (Xe). Equation (18) holds for monatomic gases; otherwise, the exponents of $d$ and $T_0$ are different. In the case of supersonic jets with conical nozzles, $d$ has to be replaced by an equivalent diameter that depends on the half opening cone angle. The scaling laws developed for rare gases have been modified afterward for metal vapors. Generally, $\langle N\rangle$ increases with $\Gamma^*$; for a comprehensive evaluation, see Buck and Krohne (1996).

For experiments at ultralow temperatures, helium droplet pick-up sources prove to be versatile (Goyal *et al.*, 1992; Bartelt *et al.*, 1996; Tiggesbäumker and Stienkemeier, 2007). A sketch of a typical setup is shown in Fig. 7. He droplets are produced by supersonic expansion of precooled helium gas with a stagnation pressure of 20 bars through a 5 $\mu$m diameter nozzle. By choosing the temperature at the orifice (9–16 K), the logarithmic-normal droplet size distributions can be adjusted in the range of $\langle N\rangle = 10^3 - 10^7$ atoms (low temperatures result in larger droplets). After passing differential pumping stages the beam enters the pickup chamber containing a gas target or a heated oven, where atoms are collected and aggregate to clusters inside the He droplets. With this setup it is possible to record clusters with up to 150 silver atoms (Radcliffe *et al.*, 2004) or 2500 magnesium atoms (Diederich *et al.*, 2005). Downstream another differential pumping stage, laser light or an electron beam ionizes the doped droplets. The benefits of pick-up sources rely on the feasibility to embed clusters into a well-controlled environment. In the case of He, the embedding medium is superfluid, weakly interacting, and ultracold with a temperature of about 0.4 K (Hartmann *et al.*, 1995), being an ideal nanomatrix for spectroscopic studies (Whaley and Miller, 2001). Similarly, droplets or particles of other elements might serve as pick-up medium, e.g., Ar, Kr, or Xe. Subsequent atom agglomeration can also lead to the formation of electronically excited species (Ievlev *et al.*, 2000). While in the case of helium the nanomatrix is mostly transparent under low laser intensity conditions, it may become an active part in the interaction process under strong laser fields that substantially alters the cluster dynamics. Subsequent to plasma formation in the embedded cluster, the nanodroplet may be ionized as well, giving rise to a core-shell-type nanoplasma.

Currently, *pure metal clusters* are mainly produced with laser vaporization or plasma-based methods. In both cases the material is vaporized, partially ionized, and then undergoes cooling and expansion in a rare gas. This can be pulsed, allowing for a hard expansion of the seeded clusters into vacuum or continuously streaming at lower pressure. In a *laser vaporization cluster source* a rotating target rod or plate of the desired material is mounted close to a piezodriven or magnetically driven pulsed gas valve. Usually He pulses with an admixture of Ne or Ar at backing pressures of 2–20 bars serve as seeding gas. Intense ns laser light pulses with about 100 mJ/pulse erode target material by producing a plasma plume, which is flushed by the seeding gas through a 1 mm diameter channel and a nozzle into high vacuum. The close contact with the cold gas leads to supersaturation and efficient aggregation already in the source channel. The nozzle, often elongated by an extender, can be cone shaped or merely be a cylinder. In some cases an additional small mixing chamber between source body and extender might increase the intensity within a desired mass range. Depending on material and operation conditions, different types of nozzles are in use, partially with long extenders of 10 cm or more. There is no optimal photon energy, but the intensity must be sufficient to induce vaporization or create a plasma. However, a frequency-doubled Nd doped yttrium aluminum garnet laser (YAG) is often used as its green color facilitates the beam adjustment. With laser vaporization sources all solid materials can be vaporized. As a significant fraction ($\sim$10%) of the clusters is charged, no additional ionization is necessary for studies on mass-selected species.

Several types of plasma-based sources are commonly used, the most prominent being the *magnetron sputtering cluster source*, going back to developments of Haberland *et al.* (1992). The basic erosion process is high pressure (1 mbar) magnetron sputtering. This versatile tool operates with a few cm in diameter plane solid target mounted close to an axial permanent magnet (see Fig. 8). In the presence of the seeding gas, a high voltage between a ring-shaped electrode and the target initiates and drives a discharge, efficiently eroding the material and producing a circular well after several hours of operation. The mainly charged vapor is cooled by the seeding gas and transported through a nozzle. Conducting materials can be sputtered by this source, whereas ferromagnets may cause difficulties.

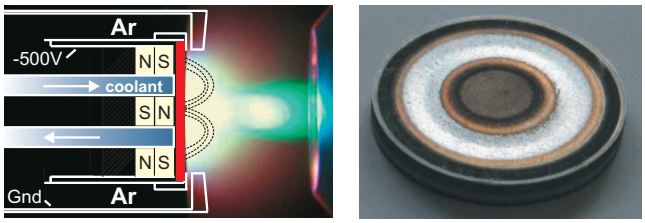


FIG. 8. (Color) Plasma plume of an uncovered Haberland-type magnetron sputtering cluster source during operation. The ion and electron motion is guided by permanent magnets behind the target. Right: Picture of a used silver target.

In contrast to the magnetron sputtering source which operates with a high voltage discharge, *arc cluster ion sources* (ACISs) make use of high current arcs. Such are known as vacuum arcs, self-stabilizing at about 40 V and 40 A. The discharge can be sustained in vacuum once a spark has initially brought some metal into the vapor phase. It is important that the discharge is carried by the metal vapor rather than the seeding gas. In order to accomplish this, the temporal development of the high voltage-driven arc needs special care. Once the metallic component in the source rules the conductivity, the discharge voltage switches to a low level so that the seeding gas will not directly be ionized. Two variants of the arc sources are in use, pulsed ones and continuously working ones. The concept of the pulsed arc cluster ion source (PACIS) (Siekmann *et al.*, 1991; Cha *et al.*, 1992) is similar to the laser vaporization cluster source, only that the laser is replaced by a pulsed high-current arc between two electrode rods at about 1 mm separation. An offspring of the PACIS uses one rotating electrode, called "pulsed microplasma source" (Barborini *et al.*, 1999). When operated continuously we obtain the ACIS (Methling *et al.*, 2001; Kleibert *et al.*, 2007). Here the target is a water-cooled hollow cathode, where a water-cooled counterelectrode serves as the anode. Magnet coils around the hollow cathode help to control the arc. Again, the plasma is flushed by an inert seeding gas into vacuum, producing a cluster beam with a high amount of charged species (about 80%, depending on the material). The beam from the ACIS can be focused by aerodynamical lens systems. These are sets of orifices and/or confining tubes connected to the nozzle. By choosing appropriate dimensions the on-axis intensities increase, which go along with a narrowing of the particle size distribution (Passig *et al.*, 2006). This type of source can generate large metal particles from 2 to 15 nm in diameter, an interesting size range for future studies of the intense laser-cluster interactions.

All cluster sources described above are housed inside well-pumped vacuum chambers in order to reduce the gas load at the point of investigation. Ideally, only the central filament of the jet passes a narrow skimmer and enters the photoexcitation chamber as a collimated cluster beam. Further differential pumping can lead to sufficiently low pressure for the spectroscopy on isolated species. However, many strong-field experiments do not make use of single cluster excitation. In particular for rare-gas clusters, the laser is often focused onto the beam in the high pressure zone close to the nozzle. For such cases many interacting clusters are simultaneously excited; thus the observed signal might originate from a dense cluster ensemble rather than from isolated systems.

### B. Sources for intense radiation

Within the past 20 years ultrashort-pulse lasers have undergone dramatic improvements with respect to pulse width, power, and repetition rate. This was first accomplished with the technique of colliding pulse mode locking within a ring dye laser (Fork *et al.*, 1981) and later by the invention of the chirped pulse amplification scheme by Maine *et al.* (1988). Nowadays, the broadband fluorescent (690–1050 nm) laser crystal Ti:sapphire operating at a central wavelength of 800 nm is the workhorse in delivering ultrashort and intense optical radiation. Laser pulse durations as short as a few femtoseconds (Brabec and Krausz, 2000; Keller, 2003) or attoseconds (Corkum and Krausz, 2007) as well as pulse powers in the petawatt regime (Ledingham *et al.*, 2003) are available. To avoid damage of the optical components, the pulses from a mode-locked femtosecond laser oscillator are first stretched to a few ps before amplification and then re-compressed in the final step (Maine *et al.*, 1988). For energy enhancement regenerative amplifiers or bow-tie-shaped multipass configurations are typically used. Stretching as well as compression of the pulse is achieved by introducing diffractive elements, e.g., reflection gratings (Strickland and Mourou, 1985) in the optical path. High energy pulses in other wavelength regions can be realized, e.g., by amplification of the third harmonic in a KrF amplifier operating at 248 nm (Bouma *et al.*, 1993). Due to the limited bandwidth of the transition the pulse duration in this type of laser is limited to a few hundred femtoseconds. With high harmonics (HH) generated by focusing intense pulses into atomic gases the short-wavelength regime becomes accessible opening up the route toward attosecond pulses (Papadogiannis *et al.*, 1999). Pulse intensities as high as $1.3\times10^{13}$ W/cm$^2$ have been reported for the 27th harmonic (Nabekawa *et al.*, 2005). A new and very powerful radiation source, i.e., the vacuum ultraviolet free-electron laser FLASH (free electron laser in Hamburg) at DESY has been established in 2005. It delivers pulses with wavelengths down to 6.8 nm at pulse energies up to 100 $\mu$J (Ayvazyan *et al.*, 2006; Tiedke *et al.*, 2009), with the current update 4 nm will be reached. Another soft x-ray free electron laser, i.e., the Spring-8 compact SASE source (SCSS) has been installed in Japan. Only recently the first hard x-ray free electron laser showed the feasibility to generate laser radiation down to 0.15 nm. This "linac coherent light source" (LCLS) at Stanford will allow, e.g., studies on coherent inner shell excitations of clusters.

In the optical domain single-shot autocorrelators or more sophisticated setups (Trebino, 2002) are applied for pulse characterization. In many experiments only the pulse width is varied by detuning the compressor length.

This introduces a linear chirp (Sec. II.B) and allows continuous variation of the pulse duration from sub-100-fs to many ps. To generate dual-pulses with variable optical delay (pump and probe) the initial pulse may be split into two replicas, e.g., by a Mach-Zehnder setup. Moreover, liquid crystal spatial light modulators, acousto-optical modulators, and deformable mirrors allow one to modify the pulse structure at will (Weiner, 2000). Besides amplitude and phase, the polarization can also be altered, e.g., to drive reactions selectively into a desired channel in coherent control experiments (Tannor *et al.*, 1986; Brumer and Shapiro, 1995). This scheme connected to a feedback algorithm (Judson and Rabitz, 1992) is capable of optimizing the laser-matter coupling [see, e.g., Assion *et al.* (1998) and Sec. VII.A].

For pulse focusing, lenses or parabolic mirrors can be used. The latter avoids pulse modification due to the propagation through optical elements, i.e., pulse broadening, self-focusing, or phase modulation. The waist radius of a Gaussian beam at the focus is $w_0 = 2\lambda f/\pi$, where the $f$ number relates the size of the unfocused beam diameter $D$ to the focal length of the lens $d_f$ by $f = d_f/D$ and $\lambda$ is the wavelength. Typical spot sizes are a few tens of $\mu$m. For a quantitative description of nonlinear laser-matter interactions the intensity profile in the focal region has to be taken into account. For a given peak intensity $I_0$, the intensity profile $I(r,z)$ is given by (Milonni and Eberly, 1988)

$$I(r,z) = \frac{I_0}{1 + z^2/z_0^2} \exp\left[ - \frac{2r^2}{w_0^2(1 + z^2/z_0^2)} \right], \tag{19}$$

where $r$ and $z$ are the axial and transverse distances to the focus and $z_0 = \pi w_0^2/\lambda$ specifies the Rayleigh length, where the beam radius has increased to $\sqrt{2}w_0$. The focal intensity profile leads to volumetric weighting, which has been used to determine intensity thresholds in the strong field ionization of atoms (Hansch *et al.*, 1996; Goodworth *et al.*, 2005; Bryan *et al.*, 2006) and molecules (Benis *et al.*, 2004). Applied to clusters, this intensity-selective scanning method has revealed a dramatic lowering of the threshold intensities for producing highly charged ions when compared to atoms (Döppner, Müller, *et al.*, 2007; Döppner *et al.*, 2009).

### C. Particle detection techniques

The optical excitation of clusters can lead to extensive fragmentation. Usually fragment mass spectra are analyzed in terms of stabilities similar to nuclear fission processes (Schmidt *et al.*, 1992). In strong fields, however, dedicated techniques are needed to resolve the emission spectra of ions and electrons in detail.

#### 1. Determination of charge state distributions

The most straightforward method to determine charge state distributions of clusters and their fragments is ion mass spectrometry. Irrespective of the particular method, the mass separation will always be connected to the charge-to-mass ratio. In particular time-of-flight (TOF) methods with accelerating electrical fields are widely used for analyzing charged products after photoionization. Figure 9 shows an example of highly charged atomic ions emerging from silver clusters embedded in He droplets after irradiation with intense fs laser light. The TOF spectrum exhibits contributions of He and Ag clusters with high masses (not shown here). At short flight times a situation appears as in Fig. 9. Whereas the background peaks are signatures of the He droplet fragments, the highlighted series can uniquely be assigned to atomic ions in high charge states from the Coulomb explosion of $Ag_N$. As a matter of fact, the Ag ions carry high recoil energies due to the violent expansion. Therefore TOF methods that use an acceleration of the ionic ensemble by electric fields in the few kV range loose part of their resolution and transmission. Consequently, the TOF spectra prove the occurrence of the ions but do not fully image the real charge state distribution.

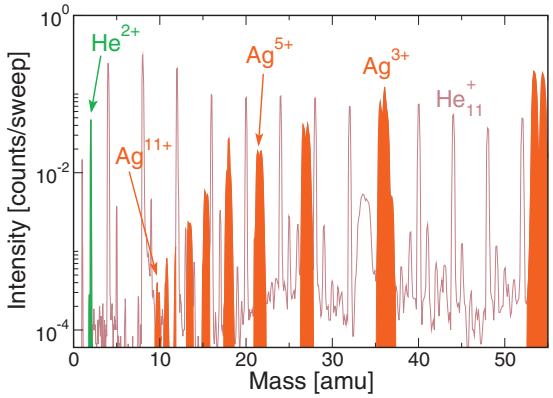


FIG. 9. (Color) Charge state spectrum from a time-of-flight analysis of $Ag_N$ in He droplets with $\langle N \rangle = 40$ exposed to 400 fs laser pulses at $4 \times 10^{13}$ W/cm$^2$ and 800 nm. The resulting $Ag^{q+}$ signals from the Coulomb explosion are highlighted. Ions with up to $q = 11$ are detected. The occurrence of $He^{2+}$ stems from charge transfer with the Ag ions. From Döppner *et al.*, 2005.

#### 2. Acquisition of ion recoil energy spectra

A simple and versatile tool to investigate ion recoil energies is the acceleration-free TOF spectroscopy. Two preconditions have to be met in order to allow a unique interpretation of the results. First, there has to be a defined source point for the ion emission. Second, the nature (mass) of the ions must be known, which is often a point difficult to achieve. However, the excitation of single-element clusters with sufficiently strong laser fields leads to complete fragmentation into atomic ions with known mass. In this case, the kinetic energy is determined by TOF measurements through a field-free drift tube of about 0.5 m, without an initial electric field. For reducing noise caused by secondary electrons and, moreover, to restrict the ion detection to the Rayleigh region of the laser focus, an adjustable narrow slit confines the ion trajectories. Resulting TOF spectra can then directly be converted into kinetic energy spectra [see, e.g., Fig. 1(d)].

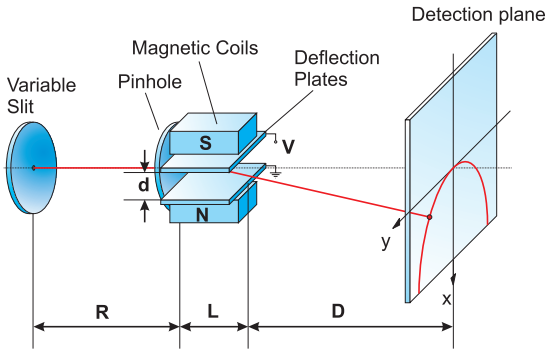


FIG. 10. (Color) Sketch of the Thomson analyzer. Ions enter a region of parallel electric and magnetic fields through a tiny hole. The resulting deflection gives characteristic parabolas from which the charge state selective recoil energy can be deduced. A multichannel plate detector with an imaging system serves to record the data. From Döppner *et al.*, 2003.

The field-free ion TOF yields recoil energies irrespective of the ion charge states. For a detailed analysis it is necessary to resolve charge-state-dependent recoil energies. To this end two methods have successfully been applied, both of which simultaneously measure the ion charge state and energy. The first method uses magnetic deflection time-of-flight (MD-TOF) mass spectrometry (Lezius *et al.*, 1998). This technique is based on TOF measurements at different positions behind a magnetic field. With the MD-TOF, highly energetic (up to 1 MeV), multiply charged ions could be recorded.

The second method is of static nature and based on a principle first applied by Thomson (1907). Figure 10 shows the Thomson analyzer for the simultaneous measurement of energy and charge of ions expelled from an exploding cluster. It consists of parallel electric and magnetic fields, followed by a field-free drift zone in connection with a position-sensitive detector. The experimentally obtained raw data reflect momentum and energy per charge and have to be transformed to energy versus charge spectra. For $Ag_N$ the charge-state-resolved ion energy distribution is rather narrow and the maximum energy grows almost linearly with ionization stage (Döppner *et al.*, 2003).

#### 3. Energy and angular-resolved electron detection

The experimental challenge in photoelectron spectroscopy results from the notoriously low densities in mass-selected charged cluster beams. To cope with this, time-of-flight electron spectroscopy has been developed with a magnetic field gradient. When the clusters are ionized at a certain spot within an electron *magnetic bottle spectrometer* the complete photoelectron spectrum can be recorded by time-of-flight measurements with up to 100% detection efficiency (Kruit and Read, 1983; Ganteför *et al.*, 1988; Arnold *et al.*, 1991; Taylor *et al.*, 1992). Whereas this method turned out to be extremely fruitful to reveal the electronic level structure of many mass-selected cluster anions, the magnetic fields involved hamper the retrieval of angular information. In the case of a neutral cluster beam, the target density can be sufficiently high in order to obtain a spectrum even without the magnetic field. Electron emission and drift occur within a field-free tube, equipped with a time-resolving detector. By rotating the polarization direction of the laser, angular-resolved photoelectron spectra are obtained. Increasing the length of the drift tube increases the energy resolution at the expense of signal intensity. Acceptable results can be achieved with a magnetically well-shielded tube of about 0.5 m length.

In contrast to the electron TOF method, where kinetic energy release information is contained in the electron drift times, imaging techniques extract energy and angular distributions by spatially resolving the signal by using position sensitive detectors. The advantage of this method is that the full emission characteristics can be reconstructed from the two-dimensional (2D) image by means of an Abel inversion. The energy resolution is limited by the quality of the 2D detector (Heck and Chandler, 1995). An improvement in the 2D imaging technique has been obtained by introducing a lens optics which maps all particles with the same initial velocity vector onto the same point of the detector, compensating for their initial emission position (Eppink and Parker, 1997). So far this technique has mainly been used to record low-energy electron spectra. With a modified electrode configuration energetic electrons from clusters driven to Coulomb explosion are accessible as well (Skruszewicz *et al.*, 2009).

## V. SINGLE-PHOTON AND MULTIPHOTON PROCESSES IN CLUSTERS

The previous sections provided the basic tools for the description and analysis of laser-induced cluster dynamics. In the following we present examples with single-photon processes in Sec. V.A and multiphoton effects in Sec. V.B. In both cases clear signatures of the photon energy persist. Single-photon excitations are typically investigated by photoelectron spectroscopy (PES), which is usually interpreted as a static image of the density of states (DOS) and indirectly gives information about the underlying geometry. When carried out with angular resolution, PES reveals structural details of the electronic orbitals being excited. However, even single-photon photoemission goes beyond a mapping of system properties in a static and direct way, as it reflects a dynamical process. Pump-probe studies, as a time-resolved version of PES, give access to ultrafast structural dynamics and energy redistribution pathways. Additional reaction channels emerge with the absorption of multiple photons, as discussed in Sec. V.B. Besides above-threshold ionization as a prime example for multiphoton signatures, thermalization and its effect on electron spectra will also be discussed. Other issues are plasmons, which often govern the response of metal clusters and become broadened by nonlinear contributions at higher intensity. However, they remain a dominant doorway process up to the strong-field domain, which is the subject of Sec. VI.

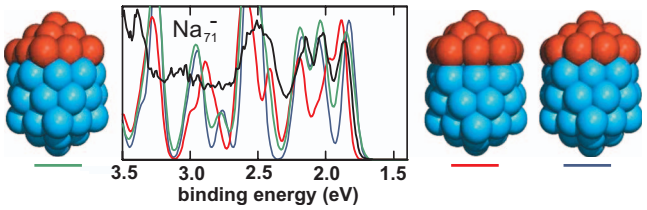


FIG. 11. (Color) PES spectrum of $Na_{71}^-$: experimental result (black curve) from nanosecond laser excitation with $\hbar\omega = 4.02$ eV at $T \simeq 100$ K and theoretical DOS calculated by DFT using different ground-state structures (as shown). From the matching of the spectra the left structure is favored while the right ones show less agreement. From Kostko *et al.*, 2007.

### A. Single-photon electron emission

#### 1. Probing the density of states

For studying single-electron excitations by photoemission, it is often useful to assume, motivated by Koopmann's theorem (Weissbluth, 1978), that the essential structures of the electronic and ionic systems do not change significantly upon electronic emission. The photoelectron energy spectrum thus basically images the DOS. Based on this assumption, PES has become a powerful tool to explore the electronic structure of mass-selected clusters. Figure 11 shows an example from $Na_{71}^-$. The experimental data (black curve) exhibit pronounced peaks at binding energies between 1.8 and 3.5 eV. Such *electronic fingerprints* reveal details of the quantum confinement and change dramatically with cluster size or structure. With DFT calculations it has become possible to obtain theoretical DOS for comparison with experimental PES spectra. Figure 11 shows an attempt to identify the cluster ground state geometry out of theoretically suggested candidates by matching the DOS. A vast amount of photoelectron spectra on different systems has been accumulated since the first successful experiments (Leopold *et al.*, 1987; Ganteför *et al.*, 1988; Pettiette *et al.*, 1988; McHugh *et al.*, 1989; Cheshnovsky *et al.*, 1990; Ho *et al.*, 1990; Ganteför *et al.*, 1996). Over time, developments in cluster production and electron detection have made it possible to cover large size ranges at high energy resolution. For instance, from Wrigge *et al.* (2002), PES spectra of $Na_N^-$ for $N = 31-500$ showed peaks that can be assigned to the electronic shell structure. For small systems a higher level of theoretical understanding can be obtained from *ab initio* quantum chemical methods (Bonačić-Koutecký *et al.*, 1991).

To date, most PES studies rely on low-energy photon excitations, i.e., *valence-band* PES. Inner-shell photoionization, i.e., *core-level* PES, has also been demonstrated (Wertheim, 1989; Eberhardt *et al.*, 1990; Siekmann *et al.*, 1993). These studies, however, dealt with deposited clusters excited with high photon energy lamps or synchrotron radiation. Common results are shifts of core levels with cluster size. Due to the surface contact a thorough understanding remains difficult since core-hole screening, chemical shifts, electronic relaxation, or charge transfer dynamics contribute to the spectra.

With third-generation synchrotron sources, experiments on free neutral (not mass-selected) clusters became possible. One issue of such studies is the absorption site as a probe of the local environment (Hatsui *et al.*, 2005; von Pietrowski *et al.*, 2006). In rare-gas clusters the measured line profiles (Tchaplyguine *et al.*, 2004) show well-separated features that can be attributed to the ionization of surface and volume atoms (Amar *et al.*, 2005; Bergersen *et al.*, 2006). Such analyses can also provide an indirect size measurement, as recently shown for neutral nanometer clusters of various metals, i.e., Na (Peredkov *et al.*, 2007a), Pb (Peredkov *et al.*, 2007b), Cu, and Ag (Tchaplyguine *et al.*, 2007).

Latest progress in core-level PES has been achieved at the free electron laser FLASH which delivers intense pulses with up to 200 eV photon energy. The energy range and high brilliance open new possibilities to interrogate both the complete valence regions and shallow core levels of numerous systems. For example, PES on free mass-separated $Pb_N^-$ revealed a pronounced $N$-dependent shift of the $5d$ core level (Senz *et al.*, 2009), which is in accordance with the metallic droplet picture for large $N$. However, strong deviations starting below $N \leqslant 20$ indicate less effiocient core-hole screening, hinting at a transition from metallic to nonmetallic bonding.

A solid theoretical understanding of the photoionization process requires the complete toolbox of computational many-particle physics. One example where DFT calculations for $Na_{71}^-$ are compared to experimental PES was shown in Fig. 11. In the same spirit, $Si_N^-$ for $N = 20-26$ has been investigated theoretically by Guliamov *et al.* (2005) and compared to data from Hoffmann *et al.* (2001). In both cases, not all peaks could be fully reproduced by theory, especially for deeply bound electronic states. Nevertheless, from comparison of the calculated DOS with the experiment the ground-state geometry can often be identified and discriminated against competing isomers. Remaining discrepancies reflect that static DFT calculations based on the Kohn-Sham eigenvalues are insufficient to fully describe photoemission. It is well known that the interpretation of eigenvalues as single-particle energies requires attention (Mundt *et al.*, 2006; Kümmel and Kronik, 2008). This concerns the meaning of single-particle eigenvalues itself as well as dynamical aspects as Koopmann's theorem does not hold in a strict way. In other words, photoemission is a highly correlated process. The photoelectron interacts with the residual system during its removal and may substantially modify the level structure. The effect becomes important with low energy electrons and dramatic in zero electron kinetic energy measurements.

The question whether PES reflects parent or daughter cluster DOS or a dynamical mixture of both has been tackled in the case of sodium cluster anions (see Fig. 12). Comparison between the experimental spectrum (Moseler *et al.*, 2003) and the Kohn-Sham eigenvalues of the (*parent*) cluster anion calculated with average-density self-interaction correction (ADSIC) is not satis-

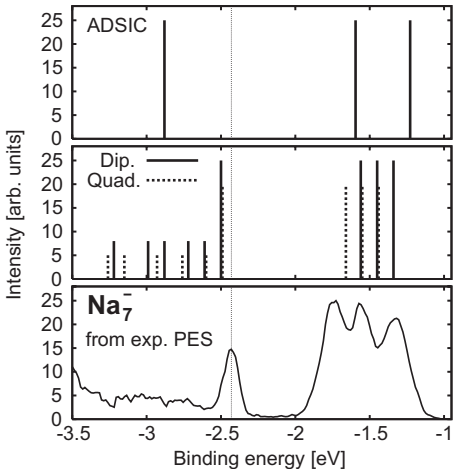


FIG. 12. Comparison of measured PES spectra for $Na_7^-$ (lower panel) (Moseler *et al.*, 2003) and two different theoretical predictions. The upper panel shows the single-electron levels from a (static) Kohn-Sham calculation applying ADSIC. The middle panel shows the theoretical result deduced from the excitation spectrum of neutral $Na_7$, the final product after photoemission. The excitations were computed with TDLDA (Mundt and Kümmel, 2007).

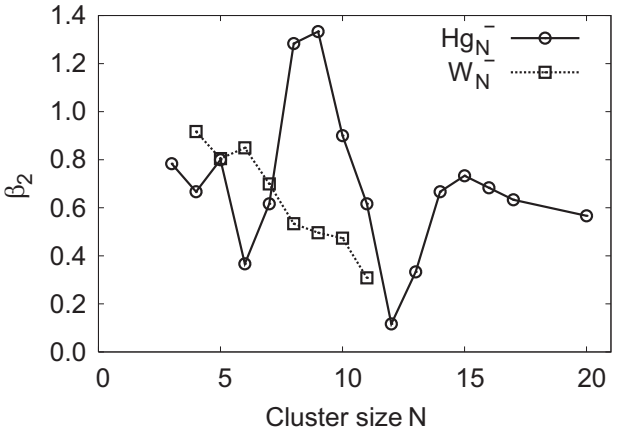


FIG. 13. Anisotropy parameter $\beta_2$ extracted from photoelectron angular distributions as a function of cluster size $N$: $W_N^-$ (squares) exposed to 4.025 eV laser light (from Pinaré *et al.*, 1999) and $Hg_N^-$ (circles) irradiated at 3.15 eV (from Verlet *et al.*, 2004). For tungsten, a smooth decrease in the characteristic emission parameter $\beta_2$ is observed as function of size. Instead, mercury clusters show pronounced oscillations in $\beta_2$ up to $N=15$.

factory (Legrand *et al.*, 2002). A way to circumvent the use of the Kohn-Sham eigenenergies is to perform a time-dependent DFT calculation of the response to a small perturbation. Mundt and Kümmel (2007) have extracted the energies of excited states of the neutralized *daughter* cluster from the time evolution of the dipole and quadrupole moments and converted the data to photoelectron kinetic energies by assuming energy conservation (middle panel). While some discrepancies still remain there is substantial improvement over mere static considerations which points out the key role of final state interactions.

### 2. Angular distributions

Besides pure energy spectra, which reflect the electronic level structure, photoemission may also reveal details of the involved orbitals and thermalization phenomena. Therefore, the emission has to be analyzed with angular resolution, a subject that is still in its early stage. The directionality of the photoelectron angular distribution (PAD) can be quantified by a Legendre expansion,

$$\frac{d\sigma(\theta)}{d\Omega} = \frac{\sigma_{\text{tot}}}{4\pi}[1 + \beta_2 P_2(\cos\theta) + \beta_4 P_4(\cos\theta) + \cdots], \tag{20}$$

where $\theta$ denotes the emission angle with respect to the laser polarization axis. The anisotropy parameter $\beta_2$ ranges from $-1$ (emission perpendicular to polarization), over 0 (isotropic emission), to 2 (emission parallel to polarization) and depends on the orbital symmetry of the initial and final states and the electron kinetic energy.

So far only a few PAD experiments have been performed on clusters. Among them are results on $W_N^-$, $N=4-11$ (Pinaré *et al.*, 1999; Baguenard *et al.*, 2001), and $Hg_N^-$, $N=3-20$ (Verlet *et al.*, 2004). The corresponding $\beta_2$ evolutions as a function of $N$ are shown in Fig. 13. For $W_N^-$, $\beta_2$ changes from a more directed behavior with small clusters ($\beta_2 \sim 1$) to nearly isotropic emission ($\beta_2 \to 0$) when $N \to 11$. From the rapidly reached isotropic behavior it was concluded that larger $W_N^-$ showed an indirect emission process, where electron-electron collisions lead to a loss of coherence. This is in agreement with the tendency of $W_N^-$ to undergo thermionic emission (Leisner *et al.*, 1991). Figure 13 also shows results on $Hg_N^-$ with strongly size-dependent asymmetries. Although the physical origin of these $\beta_2$ fluctuations could not be clarified yet, the data illustrate the high system sensitivity of angular-resolved photoemission.

A clear dependence of the PAD on the initial electronic level of the photoelectron was demonstrated with medium-sized $Na_N^-$ (Bartels *et al.*, 2009). Exemplarily, Fig. 14 compares a standard PES spectrum of $Na_{58}^-$ (top) with the corresponding angular-resolved result (bottom panel). The peaks in the top panel can be attributed to emission from the $2p$, $1g$, and $2d$ shells [see Brack (1993) and de Heer (1993) for details on the shell nomenclature]. For a given photon energy, comparison with the PAD shows that the $2p$ and $2d$ electrons are emitted parallel to the laser polarization, while the $1g$ emission is aligned perpendicularly. This highly shell specific directionality indicates a coherent photoemission process without significant contributions from electron-electron and electron-photon scattering. Furthermore, similar angular distributions for electronic sublevels of a particular shell (e.g., $1g$) show that the ionic background does not destroy the free angular momentum eigenstate character within an electronic shell. Thus, the results justify a single-particle picture of al-

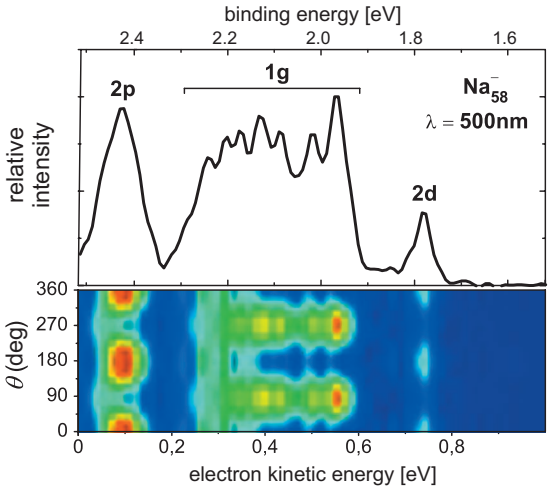


FIG. 14. (Color) Photoemission from $Na_{58}^-$ obtained with 3.15 eV photon energy. The top panel shows angle-integrated spectra, while the bottom panel shows the corresponding angular-resolved results. The emission angle $\theta$ is defined with respect to the laser polarization. From Bartels *et al.*, 2009.

most free delocalized electrons for describing the PAD from simple metal clusters.

Besides state sensitivity, PAD spectra are also dependent on the photon energy. A theoretical study of this effect was reported by Pohl *et al.* (2004b). Figure 15 shows angular distributions for three excitations close to and far above the ionization threshold by considering a pre-aliged cluster. The patterns depend on $\hbar\omega_{\rm las}$ and reflect that the nodal structure of the outgoing wave $\varphi_{\mathbf{k}}(\mathbf{r})$ changes with momentum $\mathbf{k}$. Note that the latter is asymptotically related to the excitation energy by $|\mathbf{k}| = \sqrt{2m(\hbar\omega_{\rm las} - E_{\rm IP})}/\hbar$. Systematic scanning of $\hbar\omega_{\rm las}$ modulates the zeros and maxima of $\varphi_{\mathbf{k}}$ and thus in principle allows one to systematically probe the orbitals of cluster electrons and, in turn, the background ionic field. Therefore, PAD is a promising method to gain insight into structural cluster properties. As we shall see below, photoelectron spectroscopy is also an excellent tool for time-resolved analysis of dynamical processes.

### 3. Time-resolved analysis

Excited states populated by cluster photoactivation can decay in different manners, i.e., by emission of radiation, by internal conversion with energy transfer to the ionic degrees of freedom, or by Auger processes. The real time dynamics of such processes can in principle be explored by tracing the occupation and spectral positions of electronic states within time-resolved PES (TRPES). For example, structural changes of the ionic frame might open fast radiationless decay channels due to transient crossings of the potential energy curves of the excited and ground states (conical intersection). The depletion of the excited level, when explored in TRPES experiments with fs pump-probe techniques, offers insight into internal energy conversion processes and ionic relaxation time scales. Below we discuss two recent examples.

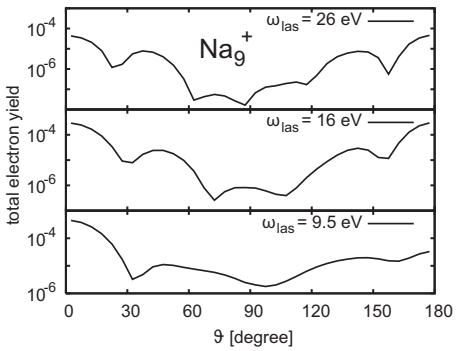


FIG. 15. Photoelectron angular distribution of $Na_9^+$ irradiated with three different laser energies as indicated, calculated in TDDFT. From Pohl *et al.*, 2004b.

TRPES on mass-selected $Ag_N^-$ with $N$=3–21 has been investigated in a two-color pump-probe experiment (Niemietz *et al.*, 2007) using a 1.55 eV pump photon safely below the vertical detachment energy (VDE). Figure 16 shows a series of spectra from $Ag_{19}^-$ obtained for time delays up to 5 ps. The peak at 1.82 eV observed in the top panel is consistent with the value of the VDE from the 1*f* level previously excited by the pump pulse. The feature then shifts with time to lower kinetic energies (higher binding energy) and stabilizes between 1.1 and 1.5 eV after about 1.3 ps (see arrow). Subsequently this peak loses intensity and vanishes after about 5 ps. This evolution can be explained by a continuous Jahn-Teller deformation of the excited cluster which eventually opens a nonradiative transition channel to the ground-state potential. For $Ag_{19}^-$, the decay time is estimated to be 630 fs, i.e., much shorter than for radiative transitions.

Another example on gold cluster anions revealed an extremely strong size dependence of the excited-state lifetime. More specifically, $Au_6^-$ shows an exceptional long lifetime of more than 90 ns (Walter *et al.*, 2007). Corresponding DFT and linear-response TDDFT calculations predict decay times of 730 ns. In contrast, $Au_7^-$ and $Au_8^-$ show clear indications for fast internal conversion on the ps time scale driven by ionic motion. As shown in Fig. 17(a), the excited-state peak in the experimental data of $Au_7^-$ is initially observed around a binding energy of 2 eV. This value just reflects the energy difference between the excited anion and the neutral ground state. As time evolves, the peak first slightly shifts to higher binding energies, then loses intensity, and finally becomes washed out after about 1 ps. At the same time a new feature appears between 2.4 and 2.8 eV which has reached a high signal intensity around 3 ps. The time evolution of the experimental peak maximum yields an exponential decay with a time constant of 1.8 ps. Results from a corresponding linear-response TDDFT calculation based on a propagation of an ensemble of classical trajectories "on the fly" (Stanzel *et al.*, 2007) are shown in Fig. 17(b). The calculated population dynamics show a decay time of 1.9 ps, which is in good agreement with the experimental result. Closer analysis of the calculation results reveals the following process: the excited anion relaxes toward a crossing with

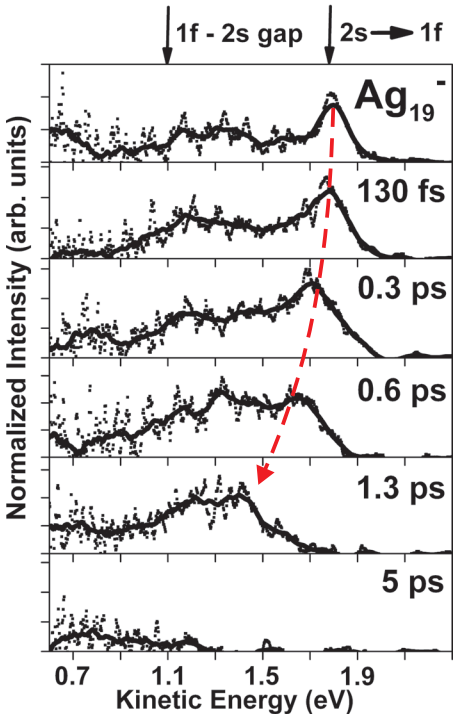


FIG. 16. (Color) Time-resolved photoelectron spectra of $Ag_{19}^-$ obtained with laser pulses of about $3\times10^9$ W/cm$^2$, $\hbar\omega_{pump}=1.55$ eV, and $\hbar\omega_{probe}=3.1$ eV. The indicated times are the delays between the pump and probe pulses. The dashed arrow emphasizes the temporal development of the initially populated 1*f* level. From Niemietz *et al.*, 2007.

the anionic ground state within about 340 fs [see the rapid lowering of the initial peak at 2 eV in Fig. 17(b)]. At the crossing the excited state begins to populate the vibrationally excited ground state. This mixing is expressed in the new feature emerging around 3.0 eV. The rapid bleaching of the 2.3 eV feature beyond 3 ps and

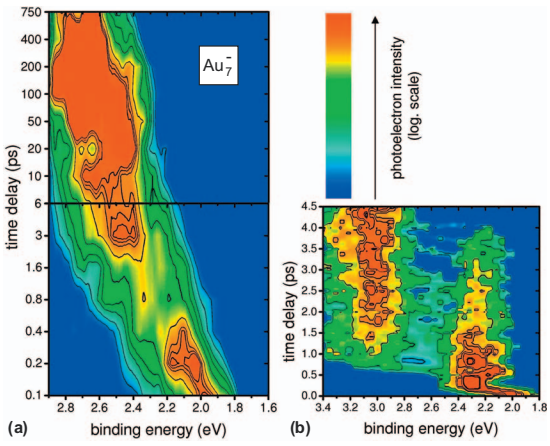


FIG. 17. (Color) Time-resolved photoelectron spectra of $Au_7^-$. (a) Experimental data obtained with 40 fs pulses at intensities below $10^{11}$ W/cm$^2$ with $\hbar\omega=1.56/3.12$ eV for pump and probe. (b) Simulated PES obtained from TDDFT coupled to ensemble MD on the fly. Note that the experimental data are plotted with a logarithmic delay axis while it is linear for the calculation results. From Stanzel *et al.*, 2007.

the stabilization of the 3.0 eV peak reflect internal energy conversion and further indicate a melting of the cluster (Stanzel *et al.*, 2007).

A more elaborate way for investigating cluster dynamics via photoemission is by recording time-resolved photoelectron angular distributions (TRPADs). The applicability of this method has been demonstrated with molecules [see Suzuki (2006)]. Femtosecond TRPAD studies on clusters have been performed by the Neumark group using imaging techniques to investigate the relaxation dynamics of small $Au_7^-$ [see Bragg *et al.* (2005)].

### B. Multiphoton signatures

At intermediate laser intensity, single-photon processes as discussed begin to be accompanied by multiphoton effects. This section is devoted to this transition region where linear and nonlinear excitations simultaneously occur. We focus on processes such as above-threshold ionization, resonance broadening, and the onset of electronic thermalization. In all cases the laser intensity remains sufficiently low to resolve the influence of the chosen photon energy.

#### 1. Competition of linear and nonlinear excitations

Both single-photon and multiphoton processes can be demonstrated with the example of photoelectron spectroscopy on $Hg_{14}^-$ (see Fig. 18) (Verlet *et al.*, 2004). These spectra are extracted from PAD measurements [see the polar plots in Figs 18(a)–18(c) and the corresponding angle-integrated results at the bottom]. Mechanisms leading to specific peaks are schematically indicated in the top panels. Process A depicts the direct emission of the extra electron in the 6*p* level with one high-energy photon or with two low-energy photons. No excitation energy is transferred to other decay channels and the peak labeled A reflects the energy of the photons and the VDE of the 6*p* electron. Other pathways leading to electron emission are feasible if the photon energy exceeds the *s*-*p* band gap: single-photon detachment of an electron in the 6*s* band (case E); two-photon interband excitation of an electron from the *s* band via the *p* band (processes C and D); or single-photon Auger processes, labeled B. The latter excitation scheme is observed in the spectra as broad features with an onset consistent with the VDE of the *s* and the *p* bands in $Hg_{14}^-$. This example thus demonstrates the complex pathways in a seemingly simple case of laser-exposed clusters.

The scenarios exemplified in Fig. 18 call for a more detailed theoretical analysis. Some studies in the simpler case of Na clusters were performed in the framework of TDLDA-MD (Pohl *et al.*, 2003, 2004a). We concentrate on the impact of intermediate states in multiphoton induced photoemission (Pohl *et al.*, 2001). In this laser intensity regime, the electron single particle energy $\varepsilon_0$ is *a priori* deduced from the recorded electron kinetic energy by

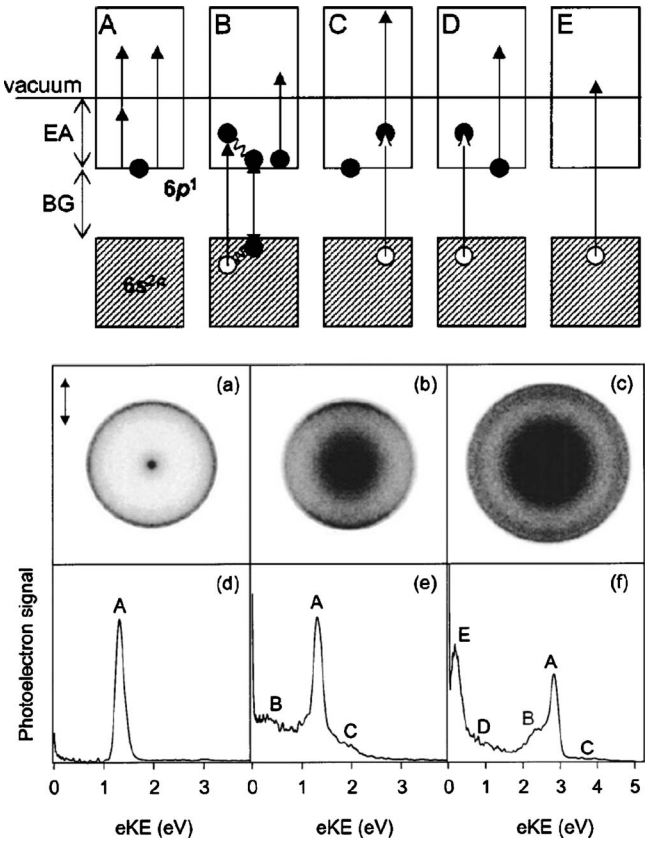


FIG. 18. Demonstration of different electron emission pathways from negatively charged mercury clusters. Top: Sketch of the pathways in terms of the band structure. Note that before irradiation the additional electron is located above the band gap (BG) of the corresponding neutral system. Bottom: Angular-resolved and integrated photoelectron spectra of $Hg_{14}^-$ at different photon energies, (a) and (d) with $\hbar\omega_{las}=1.57$ eV, (b) and (e) with $\hbar\omega_{las}=3.15$ eV, and (c) and (f) with $\hbar\omega_{las}=4.58$ eV. The labels correspond to the processes sketched in the top panel. From Verlet *et al.*, 2004.

$$E_{kin} = \varepsilon_0 + \nu\hbar\omega_{las}, \tag{21}$$

where $\nu$ is the number of photons involved. Finding such a multiphoton process is in principle straightforward as the signal shifts according to the change in the photon energy. The picture becomes more complicated if an intermediate state (say, of energy $\varepsilon_1$) can be populated by a one or multiphoton process from an initial state $\varepsilon_0$. Then the original direct $\nu$-order process competes with a sequential $\nu-1$ (or $\nu-2,\ldots$) process from state $\varepsilon_1$. Since sequential processes are less shifted than direct ones, discrimination is again possible by slightly changing the photon energy. A somewhat similar situation occurs when the photon energy is close to the plasmon excitation (Pohl *et al.*, 2001). In this case the spectra exhibit contributions pinned to the resonance energy.

The plasmon plays a major role in the optical excitation of simple metal clusters [see, e.g., Fig. 1(b) for experimental examples]. At higher laser intensities where the details of level spectroscopy got lost the plasmon remains quite robust. This is shown in Fig. 19 for $Na_{41}^+$

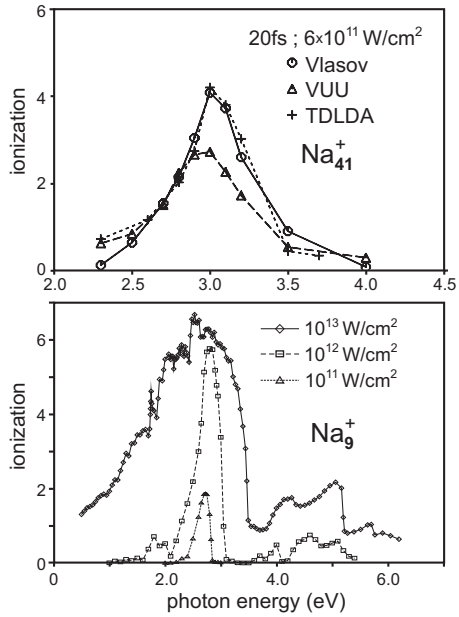


FIG. 19. Calculated total ionization of sodium clusters vs laser frequency. Top: Comparison of the total valence electron emission from $Na_{41}^+$ calculated with TDLDA, Vlasov, and VUU calculations as a function of photon energy for excitation with a 20 fs Gaussian laser pulses of intensity $I=6\times10^{11}$ W/cm$^2$ (Giglio *et al.*, 2003). Bottom: TDLDA results of the valence electron emission from $Na_9^+$ over photon energy for excitation with 100 fs pulses for three different intensities (as indicated). From Ullrich *et al.*, 1997.

and irradiation with about $10^{12}$ W/cm$^2$ (top panel). The plasmon peak centers around 3 eV and a comparison between various calculations is performed. The high number of emitted electrons calls for calculations going beyond the mean field and thus requires inclusion of dynamical correlations and electron-electron collisions, as is done, e.g., with VUU. However, the strong impact of the plasmon is obvious in all models. As it provides a resonant coupling channel, enhanced energy absorption and increased electron emission are observed (Calvayrac *et al.*, 2000). It should be noted that TDLDA-MD and Vlasov-LDA-MD match almost perfectly except for details in the tail of the distributions (e.g., at 3.5 eV). The peak height for VUU is lower than for the pure mean-field approaches due to damping of the resonance by electron-electron collisions. This damping (or resonance broadening) leads to a higher absorption (Köhn *et al.*, 2008) and slightly enhances ionization for off-resonant excitation.

The nonlinear nature of the response can be probed directly by varying the laser intensity (see the bottom panel of Fig. 19). Although the calculations on $Na_9^+$ have been restricted to the TDLDA level (no dynamical correlations), they qualitatively reflect major trends. In general, the yield is maximal for photon energies in the vicinity of the plasmon. The peak height strongly increases with laser intensity but does not show a linear scaling—a clear sign of nonlinearity of the response. In addition, the shape of the spectrum is substantially al-

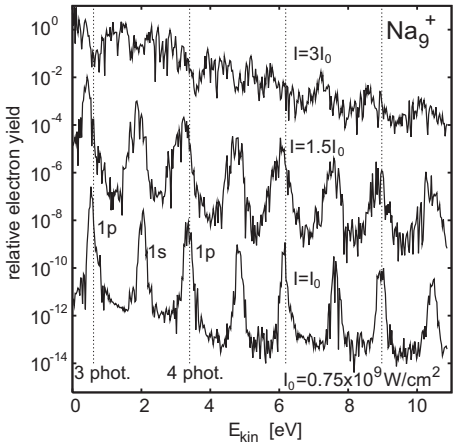


FIG. 20. Photoelectron spectra from $Na_9^+$ exposed to 100 fs laser pulses with $\hbar\omega=2.7$ eV at different intensities (indicated) as calculated with TDLDA (Pohl *et al.*, 2000). Vertical dotted lines show energies corresponding to $E_{IP}$ plus a certain number of photons. Bound states from which electrons originate are indicated in a few cases.

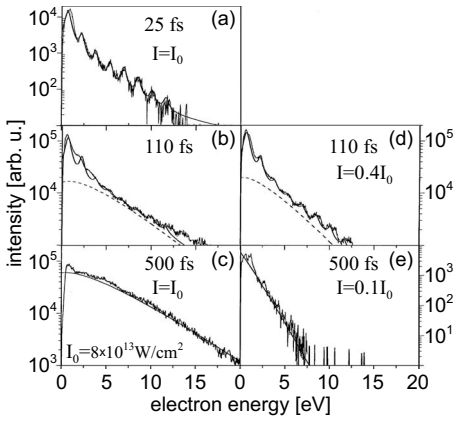


FIG. 21. Measured photoelectron spectra from $C_{60}$ exposed to laser pulses (790 nm) for various pulse widths and intensities (as indicated). Dashed lines show estimated thermal contributions. With both increasing pulse duration and increasing intensity the ATI feature declines, hinting at stronger contributions from electron-electron collisions and ionic motion. From Campbell *et al.*, 2000.

tered at higher laser intensity. The peak width increases dramatically from about 0.3 eV at $10^{11}$ W/cm$^2$, 0.6 eV at $10^{12}$ W/cm$^2$, to almost 2 eV at $10^{13}$ W/cm$^2$. This indicates a transition from the frequency-dominated domain to a dynamical regime where the field intensity becomes increasingly important.

#### 2. Above-threshold ionization and thermalization

At sufficiently high photon density, two and more photons can cooperate almost simultaneously in the excitation of a single electron. One of the consequences is direct electron emission, even far beyond the ionization threshold, although the photon energy stays below the IP. Figure 20 shows computed above-threshold ionization (ATI) spectra for $Na_9^+$, where the photon energy is 2.7 eV and thus much smaller than the $E_{IP}$ of 7.5 eV ($1p$ state) and the binding energy of the $1s$ state of 8.8 eV. The spectrum at the lowest intensity $I_0$ shows distinct peaks which can be associated with emission from these states and a well-defined number of photons $\nu$, as defined in Eq. (21). The intensity $I_0$ is already intermediate as a sufficient photon density is required to drive multiphoton excitation. On the other hand, the emission from a $\nu$-photon process evolves as $I^\nu$. This produces a steep increase with intensity such that there remains only a small intensity window before the signal becomes blurred. This is shown in Fig. 20 with the two higher intensities increased by factors of 1.5 and 3.0. Note that the spectrum is almost structureless for the highest intensity, which can be explained in the following way: the ongoing ionization increases the bonding and downshifts the single-particle levels. Moreover, the spectrum collects electrons from all stages such that the level motion first induces a broadening of the peaks ($I=1.5I_0$) and finally a complete blurring. It should be noted that the fully smoothed distribution shows an exponential decrease (after removing the $\sqrt{E_{kin}}$ phase-space element). In fact, as a result of the $I^\nu$ law, the exponential trend already appears for lower intensity when connecting individual peaks [for details see Pohl *et al.* (2004a)].

The example in Fig. 20 with fixed pulse length deals with the intensity effect on ATI from clusters. However, the pulse duration plays a cruical role as well because competing perturbations by electron-electron collisions and ionic motion come into play with increasing interaction time. This aspect is worked out in Fig. 21 with an experimental ATI result on $C_{60}$. The two middle panels corroborate the previous observation that increasing the laser intensity (step from right middle to left middle panel) smears out the multiphoton peak structure. Going through the figure from top to bottom, i.e., along increasing pulse duration, one also obtains a disappearance of the detailed pattern but this time due to an increase in the pulse width. Comparison with Fig. 2 helps with an interpretation. After a time span of the order of the electron-electron collision time ($\tau_{ee}$), the photon energy is distributed over the whole electronic system. The thermalized cloud evaporates one or more electrons at later times. The corresponding thermal emission spectrum is a smooth exponential (times phase-space factor), as indicated by the dashed curves in Fig. 21. The intermediate pulse width of 110 fs excites a transitional stage where direct and thermal emission compete. The longer time of 500 fs is safely in the thermal regime and even lowering of the intensity (lower right panel) does not revive any detailed ATI structures.

Since pronounced ATI signatures can be observed with complex systems such as $C_{60}$, it is a logical next step to consider the angular electron distributions as in the case of single-photon excitations discussed in Fig. 14. In a corresponding experiment on $C_{60}$ the energy- and angular-resolved spectra were measured for an excitation with 60 fs laser pulses (see Fig. 22). Integration of the signal over the emission angle reproduces the se-

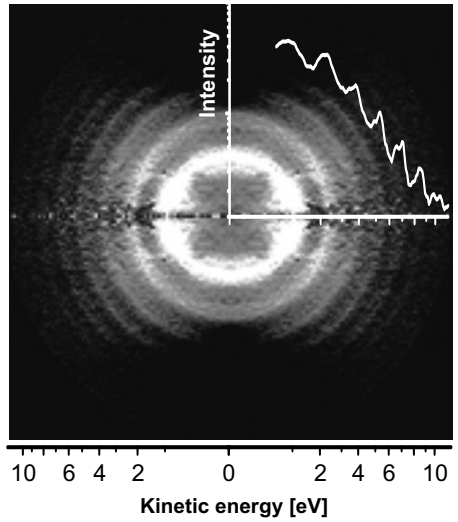


FIG. 22. Photoelectron angular distribution of $C_{60}$ for irradiation with 800 nm laser pulses of intensity of $I=10^{13}$ W/cm$^2$ and pulse width of 60 fs. The laser polarization is oriented along the horizontal axis. The rings correspond to above-threshold ionization, with increasing alignment for larger numbers $\nu$ of absorbed photons. The inset gives the angle-integrated intensity in qualitative agreement with the result in Fig. 21. From Skruszewicz *et al.*, 2009.

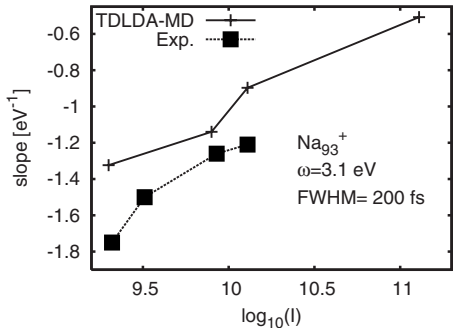


FIG. 23. Slope of the photoelectron spectrum from $Na_{93}^+$ irradiated by a 200 fs laser pulse of 3.1 eV. Results are drawn vs intensity [as $\log_{10}(I)$ with $I$ in units of W/cm$^2$]. Results from TDLDA-MD (Pohl *et al.*, 2004a) are compared with the experimental results of Schlipper *et al.*, 2001 using comparable experimental conditions.

quence of ATI peaks as seen for the short pulses in Fig. 21. The PAD exhibits, as additional information that the ATI peaks are well collimated in the direction of the laser polarization, an effect which increases with the number of photons involved. This indicates a direct emission process immediately induced by the pulse for high-order ATI. On the other hand, the more filled inner rings correspond to isotropic emission, which is most probably related to collisional thermalization. A solid understanding of the PAD structures, however, remains a challenging task for future theoretical investigations.

The above results indicate that electronic thermalization becomes increasingly important with increasing reaction time, i.e., if the laser pulse length exceeds the time required for collisional relaxation. Indeed, the underlying energy distributions in Figs. 21 and 22 show a roughly exponential behavior. For $Na_{93}^+$ perfect exponentials have been measured (Schlipper *et al.*, 2001). The slopes $s$ in $\exp(-sE_{\mathrm{kin}})$ of these distributions depend on the laser intensity (see the filled boxes in Fig. 23). Clearly the absolute values of the slopes decrease with rising intensity, which can be interpreted as an increased heating of the system. In fact, the situation might be even more complex: TDLDA calculations (without electron-electron collisions) on the same $Na_{93}^+$ also yield spectra with smooth exponentials while the signal stems from direct emission only. The trend and magnitude agree fairly well with the experimental data (cf. Fig. 23). This indicates that an interpretation as thermal emission is not compulsory from these data alone. A combined analysis including angular distributions and time-resolved measurements would be required in order to unambiguously distinguish between direct and thermal processes. These effects are considered in the models particularly suited for highly excited dynamics, i.e., VUU simulations (Sec. III.B.3), classical molecular dynamics (Sec. III.B.4), and rate equations (Sec. III.C). In the experiments, however, a clear identification of thermalization effects remains difficult. Here imaging techniques as discussed above provide a promising tool for further investigations.

## VI. CLUSTER DYNAMICS IN STRONG FIELDS

For the previously considered low and intermediate laser intensities, where nonlinearities such as plasmon broadening, the onset of saturation effects, and ATI have been discussed, the electronic configuration and ionic structure of the cluster remains similar to that of the initial state. This situation changes for laser-cluster interactions in the strong-field domain [see, for example, Figs. 1(c) and 1(d)]. In this regime the interaction leads to radical changes of the structure and properties of the clusters, such as, e.g., light-induced metallization of rare-gas systems through strong inner ionization, the creation of multiple core vacancies, or full cluster destruction via Coulomb explosion as a result of extreme charging. The cluster response is mostly (at least in the IR) field strength dominated as deduced from the Keldysh parameter or comparison with the BSI-threshold (cf. Sec. II.C). However, such an assignment based on atomic adiabaticity parameters may not be useful in all cases. The above phenomenological classification is therefore more appropriate to characterize "strong-field laser-cluster dynamics."

Several early experiments in the 1990s have sparked the rapid development of this topic. As an overview, we first concentrate on key phenomena and their possible relevance for technical applications. Subsequently we review aspects of the underlying microscopic mechanisms according to the current state of knowledge. Along this line, the discussion is divided into two parts. Section VI.A highlights early surprises and experimental key results, ranging from measurements of energy absorption

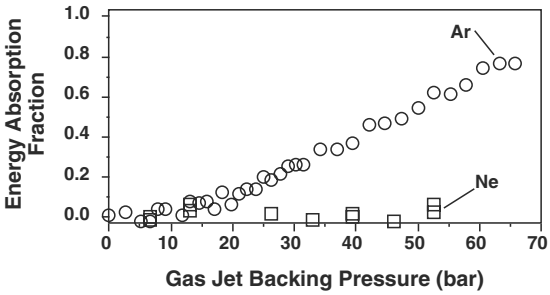


FIG. 24. Energy absorption of $Ar_N$ and Ne exposed to intense laser pulses ($7\times10^{16}$ W/cm$^2$, 2 ps, and 527 nm) as a function of backing pressure. The estimated $Ar_N$ cluster diameters are 80 Å at 40 bars and 100 Å at 55 bars. A major fraction of the laser pulse (up to 80%) is absorbed by the large Ar clusters while atomic Ne gas remains nearly transparent. Adapted from Ditmire *et al.*, 1997.

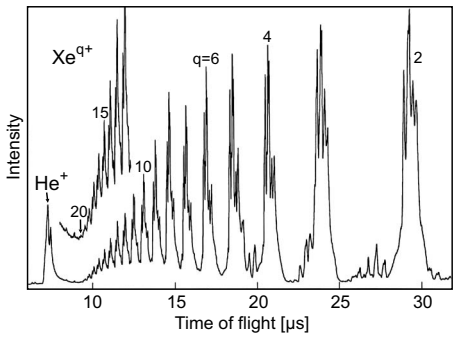


FIG. 25. Mass spectrum of highly charged atomic $Xe^{q+}$ ions resulting from excitation of $Xe_N$ with $1\times10^{15}$ W/cm$^2$, 350 fs, and 624 nm showing charge states up to $q^{max}=20$. Adapted from Snyder *et al.*, 1996.

and emission of energetic particles to short-wavelength radiation, and is restricted to a generic discussion of mechanisms and typical trends. Section VI.B reviews routes toward a more detailed microscopic understanding by closely relating theory and experiment and by pursuing more elaborate schemes such as time- or angular-resolved analyses. To describe the laser parameters, i.e., peak intensity $I_0$, pulses duration $\tau$ (FWHM), and wavelength λ, we sometimes use the compact notation ($I_0$, $\tau$, and λ).

### A. Early surprises and basic trends

#### 1. Laser energy absorption

A remarkable property of clusters in intense laser fields is very efficient energy absorption. At intensities of the order of $10^{15}$ W/cm$^2$ the average energy capture per atom can attain values of tens to hundreds of keV and by far exceeds that of atomic and molecular gas targets. Basically all of the violent processes discussed below have their starting point in this enhanced absorption in conjunction with the absence of dissipation into surrounding material.

The direct measurement of the absorption from the relative loss of laser pulse energy in the interaction region requires a high target density ($10^{13}$–$10^{15}$ clusters/cm$^3$). This situation can be realized close to the nozzle (~1 mm) of supersonic gas expansion sources and corresponds to an effective particle spacing of ≳100 nm. As a typical example for the different behaviors of clusters and gases, Fig. 24 shows the relative energy absorption $\mathcal{A}_L$ of high intensity laser pulses in a dense jet of $Ar_N$ compared to a Ne gas as a function of backing pressure. Since Ne does not condense at room temperature, the overall low absorption in Ne provides a reference for a gas of similar average atomic density. In contrast, Ar clusters become increasingly opaque with cluster size beyond the onset of cluster formation (at about 5 bars in this particular example). It should be noted that laser pulse depletion from light scattering was found to be insignificant (Ditmire *et al.*, 1997). Further, the increase of gas flux with pressure can be ruled out as a major origin for the higher pulse depletion (Zweiback *et al.*, 2002). Substantial absorption of up to $\mathcal{A}_L^{max}=0.8$ for the highest pressure in Fig. 24 is typical for dense atomic or molecular cluster beams and has also been observed with $(H_2)_N$, $(D_2)_N$, $Kr_N$, and $Xe_N$ (Ditmire *et al.*, 1997, 1999; Lin *et al.*, 2001; Miura *et al.*, 2001). In most cases, similar to Fig. 24, laser attenuation scales roughly linearly with stagnation pressure and then saturates [see also Jha *et al.* (2006)].

When analyzed as a function of pulse intensity, substantial absorption sets in at relatively sharp thresholds. Beyond the onset intensities, e.g., $I_{th}\approx3\times10^{13}$ W/cm$^2$ for $Ar_N$ and $I_{th}\approx4\times10^{12}$ W/cm$^2$ for $Xe_N$ at 527 nm, the pulse depletion increases rapidly and attains $\mathcal{A}_L\approx0.5\mathcal{A}_L^{max}$ at one order of magnitude higher intensity (Ditmire *et al.*, 1997). As the thresholds roughly follow the trend of the corresponding atomic BSI intensities, the behavior indicates an avalanche breakdown process triggered by atomic optical field ionization to establish efficient absorption. A clear signature of the dynamical nature of the energy capture, which turns out to be largely driven by resonant collective electron excitation, is the pulse length dependence of $\mathcal{A}_L$. This will be further discussed in Sec. VI.B.

#### 2. Highly charged atomic ions

Strong optical absorption leads to high ionization and usually complete disintegration of the clusters. Atomic ions with high ionization stages $q$ are finally detected [see Fig. 25 for an early ion spectrum on Xe clusters (Snyder *et al.*, 1996)]. After excitation with $10^{15}$ W/cm$^2$, 350 fs, and 624 nm pulses a broad charge state distribution emerges, extending up to $q^{max}=20$. Such charge states are much higher than those from atomic Xe under similar conditions. For example, pulse intensities of $10^{19}$ W/cm$^2$ are required to produce $Xe^{21+}$ (Dammasch *et al.*, 2001) from atomic gases—in reasonable agreement with the atomic BSI model. From 65 Å Xe clusters, ions with $q^{max}=40$ were reported by Ditmire *et al.* (1997a) after exposure to laser pulses with $2\times10^{16}$ W/cm$^2$,

150 fs, and 780 nm. Direct comparison of $Ar_N$ ($N \sim 100$) to Ar gas after irradiation with $2\times10^{14}$ W/cm$^2$, 30 ps, and 1064 nm pulses showed similar trends (Lezius *et al.*, 1997), i.e., substantially higher maximum charge states with clusters ($q^{max}=10$ with clusters versus $q^{max}=3$ with gas). The ion spectra from metal clusters ($Ag_N$, $Au_N$, $Pt_N$, and $Pb_N$) were explored with femtosecond pulses (800 nm) in several studies (Köller *et al.*, 1999; Schumacher *et al.*, 1999; Lebeault *et al.*, 2002; Radcliffe *et al.*, 2005), leading to values for $q^{max}$ up to 30 for intensities below $10^{16}$ W/cm$^2$. Further, highly charged ions have been reported for molecular clusters, i.e., atomic iodine with up to $q=15$ from $(CH_3I)_N$ (Ford *et al.*, 1999) with $2\times10^{15}$ W/cm$^2$, 130 fs, and 795 nm and up to $O^{6+}$ from $(H_2O)_N$ (Kumarappan *et al.*, 2003b) with $8\times10^{15}$ W/cm$^2$, 100 fs, and 806 nm pulses.

As a general remark it should be noted that ion distributions such as the one in Fig. 25 reflect an average over the focal intensity profile in the interaction zone where regions of higher intensity contribute with a smaller effective volume. Recently it has been demonstrated that contributions from the different intensities to such spectra can be deconvoluted (Döppner, Müller, *et al.*, 2007; Döppner *et al.*, 2009) by using intensity-selective scanning.

Dedicated studies on heterogeneous, doped, and embedded clusters have been performed to investigate the effect of the cluster composition. From Purnell *et al.* (1994), irradiation of hydrogen iodine cluster $(HI)_N$ with $1\times10^{15}$ W/cm$^2$, 350 fs, and 624 nm yields $I^{q+}$ with up to $q=17$. In the same work, $Ar_N$ and Ar atoms attached to $(HI)_N$ yield $Ar^{q+}$ up to $q=8$ for $Ar_N(HI)_M$, whereas no notable contribution from multicharged $Ar^{q+}$ ions is found for bare $Ar_N$. This supports that the low-IP atoms or molecules act as chromophores and initiate nanoplasma formation. Subsequently constituents with more strongly bound electrons can be ionized, e.g., via electron impact ionization. Other matrix effects occur in helium nanodroplets: Experiments on embedded clusters have shown evidence for electron transfer processes, where highly charged ions capture electrons from the surrounding helium (Döppner, Diederich, *et al.*, 2007). When considerably ionized, the helium shell can produce strong absorption enhancement due to resonant heating of the nanomatrix (Mikaberidze *et al.*, 2008).

Whereas most results have been obtained with optical lasers, first experiments are making use of a VUV free electron laser (Wabnitz *et al.*, 2002; Laarmann *et al.*, 2004). Power densities of up to $3\times10^{13}$ W/cm$^2$ at 98 nm (=12.65 eV) were used in these experiments on rare-gas clusters. Note that IBS heating is less effective at shorter wavelengths because of the low ponderomotive potential so that multiphoton ionization conditions are expected (cf. Sec. II.C). Moreover, resonant collective heating can be ruled out because of the high laser frequency. Still, ionization of clusters is quite effective, leading to ions with charge states up to $Xe^{8+}$ and $Ar^{6+}$. These findings underline that strong cluster excitation is still possible in the domain of large Keldysh parameters.

The origin of high-energy absorption required for the observed charging has been investigated with different theoretical approaches. Various concepts were proposed, ranging from models based on enhanced IBS heating due to strong electron-ion scattering (Santra and Greene, 2003), over efficient IBS heating resulting from a high-density nanoplasma produced by local field enhancement of inner ionization by neighboring ions (Siedschlag and Rost, 2004), to many-body heating effects (Bauer, 2004b; Jungreuthmayer *et al.*, 2005). Note that the calculations performed by Siedschlag and Rost (2004) for $Xe_{80}$ showed good agreement with the experimental ion spectra when including the experimental focus averaging. Within the approach of Santra and Greene (2003) there remain deviations from the experimental ion spectrum when taking the focus effect into account. For more details see the review of Saalmann *et al.* (2006). Further perspectives of VUV and extreme ultraviolet (XUV) excitations of clusters are discussed in Sec. VII.B. For now we return to excitations with optical lasers.

### 3. Ion energy distributions

Another early surprise was the large kinetic energy of atomic species emitted from clusters in intense laser pulses. Due to the strong heating of cluster electrons and high cluster charging on the femtosecond time scale, large amounts of thermal and Coulomb energies are available to be released within the explosion of the system. In experiments atomic ions from $Xe_N$ with kinetic energies beyond 1 MeV were observed (Ditmire *et al.*, 1997b). This has allowed for table-top experiments on cluster-based fusion (Ditmire *et al.*, 1999). Interestingly, for rare-gas clusters a rather sharp onset of high-energy ion emission is observed. For $Xe_N$ a threshold intensity somewhat above $10^{14}$ W/cm$^2$ was reported (Tisch *et al.*, 2003) with 230 fs pulses at 790 nm being roughly comparable with the BSI threshold intensity [see Eq. (6)].

The charge-state-averaged ion energy distributions turn out to be very broad [see Fig. 1(d) for $Pb_N$ and Fig. 26 for $(N_2)_N$] and show a smooth decrease with increasing energy, often followed by a cutoff frequently called "knee" feature. Typically the maximum energy, which may be quantified by the energy of the knee feature, increases with cluster size (see Fig. 26). However, in the case of $Xe_N$ (Mendham *et al.*, 2001) it was found that the maximum ion energy grows with cluster size until it levels out. For sufficiently short laser pulses the nanoplasma model predicts that the ion energy decreases beyond a certain size since the slower expansion of large clusters impedes resonant collective heating. The saturation can be explained by the relatively broad experimental cluster size distribution, i.e., the molecular beam still contains optimally sized particles producing the maximum ion energy.

Several additional effects contribute to the shape of the ion energy spectra, i.e., the spatial laser intensity profile and the degree of cluster ionization. Taking these effects into account, experimental data on $Xe_N$ (Ditmire

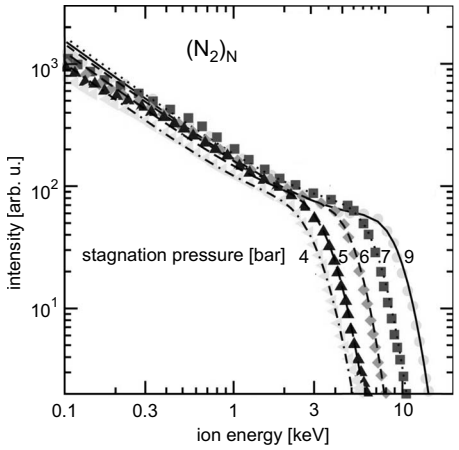


FIG. 26. Measured ion energy spectra from $(N_2)_N$ (curves) for excitation with $1\times10^{16}$ W/cm$^2$, 100 fs, and 800 nm pulses (Krishnamurthy *et al.*, 2004). The highest stagnation pressure corresponds to $\langle N\rangle=2300$. With increasing backing pressure, i.e., for larger clusters, the spectra are shifted to higher energies. Symbols represent fits using a Coulomb explosion model that incorporates averaging due to the laser beam profile and the cluster size distribution. From Islam *et al.*, 2006.

*et al.*, 1997b; Springate *et al.*, 2000b), $Ar_N$ (Kumarappan *et al.*, 2001), $(H_2)_N$ (Sakabe *et al.*, 2004), and $(N_2)_2$ (Krishnamurthy *et al.*, 2004) can be reasonably well fitted by considering Coulomb explosion (Islam *et al.*, 2006).

Neglecting thermal electron excitation and assuming a uniformly charged cluster, the final kinetic energy $\epsilon_I$ of an atomic ion is determined by its initial potential energy (Last *et al.*, 1997; Zweiback *et al.*, 2000; Nishihara *et al.*, 2001),

$$\epsilon_I(r)=\frac{4\pi}{3}\rho_I r^2 q^2\times 14.4\ \text{eV Å}, \tag{22}$$

where $r$ is the initial radial ion position, $q$ is the charge state of atomic ions, and $\rho_I$ is the number density of ions in the cluster. Hence, ions at the cluster surface acquire the highest recoil energies $\epsilon_I^{\max}$ and this maximum energy also increases with cluster size. The latter trend was experimentally confirmed on $Xe_N$ and $Ar_N$ by Ditmire *et al.* (1997a), Lezius *et al.* (1998), and Li, Wang, *et al.* (2003). Krishnamurthy *et al.* (2004) found a monotonous rise of the knee energy from about 1 to 8.5 keV with $(N_2)_N$ when increasing the size from $N=50$ to 2300 (cf. Fig. 26). With $Pb_N$, $\epsilon_I^{\max}$ rises from 70 to 180 keV when increasing the cluster size from $\langle N\rangle\approx100$ to $\approx500$ (Teuber *et al.*, 2001) [see Fig. 1(d)].

At constant cluster size, a recoil energy enhancement is observed when adding spurious amounts of appropriate dopants (Purnell *et al.*, 1994; Jha *et al.*, 2006). For instance, Ar clusters ($N\sim2000$) containing about 60 $H_2O$ molecules were considered by Jha *et al.* (2006). Under exposure to pulses with $1\times10^{16}$ W/cm$^2$, 100 fs, and 800 nm, the ion yield at 100 keV scales up by a factor of 3 and the maximum ion energy is larger when compared to the dopant-free case. This effect was traced back to a longer phase of strong cluster heating and ionization since dopants with lower ionization thresholds can initiate nanoplasma formation earlier in the laser pulse.

Clusters containing a mixture of low and high atomic number elements can be used to enhance the kinetic energy of the lighter ions. This is of particular interest for the acceleration of $D^+$ for fusion reactions. For pure $(D_2)_N$ ($N\lesssim10^5$) ion kinetic energies up to 30 keV were detected (Zweiback *et al.*, 2002) with $1\times10^{17}$ W/cm$^2$, 35 fs, and 820 nm pulses and energies up to 8.1 keV were found for bare $(H_2)_N$ ($N\sim10^5$) (Sakabe *et al.*, 2004, 2006) with $6\times10^{16}$ W/cm$^2$, 130 fs, and 850 nm pulses. The presence of a considerable fraction of highly charged heavy-element ions in the cluster produces a strongly repelling background for the light ions (Grillon *et al.*, 2002; Kumarappan *et al.*, 2003b; Madison *et al.*, 2004). For $(D_2O)_N$ an enhancement in $\epsilon_I(D^+)$ of 5.6 over the result from $(D_2)_N$ of the same radius is predicted in the limit of complete and instantaneous ionization due to higher ionization stages of oxygen (Last and Jortner, 2001). The increase in the kinetic energy of $D^+$ was verified in a study on $(D_2)_N$ and $(CD_4)_N$ (Madison *et al.*, 2004). From deuterated methane clusters excited with $1\times10^{17}$ W/cm$^2$, 35 fs, and 820 nm pulses, deuterium energies of up to 120 keV were found (Grillon *et al.*, 2002). Interestingly, only doubly charged carbon was detected, indicating substantial electron recapture. This is further supported by the fact that the maximum $C^+$ energy (180 keV) substantially exceeds the value for $D^+$.

Additional insight into the explosion dynamics and the initial ion position within the cluster can be gained by simultaneously measuring charge states and energies. In principle, each emitted ion state has its own characteristic spectrum. To access the charge-resolved spectrum, techniques such as MD-TOF or Thomson spectroscopy can be applied (see Sec. IV.C). As an example obtained with another method, i.e., retarding field analysis, Fig. 27 shows charge-resolved spectra measured at various recoil energies $\epsilon_I$ from irradiation of $Xe_{2500}$ with pulses of $2\times10^{16}$ W/cm$^2$, 150 fs, and 780 nm. With increasing $\epsilon_I$, the charge state distributions shift and broaden. At 100 keV, ions with $q=24$ are the most numerous and charge states up to $q\sim40$ are observed. In studies on $Ar_N$ ($N=1.8\times10^5$) and $Xe_N$ ($N=2\times10^6$) (Lezius *et al.*, 1998) a scaling like $\epsilon_I(q)=180\ \text{eV}\times q^2$ (Ar) and $\epsilon_I(q)=160\ \text{eV}\times q^2$ (Xe) was found for $q\leqslant6$, as expected from electrostatic consideration [see Eq. (22)]. The higher charge states ($q>10$) show a more linear dependence on $q$. Similar behavior was reported by Lebeault *et al.* (2002). This linear dependence has frequently been interpreted as a distinct fingerprint from hydrodynamic cluster expansion (driven by thermal electron energy), as predicted by the nanoplasma model (see Sec. III.C). Such an assignment of parts of the spectrum to a Coulomb explosion or a hydrodynamic expansion has nevertheless to be made with care. From a theoretical point of view (Ditmire *et al.*, 1996), the conclusion that hydrodynamic forces dominate the expansion is based on the assumption of a constant electron temperature in the expanding nanoplasma. This

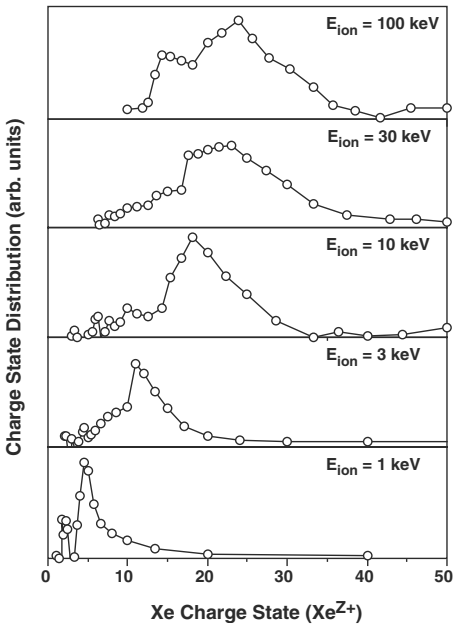


FIG. 27. Charge-resolved ion spectra from Coulomb explosion of $Xe_{2500}$ exposed to laser pulses with $2\times10^{16}$ W/cm$^2$, 150 fs, and 780 nm for different recoil energies $\epsilon_I$ (as indicated). With increasing ion kinetic energy the charge spectrum shifts to higher ionization stages. Adapted from Ditmire *et al.*, 1997a.

might be too crude to describe the dynamics correctly as the nanoplasma experiences efficient expansion cooling during cluster explosion (see Sec. VI.B.1). A more elaborate analysis of the expansion process predicts a scaling law for the maximum recoil energy as a function of atomic density, cluster radius, and initial temperature (Peano *et al.*, 2006, 2007). A one-to-one assignment of a quadratic dependence of $\epsilon_I(q)$ with a Coulomb explosion [see Eq. (22)] is correct only if the ionization process is quasi-instantaneous, i.e., much shorter than the time scale of the ionic motion [see also Teuber *et al.* (2001)]. For a dynamical cluster charging during the expansion, even pure Coulomb explosion can lead to a linear $\epsilon_I(q)$ scaling. Note that this interplay between charging time and ionic motion has also been discussed in the context of structure analysis of biomolecules through scattering of XFEL radiation (Neutze *et al.*, 2000).

#### 4. Soft x-ray and EUV emission

A decay channel of relevance for diagnostics and possible applications of laser-cluster interactions is the emission of energetic photons particularly in the soft x-ray domain. The x-ray spectra contain line emission that reflects recombination of electrons in weakly bound atomic levels with core-level vacancies, as first reported by Rhodes and co-workers (McPherson *et al.*, 1994). Note that the charge distribution during the pulse, as partly reflected by the x-ray spectra, may be different from the final ion spectra because of free-bound electron-ion recombinations and charge transfer processes.

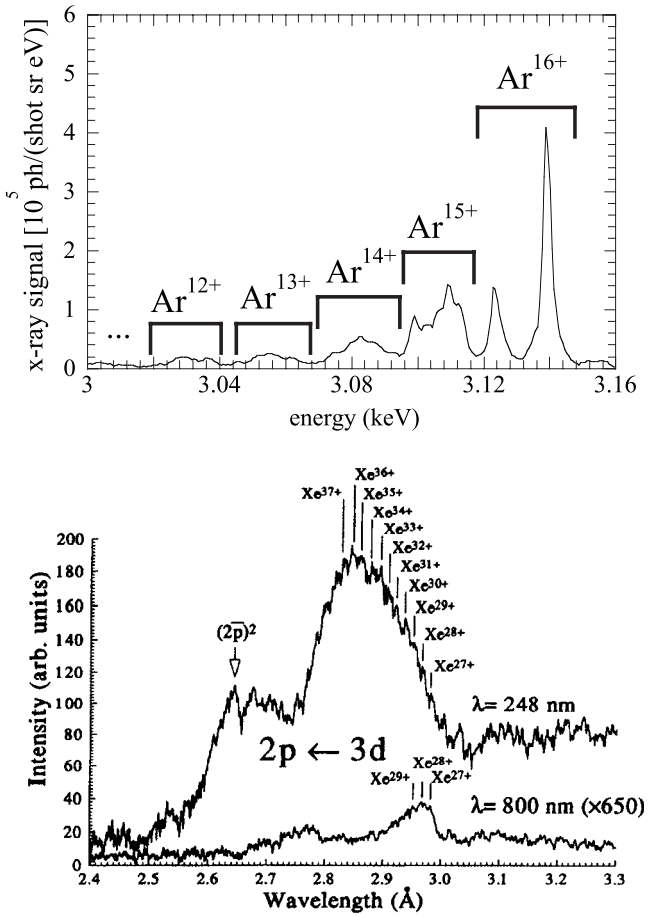


FIG. 28. Charge-state resolved x-ray emission from rare-gas clusters. Top: $K$-shell line emission from $Ar_N$ ($\langle N\rangle\sim4\times10^6$) exposed to $1.6\times10^{16}$ W/cm$^2$, 500 fs, and 800 nm laser pulses. From Dorchies *et al.*, 2005. Bottom: $L$-shell line emission from $Xe_N$ ($\langle N\rangle=12$) excited with $2\times10^{18}$ W/cm$^2$/$10^{19}$ W/cm$^2$, $\lesssim$1 ps, and 800 nm/248 nm. From Schroeder *et al.*, 1998.

The two examples in Fig. 28 show such line emission spectra which can be attributed to specific ion charge states. The top panel shows a result on $K$-shell emission from $Ar_N$ (Dorchies *et al.*, 2005) for a laser intensity of $1.6\times10^{16}$ W/cm$^2$. The example in the lower panel has been obtained at $10^{18}$–$10^{19}$ W/cm$^2$ on small $Xe_N$ and exhibits x rays down to 2.4 Å (5.2 keV) and contributions from highly charged $Xe^{q+}$ up to $q\sim40$ (Schroeder *et al.*, 1998, 2001). Note that the excitation at 248 nm compared to 800 nm results in lines from much higher charge states. So far, the most energetic x-ray emission from nanosized targets was observed on $Kr_N$ where strong $K\alpha,\beta$ radiation (12.66 keV/1.02 Å and 14.1 keV/0.88 Å) was found (Issac *et al.*, 2004) [see also Fig. 1(e)]. A comparative study on $Ar_N$, $Kr_N$, and $Xe_N$ with $5\times10^{16}$ W/cm$^2$ concentrated on $M$-shell line emission, e.g., $Kr^{9+}$ ($3d\leftarrow4d$), in the wavelength regime of about 10 nm (McPherson *et al.*, 1993). It has to be noted that this work provided the first evidence that ionization dynamics in clusters under strong field conditions significantly differs from the behavior of atomic targets. The enhanced x-ray emission disappears when the clusters

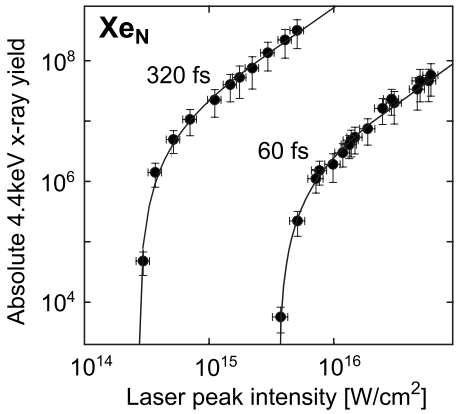


FIG. 29. Absolute x-ray yield from $Xe_N$ ($\langle N\rangle \sim 10^5$) vs laser intensity for two different pulse durations. Solid lines reflect the effective focal volumes with an intensity beyond $3.5\times10^{15}$ W/cm$^2$ for 60 fs and $2.5\times10^{14}$ W/cm$^2$ for 320 fs. From Lamour *et al.*, 2007.

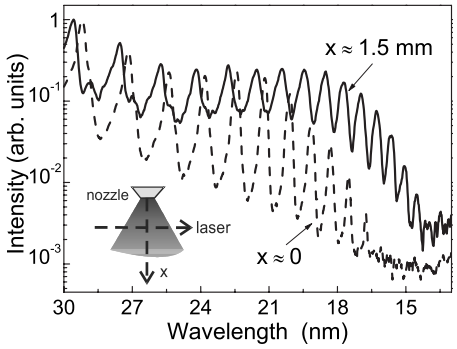


FIG. 30. High harmonic signals from Ar vs $Ar_N$: spectra resulting mainly from atomic argon (dashed curve) and $Ar_N$ ($\langle N\rangle \sim 10^5$, full curve) exposed to pulses with $2\times10^{14}$ W/cm$^2$, 25 fs, and 800 nm. The target conditions are selected by shifting the laser focus with respect to the nozzle (as indicated). From Vozzi *et al.*, 2005.

are destroyed by a weaker prepulse (Ditmire *et al.*, 1996; Skobelev *et al.*, 2002). The major contribution of the x-ray photons is emitted on the ns time scale (Ditmire *et al.*, 1995; Larsson and Sjögren, 1999; Kondo *et al.*, 2002), which is comparable to recombination lifetimes.

The yield of x-ray emission with laser intensity scales as $I^{3/2}$ once the saturation regime is attained. This behavior reflects the effective volume in the focus (Dobosz *et al.*, 1997; Rozet *et al.*, 2001) and is similar to atomic targets (Auguste *et al.*, 1992). For $Kr_N$ ($N\sim10^5$) a threshold for the onset of high-energy photon emission was observed slightly below $10^{16}$ W/cm$^2$ at 790 nm and 130 fs pulse width (Dobosz *et al.*, 1997). The onset intensities, however, show a strong dependence on pulse duration and cluster material. Pulse-length-dependent thresholds for $Ar_N$ and $Xe_N$ were observed by Lamour *et al.* (2005, 2007) and Prigent *et al.* (2008). An example from $Xe_N$ is shown in Fig. 29, where threshold intensities of $3.5\times10^{15}$ W/cm$^2$ are found with 60 fs pulses, whereas 320 fs pulses result in a substantially lower threshold of only $2.5\times10^{14}$ W/cm$^2$. The data hint at a transiently resonant heating (see Sec. VI.B.1). Note that the low threshold for the long pulse case is only slightly higher than the calculated BSI threshold intensity for atomic Xe ($9\times10^{13}$ W/cm$^2$).

A high number of emitted photons is crucial when aiming at technical applications such as EUV lithography (EUVL) [see, e.g., Banine and Moors (2004)]. Furthermore, for EUVL applications the emission must occur in a narrow spectral range to avoid aberrations. The spectral range around 13 nm is of importance since multilayer mirrors of Mo:Be and Mo:Si reach high reflectivities of nearly 70% (Stuik *et al.*, 1999). Conversion efficiencies of about $1\%/2\pi$ sr have been achieved at only 2% bandwidth, underlining that line emission from laser-driven Xe clusters, droplets, or jets [see, e.g., Hansson *et al.* (2004)] might be suitable for next generation microprocessor manufacturing (Attwood, 2007; Wu and Kumar, 2007). Within the soft x-ray regime, a recent study demonstrated the high potential of clusters in intense laser fields as debris-free radiation sources for nanostructure imaging (Fukuda *et al.*, 2008).

### 5. High harmonic generation

High harmonic generation (HHG) has been quite extensively studied in atomic and molecular gas jets (Krause *et al.*, 1992; Chang *et al.*, 1997; Spielmann *et al.*, 1997; Velotta *et al.*, 2001). The resulting spectra contain odd harmonics because of inversion symmetry and show an initial strong intensity decrease, a plateau region, and a rapid cutoff near $E_{IP}+3.17U_P$ (Brabec and Krausz, 2000). This cutoff is governed by the maximum return energy of electrons (Corkum, 1993) and reflects the importance of coherent stimulated recombination in atomic and molecular targets (Pukhov *et al.*, 2003). The physics of HHG in clusters and particles has been investigated only in a few experiments, although clusters may act as a unique nonlinear optical medium.

In an early study on HHG in clusters, a substantial harmonic signal of high order, actually 23rd harmonic ($HH^{23}$), was reported for $Ar_N$ (Donnelly *et al.*, 1996). For laser intensities of up to $1.5\times10^{14}$ W/cm$^2$, the $HH^{23}$ signal scales with $I^{17\pm1}$ and then changes its slope to $I^{4\pm1}$. In atomic gases for comparison, a power dependence of $I^{12}$ is found in the cutoff region (Wahlström *et al.*, 1993). A clear enhancement effect of the HHG yield in clusters was also reported on $Xe_N$ (Tisch *et al.*, 1997), where, for $HH^5$ (78 nm), an increase of almost one order of magnitude was found with respect to the atomic gas. A comparison of HHG spectra from atomic argon and $Ar_N$ taken under identical laser conditions is shown in Fig. 30. Close to the nozzle (i.e., $x=0$; see inset) the cluster formation is not completed and HHG mainly results from atoms. When clusters are present in the beam (at $x=1.5$ mm) the cutoff wavelength decreases considerably from 17 to 14 nm, thus increasing the highest HH order beyond the ponderomotive limit. A similar result was obtained by Pai *et al.* (2006). Common with all re-

sults is a significant HHG enhancement in clusters when compared to an atomic gas.

In fact, the special linear wave propagation properties of dense cluster media (cluster-cluster separations of the order of the diameter) could be advantageous for efficient HHG. Since a gas of inner-ionized clusters can build up strong depolarization fields, electromagnetic waves can propagate below the plasma cutoff in a particular optical mode—the so-called cluster mode (Tajima *et al.*, 1999). In a homogenous plasma, waves with frequencies below the plasma frequency become evanescent. Thus, a much higher electron density can be established in the cluster media without reflecting the fundamental wave. Moreover, in contrast to atomic gas plasmas, the refractive index of cluster media can be larger than 1. A certain mixture of atoms and clusters can be used to tune the refractive index in order to fulfill a major requirement for efficient HHG, i.e., phase matching. In principle phase matching can then be attained for any desired harmonic (Tisch, 2000), underlining the promising possibilities of clusters for tailored optical media.

Nonetheless, details on the microscopic mechanisms of HHG in clusters, e.g., concerning the interplay of stimulated recombination and bremsstrahlung, are yet to be explored. For a theoretical study on the contribution from bremsstrahlung see Popruzhenko *et al.* (2008).

### B. Analyzing the microscopic cluster response

The above examples highlight the violent and multifaceted nature of laser-cluster interactions in the strong-field regime. The aim of the following sections is to review selected aspects of the ultrafast microscopic dynamics for excitation with strong optical lasers in more detail. This concerns the dynamics of cluster heating, expansion, and ionization. The influence of the pulse structure on the laser energy absorption as well as on the emission of electrons, ions, and x-rays has been studied in experiments with stretched pulses or by dual-pulse excitation. In most cases the observed signatures support a large impact of resonant plasmon excitations as discussed in connection with theoretical concepts and results from numerical simulations. Further, we comment on the persisting difficulties in explaining the origin of highly charged ions, which requires understanding the strong-field ionization on the atomic scale in a highly excited many-body environment. Further, angular-resolved emission of electrons and ions will be addressed, which reveals unique acceleration effects in laser-excited clusters. Such studies can help identifying sensitive parameters for a control of specific decay channels and are important tests for theoretical models.

#### 1. The key role of collective excitations

*a. Evidence for resonant absorption*

An important concept for explaining the high-energy absorption of clusters in intense optical laser pulses involves resonant collective electron excitations. Since an inner ionized cluster is usually overcritical, a certain density lowering from cluster expansion is required to achieve frequency matching of the collective mode with the IR laser pulse (see Sec. II.C). Experimental evidence for such transient resonance was found by Zweiback *et al.* (1999) (see Fig. 31), where the laser energy absorption in a Xe cluster beam is measured as a function of pulse profile. The upper panel of Fig. 31 shows the result of a dual-pulse (pump-probe) experiment. In a simplified picture, the leading pulse excites the cluster moderately and initiates its expansion. At a certain time the system reaches resonant conditions leading to a strong peak in the absorption as clearly seen in Fig. 31. The optimal pulse delay increases with size, showing that larger clusters require more time to reach frequency matching. An alternative way to explore the expansion time is to use one pulse but varying its length, as shown in Fig. 31(b). Similarly, an optimal pulse duration is shown to induce maximum absorption which again increases with system size. A word of caution is advised for interpretation of such stretched pulse measurements as the intensity decreases with increasing pulse duration. For example, considering a certain threshold intensity for the nanoplasma buildup (e.g., the BSI intensity), the effective interaction volume strongly depends on the pulse duration

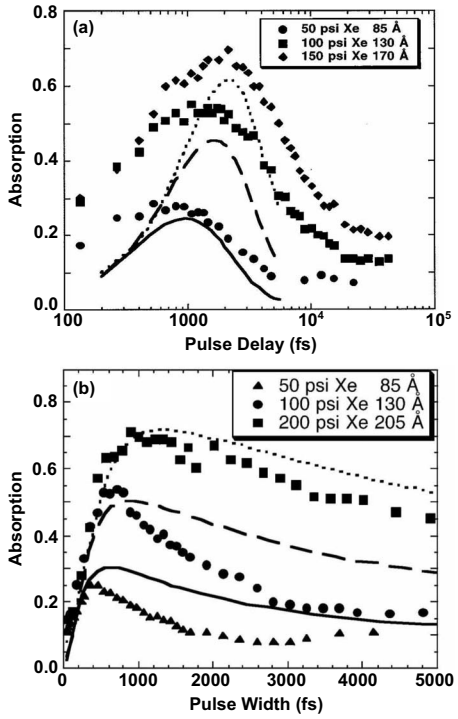


FIG. 31. Laser power absorption (symbols) by Xe clusters of different sizes (as indicated) for (a) dual-pulse excitation and (b) irradiation with stretched pulses at $\lambda=810$ nm. The dual-pulse results were obtained with 50 fs pulses of peak intensities $I_1=1.6\times10^{16}$ W/cm$^2$ and $I_2=1.6\times10^{17}$ W/cm$^2$. The single-pulse experiment was performed with constant pulse energy of 6.5 mJ, resulting in a peak intensity of $2.3\times10^{17}$ W/cm$^2$ at 50 fs pulse duration. The curves show results calculated with the hydrodynamic model from Ditmire. Adapted from Zweiback *et al.*, 1999.

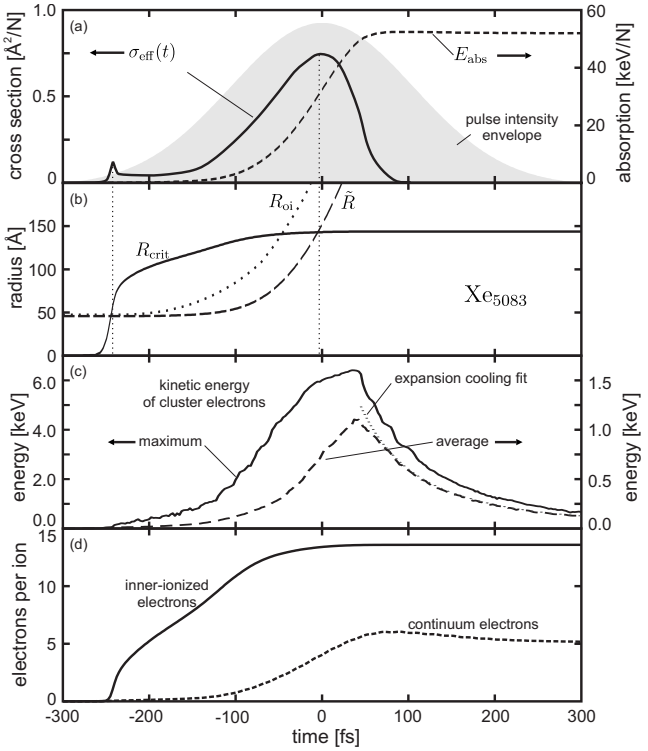


FIG. 32. Simulated dynamics of $Xe_{5083}$ exposed to a laser pulse with $10^{15}$ W/cm$^2$, 250 fs, and 800 nm using the MD code from Fennel, Ramunno, and Brabec, 2007. (a) Pulse intensity profile, cycle-averaged energy capture $E_{\rm abs}$, and associated absorption cross section $\sigma_{\rm eff}=\dot{E}_{\rm abs}/I$. (b) Mean cluster radius $\tilde{R}=\sqrt{5/3}R_{\rm rms}$, where $R_{\rm rms}$ is the root-mean-square radius, radial position of outermost ion $R_{oi}$, and critical radius $R_{\rm crit}$ for resonant coupling [Eq. (23)]. The vertical dotted lines mark the matching between $\tilde{R}$ and $R_{\rm crit}$, which coincides with the maxima in the absorption cross section. The difference between $\tilde{R}$ and $R_{oi}$ indicates inhomogeneous cluster expansion. (c) Average and maximum electron kinetic energy within the cluster radius $\tilde{R}$. The dotted line shows a fit for adiabatic expansion cooling (see text). (d) Number of inner-ionized and continuum electrons (cycle averaged); the difference of these values reflects the number of quasifree electrons (cf. Fig. 4).

as well. Thus, a long pulse with low peak intensity will probe a smaller number of targets. This problem does not occur with a dual-pulse setup as in Fig. 31(a). Nevertheless, both excitation schemes show a pronounced resonance feature in qualitative accordance with calculations based on the hydrodynamic model from Ditmire discussed in Sec. III.C (see curves in Fig. 31).

Modeling the cluster response by a single collective mode is, however, strongly oversimplified. A more comprehensive picture can be drawn from microscopic simulations, such as MD (see Sec. III.B.4). Figure 32 shows results from a MD simulation of $Xe_{5083}$ exposed to a 250 fs pulse of $10^{15}$ W/cm$^2$ [for details of the method see Fennel, Ramunno, and Brabec (2007)].

The upper panel of Fig. 32 shows the effective absorption cross section (solid line), as derived from the total energy capture (dashed line), together with the laser intensity envelope (centered at time zero). The broad absorption peak between −80 and 50 fs corresponds to resonant collective heating that is established due to the expansion-induced shift of the plasmon energy. The dominant energy capture proceeds near the crossing of the mean cluster radius $\tilde{R}$ with the critical radius for resonant collective coupling $R_{\rm crit}$ at $t\approx 0$ fs [see panel (b)]. The value of $R_{\rm crit}$ is estimated from the Mie formula [Eq. (1)] by

$$R_{\rm crit}=\left(\frac{e^2}{16\pi^3\epsilon_0 m_e c^2}\langle q\rangle N\lambda^2\right)^{1/3}, \tag{23}$$

with $\langle q\rangle$ the average atomic ionization state of the ions. For example, at $\lambda=800$ nm, a xenon cluster ($r_s=2.5$ Å) must expand by a factor of 1.4 for $\langle q\rangle=1$ and of 3.0 for $\langle q\rangle=10$ to become resonant. The evolution of cluster inner ionization [see Fig. 32(d)] leads to a time-dependent $R_{\rm crit}$. In particular, rapid inner ionization triggered by optical field ionization and further enhanced by electron impact induces a sudden rise of $R_{\rm crit}$ in the leading edge of the pulse [see Fig. 32(b)]. The initial charging is accompanied by a short period of resonant coupling when $R_{\rm crit}$ crosses the actual system radius before the cluster becomes overcritical. This ionization-driven resonance is reflected in a small feature in the cross section at $t\approx -240$ fs and was also observed in MD calculations by Saalmann and Rost (2003). When using IR pulses, such early resonance would not occur in metal clusters, as they are overcritical already in the initial state. Returning to Fig. 32, the major contribution to the energy capture $E_{\rm abs}$ proceeds within the expansion-driven resonance around $t\approx 0$ fs. In total, the ultimately absorbed energy exceeds 50 keV per atom similar to the findings of Saalmann (2006). Note that the maximum cross section of 0.75 Å$^2$/atom is comparable to values typical for collective resonances in the linear regime [cf. Fig. 1(b)]. The cross section in Fig. 32(a) reduces quickly after the resonance, reflecting the suppressed coupling efficiency at *undercritical* density. Collective effects become unimportant and IBS heating of residual electrons is weak due to rare electron-ion collisions.

Several effects contribute to the considerably large width of the resonance. To some extent, the broadening can be linked to inhomogeneous cluster expansion [see, e.g., Milchberg *et al.* (2001)], with time-delayed resonant absorption in radial shells of critical density. A comparison of the radial position of the outermost ion $R_{\rm oi}$ with $\tilde{R}$ in Fig. 32(b) shows that outer ions indeed expand more quickly [see also Ishikawa and Blenski (2000)]. This expansion is due to a less effective screening of ions near the cluster surface (Peano *et al.*, 2006). Besides the influence of the ionic density profile, the driving of electrons beyond the cluster surface introduces an additional broadening due to nonlinear damping (Megi *et al.*, 2003; Jungreuthmayer *et al.*, 2004). For sufficiently high laser intensity, the occurrence of a nonlinear resonance has also been discussed (Mulser *et al.*, 2005; Kundu and Bauer, 2006).

Returning to the example in Fig. 32, the average kinetic energy of cluster electrons of up to 1 keV [dashed curve in Fig. 32(c)] shows that there is strong thermal excitation of the nanoplasma near the resonance. The maximum electron kinetic energy within the cluster of up to 6 keV (solid line) provides a reasonable measure for the depth of the transient space-charge potential produced from outer ionization and thermal excitation [see also Saalmann and Rost (2005)]. With electron impact excitation, such energetic electrons can directly create deep inner-shell vacancies required for hard x-ray emission. After the resonant heating the expansion of the ionic background leads to an efficient electron cooling. This process can be well described by adiabatic cooling of an ideal gas in an expanding spherical vessel: $\langle \epsilon_{\rm kin}(t)\rangle = aR^{-2}(t)+b$ [see dotted curve in Fig. 32(c)]. The offset parameter $b$ accounts for the kinetic energy of electrons that become localized in ionic cells during expansion. As displayed in the lowermost panel, a substantial fraction of the inner-ionized electrons cannot be accelerated to continuum energies and remains bound in the cluster potential. Further evolution of these electrons is of central importance for predicting the final ion charge spectrum and will be reconsidered in Sec. VI.B.2.

The above MD analysis illustrates that the dynamics is dominated by collective energy absorption near the critical density. The cluster expansion to $R_{\rm crit}$ therefore sets a crucial time scale for strong-field laser-cluster interactions in the IR regime. Resonance effects can be disregarded only at very high intensities, where the laser field exceeds the restoring force from the ion background potential (Krainov and Smirnov, 2002; Heidenreich *et al.*, 2007).

*b. Signatures in emission spectra*

Having identified the dominant role of collective excitations in the absorption, we now concentrate on corresponding signatures in the emission of x rays, highly charged ions, and electrons.

Time-resolved measurements of the x-ray emission have been performed primarily on rare-gas clusters using stretched pulses (Zweiback *et al.*, 1999; Parra *et al.*, 2000; Chen, Park, Hong, Choi, *et al.*, 2002; Issac *et al.*, 2004; Lamour *et al.*, 2005; Prigent *et al.*, 2008). An example for Xe clusters is given in Fig. 33 showing the x-ray yield from $3d \rightarrow 2p$ transitions of $Xe^{q>24+}$ (Lamour *et al.*, 2005). The signal can be interpreted as a measure of energetic cluster electrons as the production of $Xe^{24+}$ plus the $2p$ vacancy by electron impact requires considerable energies of 7.3 and ~4.5 keV. The energy for the creation of the vacancy should be transferred within one single collision event. Figure 33 shows a steep increase in the x-ray yield for pulse durations up to 250 fs, indicating a growing number of multi-keV cluster electrons. Note that this is compatible with the generation of keV electrons at the instant of resonant heating in Fig. 32(c). The optimal duration thus indicates efficient collective heating [see also Zweiback *et al.* (1999) and Parra *et al.* (2000) and similar experiments on EUV emission (Chen, Park, Hong, Choi, *et al.*, 2002)]. An alternative electron heating mechanism, namely, multiple large-angle electron-ion backscattering in phase with the laser field, was proposed by Deiss *et al.* (2006) in order to explain the x-ray production from pulses that are too short for reaching resonant conditions. Whereas basic aspects of short-wavelength emission from clusters can be rationalized, there are still several pending issues. For example, the role of ionization and excitation over intermediate states or the impact of multielectron collisions on the production of core vacancies have not been resolved. Therefore, the physics behind x-ray emission from clusters remains an interesting subject for further studies.

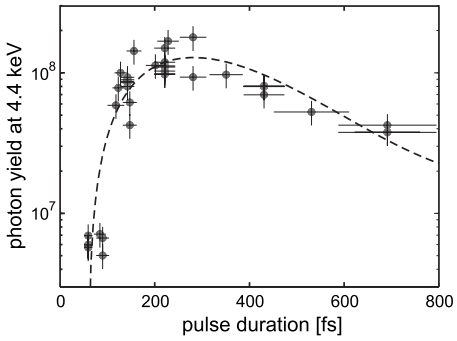


FIG. 33. X-ray yield at 4.4 keV from $Xe_N$ with $\langle N\rangle \approx 4\times10^4$ irradiated with stretched laser pulses of fixed energy (35 mJ) at 800 nm wavelength. The shortest pulse ($\tau$=50 fs) corresponds to a peak intensity of $3\times10^{16}$ W/cm$^2$. The dotted line is guide for the eyes. From Lamour *et al.*, 2005.

Measurements of ion kinetic energy spectra as a function of pulse duration substantiate the strong impact of the pulse structure. Figure 34 shows a result of a constant peak intensity experiment on $Xe_N$ performed by Fukuda *et al.* (2003). The mean ion energy grows with pulse duration reaching a maximum at about 500 fs, in accordance with the picture of a delayed resonance. Similar behavior has been reported from a constant fluence measurement (Kumarappan *et al.*, 2002). A clear effect of the temporal phase of the pulse has also been

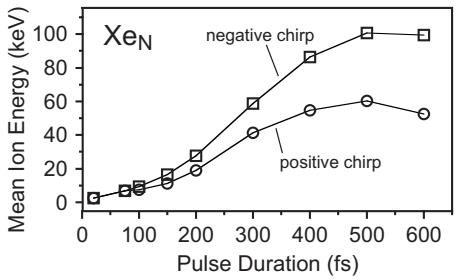


FIG. 34. Mean recoil energy of atomic ions emitted from $Xe_N$ ($\langle N\rangle \approx 5.5\times10^4$) for excitation with stretched pulses at 800 nm (spectral width of ~60 nm) and constant peak intensity of $2\times10^{17}$ W/cm$^2$. The results have been obtained with positively and negatively chirped pulses (as indicated). Note that a negative chirp corresponds to a decreasing laser frequency within the pulse. For 500 fs pulses the chirp rate is about 0.13 nm/fs. Adapted from Fukuda *et al.*, 2003.

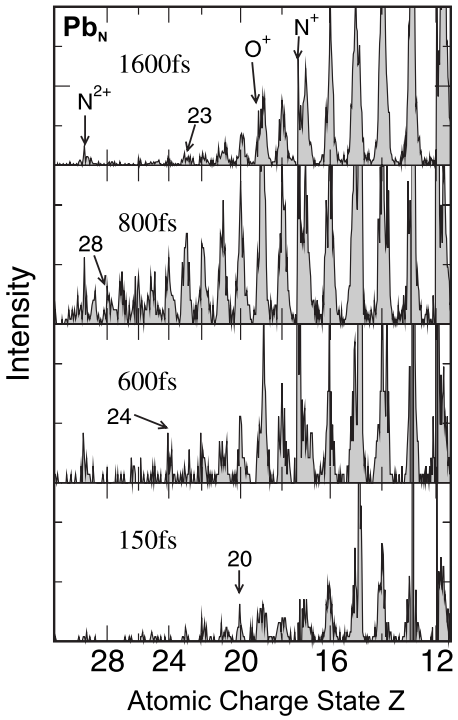


FIG. 35. Charge state distribution of $Pb^{q+}$ ions emitted from lead clusters after exposure to laser pulses of variable duration and constant energy (19 mJ). The laser peak intensity is $2.6 \times 10^{16}$ W/cm$^2$ for the shortest pulse (150 fs) and $10^{15}$ W/cm$^2$ for the optimal duration (800 fs), where the latter yields the highest charge states of up to 28. From Döppner *et al.*, 2000.

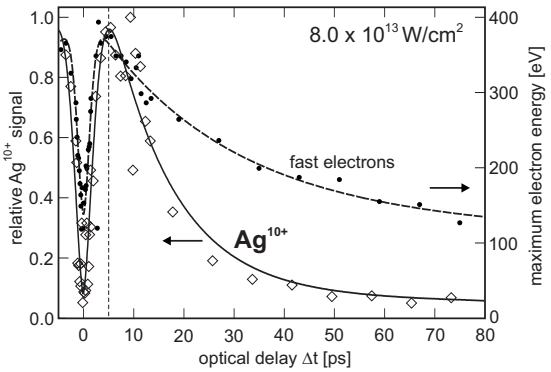


FIG. 36. Comparison of the $Ag^{10+}$ yield (diamonds, left axis) with the maximum kinetic energy of the emitted electrons (dots, right axis) following laser excitation of Ag clusters ($\langle N \rangle \approx 2 \times 10^4$) with dual 100 fs laser pulses at intensity of $8 \times 10^{13}$ W/cm$^2$ and 800 nm wavelength. The curves are guides for the eyes. Adapted from Döppner *et al.*, 2006.

observed (Fukuda *et al.*, 2003). Significant differences in the ion energies were found for positively and negatively chirped pulses. For negative chirp, i.e., a decreasing laser frequency with time, a 60% enhancement of the mean ion energy was observed (see Fig. 34). This effect can be explained qualitatively by the joint gradual frequency redshift of both laser pulse and resonance, which, in turn, extends the time span for resonant collective absorption. Applying the nanoplasma model to these particular experimental parameters, 500 fs pulses with negative chirp lead to 1.2 times higher total energy capture than the corresponding result with positive chirp.

Experiments have also shown strong enhancement of cluster ionization for optimal pulse durations (Köller *et al.*, 1999; Schumacher *et al.*, 1999; Döppner *et al.*, 2000; Lebeault *et al.*, 2002; Fukuda *et al.*, 2003; Döppner, Müller, *et al.*, 2007). Figure 35 shows spectra of high-$q$ ions as a function of pulse width for an experiment with constant laser fluence (Döppner *et al.*, 2000). The shortest and most intense pulses (150 fs) yield atomic ions up to $q=20$. With increasing pulse duration, the maximum charge state as well as the overall signal intensity grow toward a maximum for an optimal pulse width of 800 fs, where atomic ions up to $q=28$ can be identified. When further increasing the pulse duration, both the maximum charge state and the overall signal degrade.

The efficient charging for a certain pulse duration was in most cases attributed to resonant heating. Another mechanism, i.e., enhanced ionization (ENIO), has been proposed by Siedschlag and Rost (2003). This mechanism relies on the concept of charge-resonance enhanced ionization (CREI) known from diatomic molecules (see Sec. II.C), which was also considered for multiple ionization of clusters in Last and Jortner (1998). Within ENIO, the increased ionization probability occurs for an optimal interatomic distance, where the tunneling barrier between neighboring ions and the outer cluster Coulomb barrier of the system are reduced simultaneously. The optimal pulse duration is thus related to the instant at which the expanding cluster reaches the optimal interatomic distance. However, because of the large outer Coulomb barriers in highly charged clusters, ENIO is considered to be primarily relevant for small compounds ($N \lesssim 10$). Enhanced ionization due to resonant heating (plasmon-enhanced ionization), on the other hand, applies to clusters of any size and even to nm particles (Suraud and Reinhard, 2000; Reinhard and Suraud, 2001; Saalmann and Rost, 2003; Döppner *et al.*, 2005; Saalmann, 2006).

The emission spectra discussed correspond to experiments with one single pulse of variable duration. Results from a dual-pulse experiment on Ag clusters are given in Fig. 36 showing the yield of $Ag^{10+}$ and the maximum energy of the emitted electrons as a function of pulse separation. The ion signal shows a pronounced maximum for delays of about 5 ps with an enhancement of more than one order of magnitude. This indicates that cluster activation and enhanced ionization can be disentangled, as is also supported by numerical simulations (Martchenko *et al.*, 2005; Siedschlag and Rost, 2005; Döppner *et al.*, 2006; Bornath *et al.*, 2007a, 2007b). Clear indications that a sequence of two pulses may even represent the optimal pulse profile for high-$q$ ion production have been found by Zamith *et al.* (2004) for $Xe_N$ and by Truong *et al.* (2010) for $Ag_N$. In both studies genetic feedback algorithms have been used to optimize the temporal pulse structure in order to maximize ion charge states and converged toward a pulse profile containing two subpulses. Dual-pulse excitation even offers

a route for targeted control of the cluster dynamics. It has been demonstrated on small silver clusters in helium droplets that the optimal delay can be controlled by the intensity of the leading pulse. As corroborated by semiclassical Vlasov calculations, a higher intensity of the leading pulse enhances the cluster expansion speed due to stronger heating and ionization and thus reduces the time for which resonant coupling conditions are established (Döppner *et al.*, 2005).

Returning to Fig. 36, also the maximum electron energy is analyzed as a function of pulse separation. The coincidence of high ionization yield and maximal electron energy underlines the leading role of collective excitations in both decay channels. A similar correlation between fast electrons and VUV radiation was reported by Springate *et al.* (2003). A common feature is the occurrence of high electron energies. A maximum value of 375 eV$\approx 60U_p$ was observed with $Ag_N$ at moderate intensity (see Fig. 36). For $Xe_N$, electon energies in the keV range have been reported (Shao *et al.*, 1996; Kumarappan *et al.*, 2002; Springate *et al.*, 2003). Further details on the electron emission, i.e., angular- and time-resolved signatures and underlying acceleration mechanisms, are discussed in Sec. VI.B.3.

#### 2. Difficulties of explaining high charge states

Although most of the above trends such as higher ionization and energetic particle emission for resonant cluster excitation can qualitatively be explained, the quantitative understanding of the emission spectra remains a challenge. A still largely debated topic is the origin of the very high atomic ionization stages from clusters (Fennel, Ramunno, and Brabec, 2007; Heidenreich *et al.*, 2007). In order to calculate realistic ion spectra, inner ionization in the presence of local fields, outer ionization dynamics, as well as recombination effects have to be taken into account consistently. Difficulties arise from at least two facts. First, since inner ionization cannot be treated fully quantum mechanically for practical reasons, simpler approximations such as ADK rates and atomic impact ionization cross sections have to be used and must be corrected correspondingly. Second, recombination processes, even if treated only classically or with effective rates, proceed at much longer time scales than the interaction with the pulse and are thus numerically extremely time consuming. However, a few routes toward a more realistic description of high charge states by incorporating these effects have already been explored.

To cope with the first problem, inner ionization has to be corrected for medium contributions such as screening or polarization effects in the cluster. This is more or less straightforward for tunnel ionization as the effective local field resulting from the momentary distribution of charges and the laser is accessible numerically, e.g., from MD simulations. Applying an appropriate temporal or spatial filtering, the effective field can be used for the determination of tunneling ionization probabilities from the ADK rates (Ammosov *et al.*, 1986). More involved is the treatment of electron-impact ionization which is often described by the empirical cross sections of Lotz (1967). Their evalation, however, requires knowledge of atomic ionization thresholds which are modified by many-particle effects in the cluster such as screening and fields from neighboring ions. One way to the determine these shifts is the use of statistical approaches such as Debye screening or ion sphere models (Gets and Krainov, 2006; Bornath *et al.*, 2007a). These, however, assume local thermal equilibrium and neglect the details of ionic correlation. A more direct approach relies on the evaluation of the local field and the resulting shifts directly from a particle-based simulation [see Fennel, Ramunno, and Brabec (2007)]. Irrespective of the particular method, threshold lowering induces substantial enhancement of impact ionization when compared to the bare atomic cross sections. An example will be discussed below.

The second problem concerns the handling of electron-ion recombination. Usually it is assumed that only continuum electrons produced during the laser pulse contribute to the final ionization and cluster-bound electrons (quasifree after the laser pulse) fully recombine. With this assumption, however, the high experimental charge states at moderate laser intensities cannot be explained. Under experimental conditions this *full recombination* of quasifree electrons is questionable as, in particular, weakly bound electrons may not relax to lower ionic levels but can be reionized by space-charge fields in the interaction zone or by ion extraction fields required for the time-of-flight analysis (Fennel, Ramunno, and Brabec, 2007).

In latter work it was found that the combined action of both enhancement of electron impact ionization through threshold lowering and background-field induced frustrated recombination increases the maximum ion charge states by up to a factor of 2 (see Fig. 37). While enhanced charging of small clusters is dominated by threshold lowering effects, the consideration of the recombination dynamics becomes increasingly important with large clusters. Further contributions such as excitation autoionization or ionization via intermediate states, the importance of which is known for atomic electron-impact ionization (Griffin *et al.*, 1984; Loch *et al.*, 2008), have not been studied in detail.

#### 3. Asymmetric ion and electron emission

An interesting direction for possible technical applications of clusters is the pulsed generation of energetic ions and electrons. The quest for a detailed understanding of the acceleration mechanisms is therefore not only driven by fundamental interests. The presence of asymmetries in angular-resolved ion spectra reveals that the cluster disintegration notably deviates from an isotropic explosion process. Further, for excitation with appropriate pulses, the electron spectra show strong signatures from field-driven acceleration with high directionality. Corresponding signatures from experimental and theo-

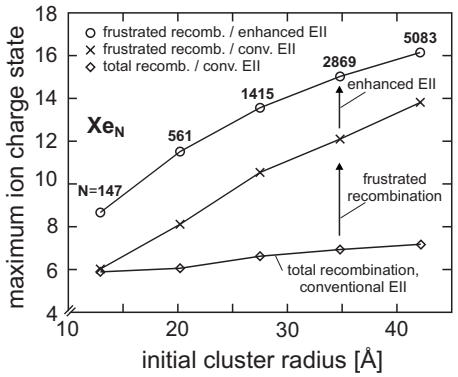


FIG. 37. Calculated maximum charge state of atomic ions from $Xe_N$ ($N$=147–5083 as indicated) exposed to 250 fs laser pulses with peak intensity $4\times10^{14}$ W/cm$^2$. The results correspond to different treatments of electron-impact ionization (EII) and electron-ion recombination. Conventional and enhanced EII correspond to atomic and local-field corrected ionization thresholds, respectively. Total recombination assumes that cluster-bound electrons recombine with the closest ion after the laser pulse, while the long-term dynamics of quasifree electrons in the presence of a weak static background field of 3 kV/m is taken into account for frustrated recombination. Adapted from Fennel, Ramunno, and Brabec, 2007.

retical studies as well as the main concepts for their explanation are reviewed below.

*a. Angular-resolved ion emission*

Ion energy spectra exhibit a clear asymmetry, where higher kinetic energies appear for the emission along the laser polarization axis. This was first reported for $Xe_N$ (Springate *et al.*, 2000a; Kumarappan *et al.*, 2002) and $Ar_N$ (Kumarappan *et al.*, 2001; Hirokane *et al.*, 2004). Figure 38 shows an example for the directional asymmetry for $Ar_N$ ($N\sim40\,000$) after excitation with $8\times10^{15}$ W/cm$^2$, 100 ps, and 806 nm pulses, where a

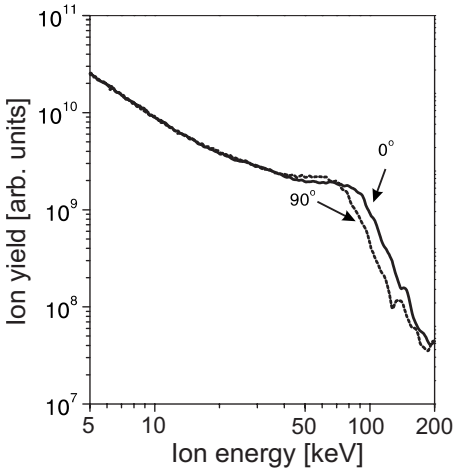


FIG. 38. Angular dependence of the ion recoil energy spectra of Ar clusters ($N=4\times10^4$) exposed to pulses with $8\times10^{15}$ W/cm$^2$, 100 ps, and 806 nm. At 0°, the polarization of the laser is parallel to the time-of-flight axis. Adapted from Kumarappan *et al.*, 2001.

polarization-induced shift of the knee in the energy distribution of about 20% is observed. Similar shifts between 15% and 40%, depending on pulse duration, were found with $Xe_N$ (Springate *et al.*, 2000b; Li *et al.*, 2005) and with molecular $(N_2)_N$ clusters (Krishnamurthy *et al.*, 2004; Mathur and Krishnamurthy, 2006).

At least three fundamentally different contributions to this asymmetry have been described. Ishikawa and Blenski (2000) proposed a mechanism where the additional acceleration is a direct result of the laser field. Since the net effect of the laser averages out for ions with constant $q$, rapid charge state oscillations of surface atoms were proposed, such that higher effective charge states appear during laser half cycles with outward electric field component, which accumulates maximum repulsion along the laser polarization axis. However, this mechanism is unlikely to fully explain the experimental asymmetry since the rates for electron-ion recombination are very low at typically high electron temperatures (Bethe and Salpeter, 1977).

The second mechanism was an asymmetric Coulomb explosion due to angular-dependent charging of ions and was originally discussed for $C_{60}$ (Kou *et al.*, 2000). Near the cluster poles, i.e., the regions with surface normal parallel to the polarization axis, higher peak electric fields from the laser and the cluster field (polarization and/or space charge) enhance inner ionization. Thus, ions located in this region experience stronger Coulomb repulsion. This view of enhanced ion acceleration along the polarization axis is supported by numerical simulations (Fennel *et al.*, 2004; Jungreuthmayer *et al.*, 2004) and the observation of asymmetric ion charging (Hirokane *et al.*, 2004).

Finally, forces directly from the cluster polarization field enhance asymmetric ion acceleration (Kumarappan *et al.*, 2002; Fennel *et al.*, 2004; Breizman *et al.*, 2005). In terms of a simple rigid sphere model, cluster ions and electrons can be described by two homogenously charged spheres of opposite charge density and equal radius. The laser-driven oscillation of the electron cloud results in a nonvanishing asymmetric contribution to the radial component of the electric field at the cluster surface, whereby enhanced repulsion follows for surface ions near the cluster poles (Breizman *et al.*, 2005). Even for an isotropic ion charge state distribution, this mechanism supports enhanced repulsion for surface ions near the cluster poles. This repulsion is particularly strong for large-amplitude oscillations of the electron cloud at resonance (see Sec. VI.B.1). Thus, this model can also explain the pulse-length-dependent asymmetry observed by Kumarappan *et al.* (2002).

*b. Angular-resolved electron emission*

Compared with ions, the degree of asymmetry is much more pronounced with electrons. The emission is aligned along the laser polarization axis (Shao *et al.*, 1996; Kumarappan *et al.*, 2002; Springate *et al.*, 2003). This preferential ejection is a direct marker for laser-assisted and nonthermal emission and turns out to also

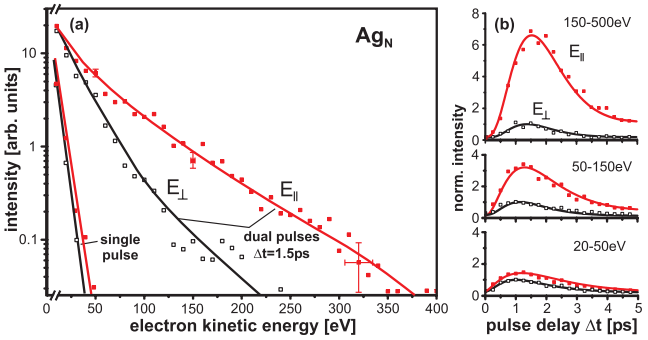


FIG. 39. (Color) Photoemission spectra from silver clusters ($N \approx 10^3$) exposed to 100 fs laser pulses with peak intensity of $8 \times 10^{13}$ W/cm$^2$ at 800 nm wavelength. (a) Energy-resolved emission parallel ($E_\parallel$) and perpendicular ($E_\perp$) to the laser polarization axis for excitation with a single pulse and dual pulses with optimal temporal delay of $\Delta t = 1.5$ ps. (b) Integrated signals for three electron energy intervals (as indicated) and normalized to the maximum obtained for ($E_\perp$) as a function of pulse delay.

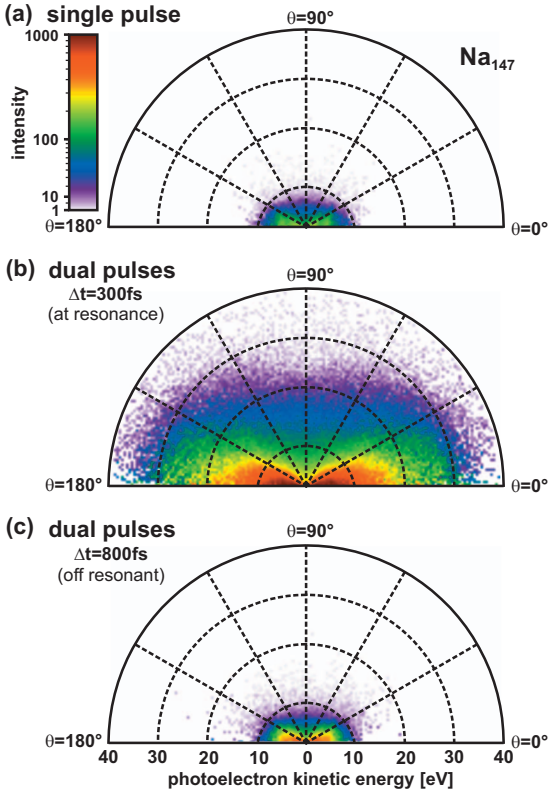


FIG. 40. (Color) Angular-resolved electron emission spectra from $Na_{147}$ exposed to 25 fs laser pulses (800 nm) with peak intensity of $8 \times 10^{12}$ W/cm$^2$ as calculated from semiclassical VUU-MD simulations. The data correspond to (a) single-pulse and dual-pulse excitations at (b) optimal and (c) a longer nonresonant delay. The emission angle $\theta$ is given with respect to the laser polarization axis. The plot is based on the data from Fennel, Döppner, *et al.*, 2007 but shown with a convenient intensity scaling.

be strongly dependent on the pulse duration. On $Xe_N$ Kumarappan *et al.* (2003a) found a yield ratio $Y_\parallel / Y_\perp \approx 3$ for optimal pulse durations, while almost isotropic emission and less energetic electrons are observed for the shortest and most intense pulse. They related this effect to resonant collective enhancement of the polarization field. Enhanced asymmetry for optimal pulse conditions is also supported by MD simulations (Martchenko *et al.*, 2005).

A pronounced resonance effect has been observed in a dual-pulse experiment on $Ag_N$ (Fennel, Döppner, *et al.*, 2007). Two pulses with optimal separation yield simultaneously higher electron energies and stronger asymmetry when compared to single-pulse excitation [see Fig. 39(a)]. Comparison of parallel and perpendicular electron yields for different energy windows as a function of pulse delay [Fig. 39(b)] shows that the asymmetry increases with electron energy. The strongest anisotropy of about 6.5 is found for the most energetic electrons [uppermost panel in Fig. 39(b)]. For all chosen energy windows a maximum yield is observed for similar delays, supporting the presence of plasmon-enhanced electron emission. VUU calculations on $Na_{147}$ (Fig. 40) show the same qualitative behavior. Off-resonance excitation induces low-energy electron emission and only a small asymmetry [Figs. 40(a) and 40(c)], while resonant dual-pulse excitation results in energetic electrons and stronger preference along the polarization axis [Fig. 40(b)]. Note that both experiment and calculation show electron energies beyond $60U_p$ along the polarization axis for resonant excitation.

By trajectory analysis it can be shown that rescattering of electrons by the cluster potential is crucial for the high-energy part of the spectrum. More specifically, corresponding electrons gain the major energy fraction within their final transit through the cluster. The importance of rescattering is well known from atomic strong-field ionization. A maximum electron energy of $10U_p$ results from backscattering of tunnel-ionized electrons upon reencounter with the mother ion at optimal laser phase [see, e.g., Walker *et al.* (1996)]. In contrast, a quasilinear transit along the laser polarization axis without deflection turns out to be optimal in clusters. The energies can exceed the $10U_p$ cutoff from atomic backscattering considerably. Two major effects contribute to the energy capture in clusters: (i) acceleration by polarization fields (Fennel, Döppner, *et al.*, 2007) and (ii) laser-field-driven acceleration (Saalmann and Rost, 2008). Within process (i), transit electrons travel in phase with the dynamic cluster polarization field produced from plasmon oscillations. A continuous increase of single-particle energy can be accomplished for fully matched trajectories. This process of surface-plasmon assisted rescattering in clusters (SPARC) supports preferential ejection of fast electrons along the laser polarization axis. It further provides an explanation for strong acceleration at the instant of resonant plasmon driving due to redistribution of collectively absorbed energy to SPARC electrons. In the simulation run of Fig. 40(b), the peak amplitude of the polarization field gradient approaches 35 GeV/m. This value corresponds to an effective intensity 25 times

higher than that of the laser pulse. Process (ii) results from the laser-driven acceleration of electrons in a quasistatic cluster potential. For passage through a deep global cluster potential, electrons acquire high transit velocities. If the velocity and the laser polarization axis are parallel and the transit occurs during a beneficial laser half cycle, electrons can be strongly accelerated by the laser field. Also such type of energy capture from rescattering, which is most effective with a deep cluster potential, produces an alignment of fast electrons. Assuming the formation of a particularly deep cluster space-charge potential for resonant collective electron excitation, this process can result in a plasmon enhancement of the electron kinetic energies as well. A detailed analysis and a corresponding scaling law for the attainable electron energy are given by Saalmann and Rost (2008). Besides possible contributions from additional many-body effects, the dynamics will contain a mixture of processes (i) and (ii). Nevertheless, mechanism (i) dominates for strong collective motion, e.g., in metallic systems at moderate intensity, while mechanism (ii) prevails with deep cluster potentials and high laser intensity.

## VII. PERSPECTIVES OF LASER-CLUSTER RESEARCH

The previous sections have shown that the field of laser-irradiated clusters is in an actively developing state. We now discuss a few promising future directions. Among those are prospects of laser pulse shaping or forthcoming light sources. Furthermore, complex environments and heterogeneous atomic compositions as well as the use of clusters for relativistic particle acceleration may open new routes for technical applications. Finally, we address some prospects and challenges of future theory developments.

### A. Laser pulse shaping and control

One intriguing perspective of light-matter coupling pertains to its active manipulation by shaping the pulse in amplitude and phase (Brixner, Damrauer, and Gerber, 2001; Brixner and Gerber, 2003). With molecules, this approach follows the suggestion of Judson and Rabitz (1992), in which a computer-controlled pulse shaper is used in combination with a learning algorithm [see Baumert *et al.* (1997) and Brixner, Damrauer, Niklaus, and Gerber (2001)], in order to achieve a selective molecular reaction. The quantum-mechanical processes can be controlled with the direct feedback from the experiment in an automated fashion, without requiring any model for the system response. This electron wave-packet engineering has become a powerful tool to realize the concept of femtochemistry (Zewail, 1980). A recent technological development further increases the possibilities and prospects of quantum control. With the technique of femtosecond polarization pulse shaping (Brixner *et al.*, 2002, 2004) it is now possible to vary intensity, instantaneous frequency, and light polarization (i.e., the degree of ellipticity as well as the orientation of the principal axes) as functions of time within a single femtosecond laser pulse. Thus, full temporal and spatial control is at reach.

For intense laser-cluster interactions, shaping the pulse in amplitude and phase can be a helpful tool to selectively steer the dynamics of charging and particle or photon emission. Basic findings along this line are the control of the Coulomb explosion by varying the laser pulse length as well as the time delay in the dual-pulse experiments as outlined in Sec. VI.B.1. For example, Fig. 36 shows the dramatic effect of the delay of two laser pulses on the charging efficiency and the energy of emitted electrons. Adaptive femtosecond control was demonstrated on the Coulomb explosion of $Xe_N$ (Zamith *et al.*, 2004). Here the signal of highly charged $Xe^{q+}$ could be optimized with the help of a simple genetic algorithm applied to an initially Fourier transform limited pulse with 100 fs duration and 230 $\mu$J energy. The procedure resulted into a sequence of two 120 fs pulses with similar amplitude and separated in time by about 500 fs, as in the optimized dual-pulse experiments (Döppner *et al.*, 2005). It is interesting to note that this two-pulse optimum has been worked out by the algorithm starting from an 80 parameter unbiased configuration. Corresponding simulations within a semiclassical molecular dynamics approach predicted that, for selected combinations of cluster size, laser intensity, and wavelength, ionization may be optimized by a three-pulse sequence (Martchenko *et al.*, 2005). In another closed-loop optimal control experiment on rare-gas clusters, pulse shaping has shown a significant potential for x-ray yield enhancement (Moore *et al.*, 2005).

Whereas the optimal-control studies on clusters were limited to an optimization of the pulse amplitude so far, the simultaneous variation of the pulse phase is still an exciting challenge. First results of such a fully unbiased adaptive fs experiment have demonstrated the controlled adjustment of charge state distributions from the Coulomb explosion of $Ag_N$ embedded in helium droplets (Truong *et al.*, 2010). In this study the optimization of the $Ag^{q+}$ charge spectrum converged to a pulse structure with a weaker prepulse and a stronger negatively chirped main pulse. However, we are far from a full theoretical understanding of the complex dynamics driven by pulses shaped in amplitude and phase. In the future, if sufficient mass-selected cluster intensity can be prepared, single ionization states and narrow-banded high-energy radiation might be realized.

### B. Toward VUV, XUV, and soft x-ray pulses

The nature of the laser-cluster coupling fundamentally changes when going from the IR regime toward excitation with VUV, XUV, or even x-ray pulses. This concerns ionization processes as well as the mechanisms of energy absorption. For excitation with IR pulses, field-driven ionization plays a crucial role for the nanoplasma generation, e.g., in rare-gas systems. The subsequent energy capture, which eventually removes electrons from the cluster, is of plasma nature and can be strongly en-

hanced through resonant collective excitations. Because of extensive plasma heating and resulting further ionization, high charge states can arise with IR pulses.

When going below about 100 nm wavelength, a value which was used in the first VUV experiments on rare-gas clusters, photoionization becomes the dominant charging mechanism for inner ionization. Concerning the energy absorption, collective effects can be disregarded as the required critical density cannot be reached and pure IBS heating prevails. In fact, the observation of surprisingly high energy capture in the first VUV experiments on clusters (see Sec. VI.A.2) has lead to substantial progress in the understanding of heating and ionization effects in dense targets (Santra and Greene, 2003; Bauer, 2004b; Siedschlag and Rost, 2004; Jungreuthmayer *et al.*, 2005; Ramunno *et al.*, 2006; Saalmann *et al.*, 2006; Georgescu *et al.*, 2007b; Ziaja *et al.*, 2007).

When further increasing the laser frequency, IBS heating becomes more and more suppressed [cf. Eq. (8)], so that photoexcitation of tightly bound electrons begins to become the leading energy capture process. Signatures of this transition have recently been observed on $Ar_N$ in intense femtosecond XUV FEL pulses at $\lambda = 32$ nm ($\hbar\omega_{las} = 38$ eV) (Bostedt *et al.*, 2008). By comparing the experimental photoelectron spectra with complementary Monte Carlo simulations, the following behavior was found. The cluster ionization first proceeds as a multistep process of direct single-photon absorption events. Electrons are released from the cluster directly without prior inner ionization and the space charge buildup results in an energy downshift for subsequent ionization steps. This shift leads to a highly nonthermal electron energy distribution. At a certain degree of ionization, the cluster potential frustrates further electron release, leading to the formation of a nanoplasma only beyond a certain threshold intensity. Even at higher intensity no strong impact of IBS heating was found. These findings are in agreement with corresponding MD results (Arbeiter and Fennel, 2010) and calculations based on kinetic transport equations (Ziaja *et al.*, 2009).

Using intense soft x-ray pulses at $\lambda = 13$ nm Hoener *et al.* (2008) found highly efficient charging of $Xe_N$ with ions up $Xe^{9+}$, which can be ascribed to the large absorption cross section of the giant atomic Xe $4d$ resonance. By surrounding $Xe_N$ with an additional argon layer it was further shown that charge recombination dynamics can be studied in the well controllable core-shell system.

Another interesting issue concerns the time-resolved monitoring of the cluster excitation and the subsequent Coulomb explosion by combining different types of pulses. For example, the ionization of rare-gas clusters may be driven by VUV radiation, as in the case of Wabnitz *et al.* (2002), whereas a subsequent IR pulse probes the collective electron response of the priorly *metallized system* (Siedschlag and Rost, 2005). A combination of VUV and XUV pulses was proposed to monitor the time-dependent ionization stages in small clusters (Georgescu *et al.*, 2007a). Another scheme uses x-ray radiation for Thomson scattering on exploding clusters or droplets, which have been initially excited by strong IR pulses (Höll *et al.*, 2007). With this scheme a fundamental understanding can be gained on highly nonstationary strongly coupled plasmas and their transition from degenerate to classical systems. The advent of x-ray free electron lasers will open direct access to the temporal development of such complex systems.

### C. Clusters in an environment

Embedding clusters into an environment or depositing them at surfaces modifies their optical responses [see Kreibig and Vollmer (1995)]. A major branch of present-day cluster research comprises systems in contact with solid surfaces [for a review see, e.g., Meiwes-Broer (2000, 2006) and Meiwes-Broer and Berndt (2007)]. An extremely rich scenery unfolds when considering the specific effects emerging from the interaction of a cluster with an environment. One finds only small shifts for the Mie plasmon resonances of metal clusters embedded in inert matter (Diederich *et al.*, 2002; Fehrer, Dinh, Suraud, and Reinhard, 2007) and larger ones for contact with conducting material (Pinchuk *et al.*, 2004). Details of the excitation spectrum, however, are rather sensitive to the interface. For example, the interface influences the spectral fragmentation and the plasmon damping [for experimental assessment see, e.g., Hendrich *et al.* (2003) and Ziegler *et al.* (2004)]. Large effects from the environment are to be expected in the reaction dynamics at high excitations. For example, the presence of a matrix can significantly alter the expansion dynamics of the embedded target. Such processes are of particular interest for single shot x-ray structure analysis with FEL pulses. In order to improve the quality of the diffraction pattern it has been suggested to retard target explosion by adding a surrounding nanomatrix (e.g., a few layers of rage-gas atoms) as a sacrifical tamper layer (Gnodtke *et al.*, 2009; Hau-Riege *et al.*, 2010).

A theoretical example for IR excitation is shown in Fig. 41. This figure compares three test cases, $Na_8$ as a small metal cluster, $Na_8$ embedded in $Ar_{434}$ (a large rare-gas cluster as model for a matrix), and pure $Ar_{447}$, all three exposed to the same laser pulse. The laser pulse leads to a charge state $q = 3$ of $Na_8$. In the free case (bottom panel) this induces a Coulomb explosion. The situation is quite different for $Na_8$ in $Ar_{434}$ matrix. The metal cluster is again highly excited and starts to explode; but the explosion is stopped by the Ar atoms which efficiently absorb the excitation energy of the system (lower middle panel). The Ar matrix is perturbed and exhibits monopole oscillations but of much smaller amplitude than $Na_8$ (upper middle panel). The upper panel of Fig. 41 shows the case of pure $Ar_{447}$. Under the same laser conditions, one can see that $Ar_{447}$ remains essentially unperturbed, showing no electron emission and only extremely weak breathing oscillations. Obviously, $Na_8$ acts here as a chromophore, absorbing energy from the laser pulse and transferring it to the environment. The example shows that the combination of two materials changes the reaction dynamics of either system dramatically. One can easily imagine that putting clus-

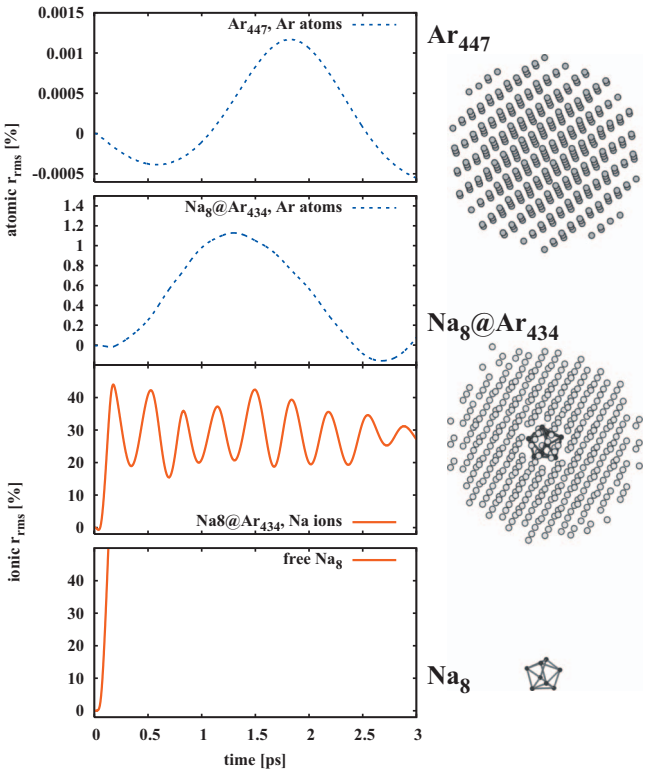


FIG. 41. (Color) Time evolution of the root mean square radius $r_{rms}$ of free $Na_8$ (bottom), $Na_8$ embedded in $Ar_{434}$ (middle), and pure $Ar_{447}$ (top) after irradiation with $2.4\times10^{12}$ W/cm$^2$, 33 fs, and 650 nm. Calculations have been performed using TDDFT for Na valence electrons and MD for $Na^+$ ions and Ar atoms. Note the different scales for $r_{rms}$ in the two upper panels. From Fehrer, Dinh, Bär, *et al.*, 2007.

ters in contact with various substrates produces interesting scientific questions and offers technical applications in the field of nanotechnology. We mention in the following a few aspects to give an idea of the enormous possibilities, concentrating on optical properties.

When depositing $Au_N$ on a semiconductor surface the change of optical cluster properties can be exploited to producing enhanced photocurrent (Schaadt *et al.*, 2005). There are promising applications, e.g., in medicine where the frequency selective optical coupling of organically coated metal clusters attached to biological tissue may be used for diagnosis (Bruchez *et al.*, 1998; Mayer *et al.*, 2001; Dubertret *et al.*, 2002; Simberg *et al.*, 2007) or, in the case of stronger laser fields, for localized heating in therapy (Khlebtsov *et al.*, 2006). The field amplification effect is of interest in many other materials and applications [see, e.g., the study of localized melting for the generic combination of Au clusters embedded in ice (Richardson *et al.*, 2006)]. The strong coupling to light may be used for more than just heating. Ensembles of size and shape-selected clusters on a surface are produced by laser-assisted growth (Wenzel *et al.*, 1999; Ouacha *et al.*, 2005). A dedicated modification of the shape for embedded Ag clusters is demonstrated by Perner *et al.* (2000) and Dahmen *et al.* (2006). Time scales and mechanisms of energy transport are thus issues in various fields. Theoretical analysis has yet to deal with the variety of material combinations. For an example using the generic test system of metal cluster in a rare-gas matrix, see Fehrer, Dinh, Bär, *et al.* (2007) and Fehrer *et al.* (2008). A thorough study of surface-deposited cluster subject to strong laser pulses is still a matter of future studies.

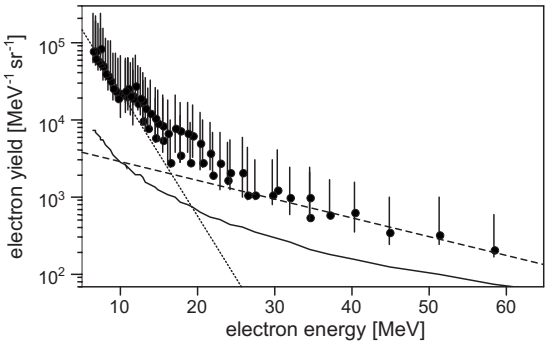


FIG. 42. Electron kinetic energy distribution resulting from irradiation of large Ar particles (micron-sized diameter) in Ar-gas environment by a superintense laser ($3.5\times10^{19}$ W/cm$^2$). The solid curve shows the detection threshold. Straight lines indicate fits to thermal distributions, dashed for $T$=18.8 MeV, and dotted for $T$=2.8 MeV. Adapted from Fukuda *et al.*, 2007.

### D. Relativistic particle acceleration with clusters

Strong laser fields impinging on clusters can drive interesting electron dynamics. For an example from the moderate intensity domain ($\sim10^{14}$ W/cm$^2$), Fennel, Döppner, *et al.* (2007) described a cascadelike acceleration mechanism based on resonant field amplification in individual clusters (see Sec. VI.B.3). In the regime of $10^{15}$–$10^{17}$ W/cm$^2$ electron energies from keV up to several hundreds of keV are reported (Shao *et al.*, 1996; Chen, Park, Hong, Choi, *et al.*, 2002; Springate *et al.*, 2003), emitted in the transverse direction to the laser propagation axis. Beyond a few tens of keV the emission is most likely due to macroscopic plasma wave-breaking effects in a very dense cluster beam as is further supported by a pronounced forward peak in the emission (Chen, Park, Hong, Kim, *et al.*, 2002). Moreover, there are few examples close to or in the relativistic regime ($10^{19}$ W/cm$^2$). From studies on bulk and dense atomic gases it is known that charged particles can be accelerated by the plasma wakefield to large kinetic energies [for a detailed theoretical discussion see Pukhov and Meyer-ter-Vehn (2002) and for a recent experimental example see Karsch *et al.* (2007)]. There exist plans to employ the effect to build fairly inexpensive laser-driven table-top free electron lasers (Grüner *et al.*, 2007). Indications for special relativistic electron acceleration mechanisms with clusters have been reported in a study on large Ar particles in a low-density background gas (Fukuda *et al.*, 2007). The example in Fig. 42 shows the achieved electron kinetic energies. On the basis of simulation results, the two temperatures have been associated with two different generating mechanisms. The

lower-energy electrons stem from acceleration in a distorted wakefield. In contrast, the high-energy electrons are removed from the clusters with already relativistic energies and then further accelerated by the laser pulse directly. The kinetic energies observed here are still far below what can emerge from bulk plasma. However, whereas optimum conditions, advantages, and disadvantages have yet to be worked out, the example proves the feasibility of relativistic particle acceleration with clusters. A recent PIC simulation supports the generation of relativistic multi-MeV attosecond electron bunches from sub-$\mu$m He droplets (Liseykina *et al.*, 2010). Moreover, the use of clusters as dense electron containers for free-space electron acceleration, e.g., with radially polarized laser beams, might be promising for generating ultrashort electron bunches with durations down to the attosecond domain at up to GeV energy (Varin and Piche, 2006; Karmakar and Pukhov, 2007).

### E. Challenges for theory

The theoretical description of laser-cluster dynamics requires covering different scales of length, time, and energy. This difficulty usually hampers a fully microscopic treatment of all degrees of freedom. Fortunately, resolving a certain set of scales is often sufficient, as the main response channels in a particular scenario are determined by the type of excitation (e.g., by laser intensity, frequency, pulse length) and by the size or structure of the target. We have seen in Sec. III that there exists a bunch of theoretical approaches, ranging from fully microscopic ones to macroscopic ones, which are applicable within certain windows of size and energy. Their limitations result from both formal constraints, e.g., due to the level on which correlations and quantum effects are resolved, and practical ones such as numerical expense. To promote the development of more elaborate methods and schemes with wider ranges of applicability, we see at least two promising directions.

The first and most straightforward path is improvement of particular methods along with the rapid development of high-performance computers. For instance, the impressive growth of numerical power allows application of fully correlated quantum approaches to systems with several electrons, e.g., with the efficient handling of few-body wave functions by MCTDH (Beck *et al.*, 2000) or MCTDHF methods (Caillat *et al.*, 2005). This opens a route to explore truly correlated electron dynamics including continuum and intermediate excited states [for an example on a molecular system see Sukiasyan *et al.* (2009)]. A more fundamental challenge concerns the inclusion of dynamical correlations in mean-field quantum theories such as TDLDA in the sense of a quantum counterpart to the semiclassical description within VUU. On the classical level, efficient numerical schemes and large-scale parallelization promise the feasibility of up to gigaparticle simulations.

A second frontier concerns the connection of different treatments in terms of multilevel or multiscale methods. A well-known example for biological and chemical applications are mixed quantum mechanic and molecular dynamic approaches [see, e.g., Bakowies and Thiel (1996)]. For clusters the combination of different levels has turned out to be successful, e.g., within MD and hydrodynamic schemes for strong-field excitations, where the quantum nature of inner ionization is taken into account via effective rates and cross sections. The connection of different treatments, however, requires interfaces, the validation of which is a challenge. Firm links between the approaches and reliable interfaces, e.g., within overlapping zones similar to those shown in Fig. 6, are therefore highly desirable and have far-reaching implications. One example could be the connection of an explicit atomic-scale quantum treatment of inner ionization with a more coarse-grained semiclassical or even classical treatment of quasifree and continuum electrons. This would be of much interest for strong-field laser-cluster interactions in a wide range of laser frequencies, i.e., from the IR up to the x-ray domain. Another challenging aspects are strong-field excitations of larger clusters and particles in the IR range, where propagation effects of the light field can no longer be neglected. Here a combination of molecular dynamics techniques for evaluating the short-range part of the interactions combined with electromagnetic particle-in-cell concepts for describing the long-range component of the Coulomb and radiation fields might be promising. Last, such neighboring approaches could also be combined in a sequential way, e.g., to resolve the laser excitation microscopically, whereas the long-term behavior is described with a less expensive scheme.

Along these lines the field of laser-cluster dynamics will certainly be inspired by forthcoming developments in other branches such as atomic, molecular, and plasma physics.

## ACKNOWLEDGMENTS

We thank Gustav Gerber for fruitful discussions. Th.F., J.T., and K.-H.M.-B. gratefully acknowledge financial support by the Deutsche Forschungsgemeinschaft (DFG) within Grant No. SFB 652. Computer time has been provided by the HLRN Computing Center. This work was further supported by the DFG (Grant No. RE 322/10-1), the French-German exchange program PROCOPE of the DAAD (Grant No. 07523TE), the Institut Universitaire de France, the Agence Nationale de la Recherche (Grant No. ANR-06-BLAN-0319-02), the Humboldt Foundation, a Gay-Lussac Price, the French computational facilities CalMip, IDRIS, and CINES, and the Computing Center of the University of Erlangen.

## REFERENCES

Alonso, J. A., 2006, *Structure and Properties of Atomic Clusters* (Imperial College, London).

Amar, F. G., J. Smaby, and T. J. Preston, 2005, J. Chem. Phys. **122**, 244717.

Ammosov, M. V., N. B. Delone, and V. P. Krainov, 1986, Zh.

Eksp. Teor. Fiz. **91**, 2008 [Sov. Phys. JETP **64**, 1191 (1986)].
Ancilotto, F., and F. Togio, 1995, Z. Phys. B: Condens. Matter **98**, 309.
Arbeiter, M., and T. Fennel, 2010, e-print arXiv:1005.4004.
Arnold, D. W., S. E. Bradforth, T. N. Kitsopoulos, and D. M. Neumark, 1991, J. Chem. Phys. **95**, 8753.
Ashcroft, N. W., and N. D. Mermin, 1976, *Solid State Physics* (Saunders College, Philadelphia).
Assion, A., T. Baumert, M. Bergt, T. Brixner, B. Kiefer, V. Seyfried, M. Strehle, and G. Gerber, 1998, Science **282**, 919.
Attwood, D. T., 2007, *Soft X-Rays and Extreme Ultraviolet Radiation: Principles and Applications* (Cambridge University Press, Cambridge).
Augst, S., D. Strickland, D. D. Meyerhofer, S. L. Chin, and J. H. Eberly, 1989, Phys. Rev. Lett. **63**, 2212.
Auguste, T., P. Monot, L. A. Lompre, G. Mainfray, and C. Manus, 1992, J. Phys. B **25**, 4181.
Ayvazyan, V., *et al.*, 2006, Eur. Phys. J. D **37**, 297.
Babst, J., and P.-G. Reinhard, 1997, Z. Phys. D: At., Mol. Clusters **42**, 209.
Baguenard, B., J. C. Pinaré, C. Bordas, and M. Broyer, 2001, Phys. Rev. A **63**, 023204.
Bakowies, D., and W. Thiel, 1996, J. Chem. Phys. **100**, 10580.
Ball, J. A., J. A. Wheeler, and E. L. Firemen, 1973, Rev. Mod. Phys. **45**, 333.
Banine, V., and R. Moors, 2004, J. Phys. D **37**, 3207.
Barborini, E., P. Piseri, and P. Milani, 1999, J. Phys. D **32**, 105.
Barnes, J., and P. Hut, 1986, Nature (London) **324**, 446.
Bartels, C., C. Hock, J. Huwer, R. Kuhnen, J. Schwöbel, and B. v. Issendorff, 2009, Science **323**, 1323.
Bartelt, A., J. D. Close, F. Federmann, N. Quaas, and J. P. Toennies, 1996, Phys. Rev. Lett. **77**, 3525.
Batani, D., C. J. Joachain, S. Martellucci, and A. N. Chester, 2001, Eds., *Atoms, Solids, and Plasmas in Super-Intense Laser Fields* (Kluwer, New York).
Bauer, D., 2004a, J. Phys. B **37**, 3085.
Bauer, D., 2004b, Appl. Phys. B: Lasers Opt. **78**, 801.
Baumert, T., T. Brixner, V. Seyfried, M. Strehle, and G. Gerber, 1997, Appl. Phys. B: Lasers Opt. **65**, 779.
Beck, M. H., A. Jackle, G. A. Worth, and H. D. Meyer, 2000, Phys. Rep. **324**, 1.
Belkacem, M., F. Megi, P.-G. Reinhard, E. Suraud, and G. Zwicknagel, 2006a, Phys. Rev. A **73**, 051201(R).
Belkacem, M., F. Megi, P.-G. Reinhard, E. Suraud, and G. Zwicknagel, 2006b, Eur. Phys. J. D **40**, 247.
Benis, E. P., J. F. Xia, X. M. Tong, M. Faheem, M. Zamkov, B. Shan, P. Richard, and Z. Chang, 2004, Phys. Rev. A **70**, 025401.
Bergersen, H., M. Abu-Samha, J. Harnes, O. Björneholm, S. Svensson, L. J. Sæthre, and K. J. Børve, 2006, Phys. Chem. Chem. Phys. **8**, 1891.
Bertsch, G. F., and S. Das Gupta, 1988, Phys. Rep. **160**, 189.
Bethe, H. A., and E. E. Salpeter, 1977, *Quantum Mechanics of One- and Two-Electron Atoms* (Plenum, New York).
Beutel, V., H. G. Kramer, G. L. Bhale, M. Kuhn, K. Weyers, and W. Demtröder, 1993, J. Chem. Phys. **98**, 2699.
Blaise, P., S. A. Blundell, and C. Guet, 1997, Phys. Rev. B **55**, 15856.
Bloch, F., 1933, Z. Phys. **81**, 363.
Blum, V., G. Lauritsch, J. A. Maruhn, and P.-G. Reinhard, 1992, J. Comput. Phys. **100**, 364.
Bonačić-Koutecký, V., P. Fantucci, and J. Koutecký, 1991, Chem. Rev. (Washington, D.C.) **91**, 1035.
Bornath, T., P. Hilse, and M. Schlanges, 2007a, Laser Phys. **17**, 591.
Bornath, T., P. Hilse, and M. Schlanges, 2007b, Contrib. Plasma Phys. **47**, 402.
Bostedt, C., *et al.*, 2008, Phys. Rev. Lett. **100**, 133401.
Bouma, B., T. S. Luk, K. Boyer, and C. K. Rhodes, 1993, J. Opt. Soc. Am. B **10**, 1180.
Brabec, T., and F. Krausz, 2000, Rev. Mod. Phys. **72**, 545.
Brack, M., 1993, Rev. Mod. Phys. **65**, 677.
Bragg, A. E., J. R. R. Verlet, A. Kammrath, O. Cheshnovsky, and D. M. Neumark, 2005, J. Chem. Phys. **122**, 054314.
Bréchignac, C., P. Cahuzac, F. Carlier, M. de Frutos, R. N. Barnett, and U. Landman, 1994, Phys. Rev. Lett. **72**, 1636.
Breizman, B. N., A. V. Arefiev, and M. V. Fomyts'kyi, 2005, Phys. Plasmas **12**, 056706.
Brixner, T., N. H. Damrauer, and G. Gerber, 2001, in *Advances in Atomic, Molecular, and Optical Physics*, edited by B. Bederson and H. Walther (Academic, San Diego), pp. 1–54.
Brixner, T., N. H. Damrauer, P. Niklaus, and G. Gerber, 2001, Nature (London) **414**, 57.
Brixner, T., and G. Gerber, 2003, ChemPhysChem **4**, 418.
Brixner, T., G. Krampert, P. Niklaus, and G. Gerber, 2002, Appl. Phys. B: Lasers Opt. **74**, S133.
Brixner, T., G. Krampert, T. Pfeifer, R. Selle, G. Gerber, M. Wollenhaupt, O. Graefe, C. Horn, D. Liese, and T. Baumert, 2004, Phys. Rev. Lett. **92**, 208301.
Bruchez, M., Jr., M. Moronne, P. Gin, S. Weiss, and A. P. Alivisato, 1998, Science **281**, 2013.
Brumer, P., and M. Shapiro, 1995, Sci. Am. (Int. Ed.) **272**, 56.
Brunel, F., 1987, Phys. Rev. Lett. **59**, 52.
Bryan, W. A., *et al.*, 2006, Nat. Phys. **2**, 379.
Buck, U., and R. Krohne, 1996, J. Chem. Phys. **105**, 5408.
Caillat, J., J. Zanghellini, M. Kitzler, O. Koch, W. Kreuzer, and A. Scrinzi, 2005, Phys. Rev. A **71**, 012712.
Calvayrac, F., P.-G. Reinhard, E. Suraud, and C. A. Ullrich, 2000, Phys. Rep. **337**, 493.
Campbell, E. E. B., K. Hansen, K. Hoffmann, G. Korn, M. Tchaplyguine, M. Wittmann, and I. V. Hertel, 2000, Phys. Rev. Lett. **84**, 2128.
Ceperley, D. M., and B. J. Alder, 1980, Phys. Rev. Lett. **45**, 566.
Cha, C. Y., G. Ganteför, and W. Eberhardt, 1992, Rev. Sci. Instrum. **63**, 5661.
Chang, Z. H., A. Rundquist, H. W. Wang, M. M. Murnane, and H. C. Kapteyn, 1997, Phys. Rev. Lett. **79**, 2967.
Chen, L. M., J. J. Park, K. H. Hong, I. W. Choi, J. L. Kim, J. Zhang, and C. H. Nam, 2002, Phys. Plasmas **9**, 3595.
Chen, L. M., J. J. Park, K.-H. Hong, J. L. Kim, J. Zhang, and C. H. Nam, 2002, Phys. Rev. E **66**, 025402(R).
Cheshnovsky, O., K. J. Taylor, J. Conceicao, and R. E. Smalley, 1990, Phys. Rev. Lett. **64**, 1785.
Corkum, P. B., 1993, Phys. Rev. Lett. **71**, 1994.
Corkum, P. B., and F. Krausz, 2007, Nat. Phys. **3**, 381.
Dahmen, C., A. N. Sprafke, H. Dieker, M. Wuttig, and G. v. Plessen, 2006, Appl. Phys. Lett. **88**, 011923.
Dammasch, M., M. Dörr, U. Eichmann, E. Lenz, and W. Sandner, 2001, Phys. Rev. A **64**, 061402(R).
de Heer, W. A., 1993, Rev. Mod. Phys. **65**, 611.
Deiss, C., N. Rohringer, J. Burgdörfer, E. Lamour, C. Prigent, J. P. Rozet, and D. Vernhet, 2006, Phys. Rev. Lett. **96**, 013203.
Della-Sala, F., and A. Görling, 2003, Int. J. Quantum Chem. **91**, 131.
Diederich, T., T. Döppner, T. Fennel, J. Tiggesbäumker, and K.-H. Meiwes-Broer, 2005, Phys. Rev. A **72**, 023203.

Diederich, T., J. Tiggesbäumker, and K.-H. Meiwes-Broer, 2002, J. Chem. Phys. **116**, 3263.
Ditmire, T., 1998, Phys. Rev. A **57**, R4094.
Ditmire, T., T. Donnelly, R. W. Falcone, and M. D. Perry, 1995, Phys. Rev. Lett. **75**, 3122.
Ditmire, T., T. Donnelly, A. M. Rubenchik, R. W. Falcone, and M. D. Perry, 1996, Phys. Rev. A **53**, 3379.
Ditmire, T., R. A. Smith, J. W. G. Tisch, and M. H. R. Hutchinson, 1997, Phys. Rev. Lett. **78**, 3121.
Ditmire, T., E. Springate, J. W. G. Tisch, Y. L. Shao, M. B. Mason, N. Hay, J. P. Marangos, and M. H. R. Hutchinson, 1998, Phys. Rev. A **57**, 369.
Ditmire, T., J. W. G. Tisch, E. Springate, M. B. Mason, N. Hay, J. P. Marangos, and M. H. R. Hutchinson, 1997a, Phys. Rev. Lett. **78**, 2732.
Ditmire, T., J. W. G. Tisch, E. Springate, M. B. Mason, N. Hay, R. A. Smith, J. Marangos, and M. H. R. Hutchinson, 1997b, Nature (London) **386**, 54.
Ditmire, T., J. Zweiback, V. P. Yanovsky, T. E. Cowan, G. Hays, and K. B. Wharton, 1999, Nature (London) **398**, 489.
Dobosz, S., M. Lezius, M. Schmidt, P. Meynadier, M. Perdrix, D. Normand, J. P. Rozet, and D. Vernhet, 1997, Phys. Rev. A **56**, R2526.
Dobson, J. F., 1994, Phys. Rev. Lett. **73**, 2244.
Domps, A., P. L'Eplattenier, P.-G. Reinhard, and E. Suraud, 1997, Ann. Phys. (Leipzig) **509**, 455.
Domps, A., P.-G. Reinhard, and E. Suraud, 1998a, Phys. Rev. Lett. **81**, 5524.
Domps, A., P.-G. Reinhard, and E. Suraud, 1998b, Phys. Rev. Lett. **80**, 5520.
Domps, A., P.-G. Reinhard, and E. Suraud, 2000, Ann. Phys. **280**, 211.
Donnelly, T. D., T. Ditmire, K. Neuman, M. D. Perry, and R. W. Falcone, 1996, Phys. Rev. Lett. **76**, 2472.
Döppner, T., T. Diederich, A. Przystawik, N. X. Truong, T. Fennel, J. Tiggesbäumker, and K.-H. Meiwes-Broer, 2007, Phys. Chem. Chem. Phys. **9**, 4639.
Döppner, T., T. Fennel, T. Diederich, J. Tiggesbäumker, and K.-H. Meiwes-Broer, 2005, Phys. Rev. Lett. **94**, 013401.
Döppner, T., T. Fennel, P. Radcliffe, J. Tiggesbäumker, and K.-H. Meiwes-Broer, 2006, Phys. Rev. A **73**, 031202(R).
Döppner, T., J. P. Müller, A. Przystawik, S. Göde, J. Tiggesbäumker, K.-H. Meiwes-Broer, C. Varin, L. Ramunno, T. Brabec, and T. Fennel, 2009, e-print arXiv:0908.2145.
Döppner, T., J. Müller, A. Przystawik, J. Tiggesbäumker, and K.-H. Meiwes-Broer, 2007, Eur. Phys. J. D **43**, 261.
Döppner, T., S. Teuber, T. Diederich, T. Fennel, P. Radcliffe, J. Tiggesbäumker, and K.-H. Meiwes-Broer, 2003, Eur. Phys. J. D **24**, 157.
Döppner, T., S. Teuber, M. Schumacher, J. Tiggesbäumker, and K.-H. Meiwes-Broer, 2000, Appl. Phys. B: Lasers Opt. **71**, 357.
Dorchies, F., T. Caillaud, F. Blasco, C. Bonté, H. Jouin, S. Micheau, B. Pons, and J. Stevefelt, 2005, Phys. Rev. E **71**, 066410.
Dreizler, R. M., and E. K. U. Gross, 1990, *Density Functional Theory: An Approach to the Quantum Many-Body Problem* (Springer, Berlin).
Dubertret, B., P. Skourides, D. J. Norris, V. Noireaux, A. H. Brivanlou, and A. Libchaber, 2002, Science **298**, 1759.
Eberhardt, W., P. Fayet, D. M. Cox, Z. Fu, A. Kaldor, R. Sherwood, and D. Sondericker, 1990, Phys. Rev. Lett. **64**, 780.
Echt, O., and E. Recknagel, 1991, Eds., *Proceedings of the Fifth International Symposium on Small Particles and Inorganic Clusters ISSPIC 5* (Springer, Berlin).
Ekardt, W., 1999, Ed., *Metal Clusters* (Wiley, New York).
Ellert, C., M. Schmidt, H. Haberland, V. Veyret, and V. Bonačić-Koutecký, 2002, J. Chem. Phys. **117**, 3711.
Eppink, A. T. J. B., and D. H. Parker, 1997, Rev. Sci. Instrum. **68**, 3477.
Fehrer, F., P. M. Dinh, M. Bär, P.-G. Reinhard, and E. Suraud, 2007, Eur. Phys. J. D **45**, 447.
Fehrer, F., P. M. Dinh, P.-G. Reinhard, and E. Suraud, 2008, Comput. Mater. Sci. **42**, 203.
Fehrer, F., P. M. Dinh, E. Suraud, and P.-G. Reinhard, 2007, Phys. Rev. B **75**, 235418.
Fehrer, F., P.-G. Reinhard, and E. Suraud, 2006, Appl. Phys. A: Mater. Sci. Process. **82**, 145.
Fehrer, F., P.-G. Reinhard, E. Suraud, E. Giglio, B. Gervais, and A. Ipatov, 2005, Appl. Phys. A: Mater. Sci. Process. **82**, 151.
Feit, M. D., J. A. Fleck, and A. Steiger, 1982, J. Comput. Phys. **47**, 412.
Feldhaus, J., J. Arthur, and J. B. Hastings, 2005, J. Phys. B **38**, S799.
Fennel, T., G. F. Bertsch, and K.-H. Meiwes-Broer, 2004, Eur. Phys. J. D **29**, 367.
Fennel, T., T. Döppner, J. Passig, C. Schaal, J. Tiggesbäumker, and K.-H. Meiwes-Broer, 2007, Phys. Rev. Lett. **98**, 143401.
Fennel, T., and J. Köhn, 2008, in *Computational Many-Particle Physics*, edited by H. Fehske, R. Schneider, and A. Weisse, Lecture Notes in Physics Vol. 739 (Springer, Berlin), pp. 255–273.
Fennel, T., L. Ramunno, and T. Brabec, 2007, Phys. Rev. Lett. **99**, 233401.
Feret, L., E. Suraud, F. Calvayrac, and P.-G. Reinhard, 1996, J. Phys. B **29**, 4477.
Fermi, E., 1928, Z. Phys. **48**, 73.
Ford, J. V., Q. Zhong, L. Poth, and A. W. Castleman, Jr., 1999, J. Chem. Phys. **110**, 6257.
Fork, R. L., B. I. Greene, and C. V. Shank, 1981, Appl. Phys. Lett. **38**, 671.
Fukuda, Y., Y. Kishimoto, T. Masaki, and K. Yamakawa, 2006, Phys. Rev. A **73**, 031201(R).
Fukuda, Y., K. Yamakawa, Y. Akahane, M. Aoyama, N. Inoue, H. Ueda, and Y. Kishimoto, 2003, Phys. Rev. A **67**, 061201(R).
Fukuda, Y., *et al.*, 2007, Phys. Lett. A **363**, 130.
Fukuda, Y., *et al.*, 2008, Appl. Phys. Lett. **92**, 121110.
Ganteför, G., A. Handschuh, H. Möller, C. Y. Cha, P. S. Bechthold, and W. Eberhardt, 1996, Surf. Rev. Lett. **3**, 399.
Ganteför, G., K.-H. Meiwes-Broer, and H. O. Lutz, 1988, Phys. Rev. A **37**, 2716.
Georgescu, I., U. Saalmann, and J. M. Rost, 2007a, Phys. Rev. Lett. **99**, 183002.
Georgescu, I., U. Saalmann, and J. M. Rost, 2007b, Phys. Rev. A **76**, 043203.
Gets, A. V., and V. P. Krainov, 2006, J. Phys. B **39**, 1787.
Giglio, E., P.-G. Reinhard, and E. Suraud, 2003, Phys. Rev. A **67**, 043202.
Giglio, E., E. Suraud, and P.-G. Reinhard, 2002, Ann. Phys. **11**, 291.
Gnodtke, C., U. Saalmann, and J. M. Rost, 2009, Phys. Rev. A **79**, 041201(R).
Goodworth, T. R. J., W. A. Bryan, I. D. Williams, and W. R. Newell, 2005, J. Phys. B **38**, 3083.

Götz, T., M. Buck, C. Dressler, F. Eisert, and F. Träger, 1995, Appl. Phys. A: Mater. Sci. Process. **60**, 607.
Goyal, S., D. L. Schutt, and G. Scoles, 1992, Phys. Rev. Lett. **69**, 933.
Gresh, N., O. Parisel, and C. Giessner-Prettre, 1999, J. Mol. Struct. **458**, 27.
Griffin, D. C., C. Bottcher, M. S. Pindzola, S. M. Younger, D. C. Gregory, and D. H. Crandall, 1984, Phys. Rev. A **29**, 1729.
Grillon, G., *et al.*, 2002, Phys. Rev. Lett. **89**, 065005.
Gross, E. K. U., J. F. Dobson, and M. Petersilka, 1996, Top. Curr. Chem. **181**, 81.
Grüner, F., *et al.*, 2007, Appl. Phys. B: Lasers Opt. **86**, 431.
Guan, J. G., M. E. Casida, A. M. Köster, and D. R. Salahub, 1995, Phys. Rev. B **52**, 2184.
Guliamov, O., L. Kronik, and K. A. Jackson, 2005, J. Chem. Phys. **123**, 204312.
Haberland, H., 1994, Ed., *Clusters of Atoms and Molecules 1 and 2*, Springer Series in Chemical Physics Vols. 52 and 56 (Springer, Berlin).
Haberland, H., Z. Insepov, and M. Moseler, 1993, Z. Phys. D: At., Mol. Clusters **26**, 229.
Haberland, H., M. Karrais, M. Mall, and Y. Thurner, 1992, J. Vac. Sci. Technol. A **10**, 3266.
Hagena, O. F., 1974, in *Molecular Beams and Low Density Gas Dynamics*, edited by P. P. Wegener (Dekker, New York), p. 93.
Hagena, O. F., 1981, Surf. Sci. **106**, 101.
Hagena, O. F., 1987, Z. Phys. D: At., Mol. Clusters **4**, 291.
Hansch, P., M. A. Walker, and L. D. Van Woerkom, 1996, Phys. Rev. A **54**, R2559.
Hansson, B. A. M., O. Hemberg, H. M. Hertz, M. Berglund, H. J. Choi, B. Jacobsson, E. Janin, S. Mosesson, L. Rymell, J. Thoresen, and M. Wilner, 2004, Rev. Sci. Instrum. **75**, 2122.
Hartmann, M., R. E. Miller, J. P. Toennies, and A. Vilesov, 1995, Phys. Rev. Lett. **75**, 1566.
Hatsui, T., H. Setoyama, N. Kosugi, B. Wassermann, I. L. Bradeanu, and E. Rühl, 2005, J. Chem. Phys. **123**, 154304.
Hau-Riege, S. P., S. Boutet, A. Barty, S. Bajt, M. J. Bogan, M. Frank, J. Andreasson, B. Iwan, M. M. Seibert, J. Hajdu, A. Sakdinawat, J. Schulz, R. Treusch, and H. N. Chapman, 2010, Phys. Rev. Lett. **104**, 068801.
Heck, A. J. R., and D. W. Chandler, 1995, Annu. Rev. Phys. Chem. **46**, 335.
Heidenreich, A., I. Last, and J. Jortner, 2007, J. Chem. Phys. **127**, 074305.
Hendrich, C., J. Bosbach, F. Stietz, F. Hubenthal, T. Vartanyan, and F. Träger, 2003, Appl. Phys. B: Lasers Opt. **76**, 869.
Hilse, P., M. Moll, M. Schlanges, and T. Bornath, 2009, Laser Phys. **19**, 428.
Hirokane, M., S. Shimizu, M. Hashida, S. Okada, S. Okihara, F. Sato, T. Iida, and S. Sakabe, 2004, Phys. Rev. A **69**, 063201.
Hirschfelder, J. O., C. F. Curtiss, and R. Bird, 1954, *Molecular Theory of Gases and Liquids* (Wiley, New York).
Ho, J., K. M. Ervin, and W. C. Lineberger, 1990, J. Chem. Phys. **93**, 6987.
Hoener, M., C. Bostedt, H. Thomas, L. Landt, E. Eremina, H. Wabnitz, T. Laarmann, R. Treusch, A. R. B. de Castro, and T. Möller, 2008, J. Phys. B **41**, 181001.
Hoffmann, M. A., G. Wrigge, B. v. Issendorff, J. Müller, G. Ganteför, and H. Haberland, 2001, Eur. Phys. J. D **16**, 9.
Höll, A., *et al.*, 2007, High Energy Density Phys. **3**, 120.
Ievlev, D., I. Rabin, W. Schulze, and G. Ertl, 2000, Chem. Phys. Lett. **328**, 142.
Ishikawa, K., and T. Blenski, 2000, Phys. Rev. A **62**, 063204.
Islam, M. R., U. Saalmann, and J. M. Rost, 2006, Phys. Rev. A **73**, 041201(R).
Issac, R. C., G. Vieux, B. Ersfeld, E. Brunetti, S. P. Jamison, J. Gallacher, D. Clark, and D. A. Jaroszynski, 2004, Phys. Plasmas **11**, 3491.
Jha, J., D. Mathur, and M. Krishnamurthy, 2006, Appl. Phys. Lett. **88**, 041107.
Judson, R. S., and H. Rabitz, 1992, Phys. Rev. Lett. **68**, 1500.
Jungreuthmayer, C., M. Geissler, J. Zanghellini, and T. Brabec, 2004, Phys. Rev. Lett. **92**, 133401.
Jungreuthmayer, C., L. Ramunno, J. Zanghellini, and T. Brabec, 2005, J. Phys. B **38**, 3029.
Jurek, Z., G. Faigel, and M. Tegze, 2004, Eur. Phys. J. D **29**, 217.
Kadanoff, L. P., and G. Baym, 1962, *Quantum Statistical Mechanics* (Benjamin, New York).
Karmakar, A., and A. Pukhov, 2007, Laser Part. Beams **25**, 371.
Karsch, S., *et al.*, 2007, New J. Phys. **9**, 415.
Keldysh, L. V., 1965, Sov. Phys. JETP **20**, 1307.
Keller, U., 2003, Nature (London) **424**, 831.
Khlebtsov, B., V. Zharov, A. Melnikov, V. Tuchin, and N. Khlebtsov, 2006, Nanotechnology **17**, 5167.
Kleibert, A., J. Passig, K.-H. Meiwes-Broer, M. Getzlaff, and J. Bansmann, 2007, J. Appl. Phys. **101**, 114318.
Klein-Wiele, J. H., P. Simon, and H. G. Rubahn, 1999, Opt. Commun. **161**, 42.
Köhn, J., R. Redmer, K.-H. Meiwes-Broer, and T. Fennel, 2008, Phys. Rev. A **77**, 033202.
Köller, L., M. Schumacher, J. Köhn, S. Teuber, J. Tiggesbäumker, and K.-H. Meiwes-Broer, 1999, Phys. Rev. Lett. **82**, 3783.
Kondo, K., M. Mori, and T. Shiraishi, 2002, Appl. Surf. Sci. **197**, 138.
Kostko, O., B. Huber, M. Moseler, and B. v. Issendorff, 2007, Phys. Rev. Lett. **98**, 043401.
Kou, J. K., V. Zhakhovskii, S. Sakabe, K. Nishihara, S. Shimizu, S. Kawato, M. Hashida, K. Shimizu, S. Bulanov, Y. Izawa, Y. Kato, and N. Nakashima, 2000, J. Chem. Phys. **112**, 5012.
Krainov, V. P., 2000, J. Phys. B **33**, 1585.
Krainov, V. P., and M. B. Smirnov, 2002, Phys. Rep. **370**, 237.
Krause, J. L., K. J. Schafer, and K. C. Kulander, 1992, Phys. Rev. Lett. **68**, 3535.
Krause, P., T. Klamroth, and P. Saalfrank, 2005, J. Chem. Phys. **123**, 074105.
Kreibig, U., and M. Vollmer, 1995, *Optical Properties of Metal Clusters*, Springer Series in Materials Science Vol. 25 (Springer, Berlin).
Krishnamurthy, M., J. Jha, D. Mathur, C. Jungreuthmayer, L. Ramunno, J. Zanghellini, and T. Brabec, 2006, J. Phys. B **39**, 625.
Krishnamurthy, M., D. Mathur, and V. Kumarappan, 2004, Phys. Rev. A **69**, 033202.
Kruit, P., and F. H. Read, 1983, J. Phys. E **16**, 313.
Kumarappan, V., M. Krishnamurthy, and D. Mathur, 2001, Phys. Rev. Lett. **87**, 085005.
Kumarappan, V., M. Krishnamurthy, and D. Mathur, 2002, Phys. Rev. A **66**, 033203.
Kumarappan, V., M. Krishnamurthy, and D. Mathur, 2003a, Phys. Rev. A **67**, 043204.
Kumarappan, V., M. Krishnamurthy, and D. Mathur, 2003b, Phys. Rev. A **67**, 063207.

Kümmel, S., and L. Kronik, 2008, Rev. Mod. Phys. **80**, 3.
Kundu, M., and D. Bauer, 2006, Phys. Rev. Lett. **96**, 123401.
Laarmann, T., A. R. B. de Castro, P. Gürtler, W. Laasch, J. Schulz, H. Wabnitz, and T. Möller, 2004, Phys. Rev. Lett. **92**, 143401.
Lamour, E., C. Prigent, J. P. Rozet, and D. Vernhet, 2005, Nucl. Instrum. Methods Phys. Res. B **235**, 408.
Lamour, E., C. Prigent, J. P. Rozet, and D. Vernhet, 2007, J. Phys.: Conf. Ser. **88**, 012035.
Larsson, J., and A. Sjögren, 1999, Rev. Sci. Instrum. **70**, 2253.
Last, I., and J. Jortner, 1998, Phys. Rev. A **58**, 3826.
Last, I., and J. Jortner, 1999, Phys. Rev. A **60**, 2215.
Last, I., and J. Jortner, 2000, Phys. Rev. A **62**, 013201.
Last, I., and J. Jortner, 2001, Phys. Rev. A **64**, 063201.
Last, I., I. Schek, and J. Jortner, 1997, J. Chem. Phys. **107**, 6685.
Lebeault, M. A., J. Viallon, J. Chevaleyre, C. Ellert, D. Normand, M. Schmidt, O. Sublemontier, C. Guet, and B. Huber, 2002, Eur. Phys. J. D **20**, 233.
Ledingham, K. W. D., P. McKenna, and R. P. Singhal, 2003, Science **300**, 1107.
Legrand, C., E. Suraud, and P.-G. Reinhard, 2002, J. Phys. B **35**, 1115.
Leisner, T., K. Athanassenas, O. Echt, O. Kandler, D. Kreisle, and E. Recknagel, 1991, Z. Phys. D: At., Mol. Clusters **20**, 127.
Leopold, D. G., J. Ho, and W. C. Lineberger, 1987, J. Chem. Phys. **86**, 1715.
Lezius, M., S. Dobosz, D. Normand, and M. Schmidt, 1997, J. Phys. B **30**, L251.
Lezius, M., S. Dobosz, D. Normand, and M. Schmidt, 1998, Phys. Rev. Lett. **80**, 261.
Li, J., X. Li, H.-J. Zhai, and L.-S. Wang, 2003, Science **299**, 864.
Li, S. H., C. Wang, J. S. Liu, P. P. Zhu, X. W. Wang, G. Q. Ni, R. X. Li, and Z. Z. Xu, 2005, Plasma Sci. Technol. **7**, 2684.
Li, S. H., C. Wang, P. P. Zhu, X. X. Wang, R. X. Li, G. Q. Ni, and Z. Z. Xu, 2003, Chin. Phys. Lett. **20**, 1247.
Lifschitz, E. M., and L. P. Pitajewski, 1988, *Physikalische Kinetik*, Lehrbuch der Theoretischen Physik Vol. 10 (Mir, Moscow).
Lin, Z. Q., J. Zhang, Y. J. Li, L. M. Chen, T. Z. Lu, H. Teng, B. Y. Man, and L. Z. Zhao, 2001, Chin. Phys. Lett. **18**, 211.
Liseykina, T. V., S. Pirner, and D. Bauer, 2010, Phys. Rev. Lett. **104**, 095002.
Loch, S. D., M. S. Pindzola, and D. C. Griffin, 2008, Int. J. Mass. Spectrom. **271**, 68.
Lotz, W., 1967, Z. Phys. **206**, 205.
Madison, K. W., P. K. Patel, D. Price, A. Edens, M. Allen, T. E. Cowan, J. Zweiback, and T. Ditmire, 2004, Phys. Plasmas **11**, 270.
Maine, P., D. Strickland, P. Bado, M. Pessot, and G. Mourou, 1988, IEEE J. Quantum Electron. **24**, 398.
Marques, M. A. L., C. Ullrich, F. Nogueira, A. Rubio, K. Burke, and E. K. U. Gross, 2006, Eds., *Time-Dependent Density-Functional Theory*, Lectures Notes in Physics Vol. 706 (Springer, Berlin).
Martchenko, T., C. Siedschlag, S. Zamith, H. G. Muller, and M. J. J. Vrakking, 2005, Phys. Rev. A **72**, 053202.
Martin, T. P., 1996, Phys. Rep. **273**, 199.
Mathur, D., and M. Krishnamurthy, 2006, Laser Phys. **16**, 581.
Matveev, A. V., K. M. Neyman, G. Pacchioni, and N. Rösch, 1999, Chem. Phys. Lett. **299**, 603.
Mayer, C., R. Palkovits, G. Bauer, and T. Schalkhammer, 2001, J. Nanopart. Res. **3**, 361.
McHugh, K. M., J. G. Eaton, G. H. Lee, H. W. Sarkas, L. H. Kidder, J. T. Snodgrass, M. R. Manaa, and K. H. Bowen, 1989, J. Chem. Phys. **91**, 3792.
McPherson, A., T. S. Luk, B. D. Thompson, K. Boyer, and C. K. Rhodes, 1993, Appl. Phys. B: Lasers Opt. **57**, 337.
McPherson, A., B. D. Thompson, A. B. Borisov, K. Boyer, and C. K. Rhodes, 1994, Nature (London) **370**, 631.
Megi, F., M. Belkacem, M. A. Bouchene, E. Suraud, and G. Zwicknagel, 2003, J. Phys. B **36**, 273.
Meiwes-Broer, K.-H., 2000, Ed., *Metal Clusters at Surfaces* (Springer, Berlin).
Meiwes-Broer, K.-H., 2006, Ed., *Clusters at Surfaces: Electronic Properties and Magnetism*, special issue of Appl. Phys. A **82**.
Meiwes-Broer, K.-H., and R. Berndt, 2007, Eds., *Atomic Clustes at Surfaces and in Thin Films*, special issue of Eur. Phys. J. D **45**.
Mendham, K. J., N. Hay, M. B. Mason, J. W. G. Tisch, and J. P. Marangos, 2001, Phys. Rev. A **64**, 055201.
Methling, R.-P., V. Senz, E.-D. Klinkenberg, T. Diederich, J. Tiggesbäumker, G. Holzhüter, J. Bansmann, and K.-H. Meiwes-Broer, 2001, Eur. Phys. J. D **16**, 173.
Micheau, S., C. Bonté, F. Dorchies, C. Fourment, M. Harmand, H. Jouin, O. Peyrusse, B. Pons, and J. J. Santos, 2007, High Energy Density Phys. **3**, 191.
Mie, G., 1908, Ann. Phys. (Leipzig) **330**, 377.
Mikaberidze, A., U. Saalmann, and J. M. Rost, 2008, Phys. Rev. A **77**, 041201(R).
Milani, P., and S. Ianotta, 1999, *Cluster Beam Synthesis of Nanostructured Materials*, Springer Series in Cluster Physics (Springer, Berlin).
Milchberg, H. M., S. J. McNaught, and E. Parra, 2001, Phys. Rev. E **64**, 056402.
Milonni, P. W., and J. H. Eberly, 1988, *Lasers* (Wiley, New York).
Miura, E., H. Honda, K. Katsura, E. Takahashi, and K. Kondo, 2001, Jpn. J. Appl. Phys., Part 1 **40**, 7067.
Moore, A. S., K. J. Mendham, D. R. Symes, J. S. Robinson, E. Springate, M. B. Mason, R. A. Smith, J. W. G. Tisch, and J. P. Marangos, 2005, Appl. Phys. B: Lasers Opt. **80**, 101.
Moseler, M., B. Huber, H. Häkkinen, U. Landman, G. Wrigge, M. A. Hoffmann, and B. v. Issendorff, 2003, Phys. Rev. B **68**, 165413.
Mulser, P., M. Kanapathipillai, and D. H. H. Hoffmann, 2005, Phys. Rev. Lett. **95**, 103401.
Mundt, M., and S. Kümmel, 2007, Phys. Rev. B **76**, 035413.
Mundt, M., S. Kümmel, B. Huber, and M. Moseler, 2006, Phys. Rev. B **73**, 205407.
Nabekawa, Y., H. Hasegawa, E. J. Takahashi, and K. Midorikawa, 2005, Phys. Rev. Lett. **94**, 043001.
Näher, U., S. Björnholm, S. Frauendorf, F. Garcias, and C. Guet, 1997, Phys. Rep. **285**, 245.
Nakatsukasa, T., K. Yabana, and G. F. Bertsch, 2002, Phys. Rev. A **65**, 032512.
Needs, R. J., P. R. C. Kent, A. R. Porter, M. D. Towler, and G. Rajagopal, 2002, Int. J. Quantum Chem. **86**, 218.
Nest, M., T. Klamroth, and P. Saalfrank, 2005, J. Chem. Phys. **122**, 124102.
Neutze, R., R. Wouts, D. van der Spoel, E. Weckert, and J. Hajdu, 2000, Nature (London) **406**, 752.
Niemietz, M., M. Engelke, Y. D. Kim, and G. Ganteför, 2007, Phys. Rev. B **75**, 085438.
Nishihara, K., H. Amitani, M. Murakami, S. V. Bulanov, and T.

Z. Esirkepov, 2001, Nucl. Instrum. Methods Phys. Res. A **464**, 98.
Ouacha, H., C. Hendrich, F. Hubenthal, and F. Träger, 2005, Appl. Phys. B: Lasers Opt. **81**, 663.
Pai, C. H., C. C. Kuo, M. W. Lin, J. P. Wang, and S. Y. Chen, 2006, Opt. Lett. **31**, 984.
Papadogiannis, N. A., B. Witzel, C. C. Kalpouzos, and D. Charalambidis, 1999, Phys. Rev. Lett. **83**, 4289.
Parker, J., K. T. Taylor, C. W. Clark, and S. Blodgett-Ford, 1996, J. Phys. B **29**, L33.
Parker, J. S., B. J. S. Doherty, K. J. Meharg, and K. T. Taylor, 2003, J. Phys. B **36**, L393.
Parra, E., I. Alexeev, J. Fan, K. Y. Kim, S. J. McNaught, and H. M. Milchberg, 2000, Phys. Rev. E **62**, R5931.
Passig, J., K.-H. Meiwes-Broer, and J. Tiggesbäumker, 2006, Rev. Sci. Instrum. **77**, 093304.
Pauly, H., 2000, *Atom, Molecule and Cluster Beams 2* (Springer, Berlin).
Peano, F., J. L. Martins, R. A. Fonseca, L. O. Silva, G. Coppa, F. Peinetti, and R. Mulas, 2007, Phys. Plasmas **14**, 056704.
Peano, F., F. Peinetti, R. Mulas, G. Coppa, and L. O. Silva, 2006, Phys. Rev. Lett. **96**, 175002.
Perdew, J. P., K. Burke, and M. Ernzerhof, 1996, Phys. Rev. Lett. **77**, 3865.
Perdew, J. P., and Y. Wang, 1992, Phys. Rev. B **45**, 13244.
Peredkov, S., *et al.*, 2007a, Phys. Rev. B **75**, 235407.
Peredkov, S., *et al.*, 2007b, Phys. Rev. B **76**, 081402(R).
Perner, M., S. Gresillon, J. März, G. von Plessen, J. Feldmann, J. Porstendorfer, K.-J. Berg, and G. Berg, 2000, Phys. Rev. Lett. **85**, 792.
Petrov, G. M., and J. Davis, 2008, Phys. Plasmas **15**, 056705.
Pettiette, C. L., S. H. Yang, M. J. Craycraft, J. Conceicao, R. T. Laaksonen, O. Cheshnovsky, and R. E. Smalley, 1988, J. Chem. Phys. **88**, 5377.
Pfalzner, S., and P. Gibbon, 1996, *Many-Body Tree Methods in Physics* (Cambrigde University Press, Cambridge).
Pinaré, J. C., B. Baguenard, C. Bordas, and M. Broyer, 1999, Eur. Phys. J. D **9**, 21.
Pinchuk, A., A. Hilger, G. von Plessen, and U. Kreibig, 2004, Nanotechnology **15**, 1890.
Pines, D., and P. Nozières, 1966, *The Theory of Quantum Liquids* (Benjamin, New York).
Plagne, L., J. Daligault, K. Yabana, T. Tazawa, Y. Abe, and C. Guet, 2000, Phys. Rev. A **61**, 033201.
Pohl, A., P.-G. Reinhard, and E. Suraud, 2000, Phys. Rev. Lett. **84**, 5090.
Pohl, A., P.-G. Reinhard, and E. Suraud, 2001, J. Phys. B **34**, 4969.
Pohl, A., P.-G. Reinhard, and E. Suraud, 2003, Phys. Rev. A **68**, 053202.
Pohl, A., P.-G. Reinhard, and E. Suraud, 2004a, J. Phys. B **37**, 3301.
Pohl, A., P.-G. Reinhard, and E. Suraud, 2004b, Phys. Rev. A **70**, 023202.
Popruzhenko, S. V., M. Kundu, D. F. Zaretsky, and D. Bauer, 2008, Phys. Rev. A **77**, 063201.
Portales, H., L. Saviot, E. Duva, M. Fujii, S. Hayashi, N. D. Fatti, and F. Vallée, 2001, J. Chem. Phys. **115**, 3444.
Press, W. H., S. A. Teukolsky, W. T. Vetterling, and B. P. Flannery, 1992, *Numerical Recipes* (Cambridge University Press, Cambridge).
Prigent, C., C. Deiss, E. Lamour, J. P. Rozet, D. Vernhet, and J. Burgdörfer, 2008, Phys. Rev. A **78**, 053201.
Pukhov, A., S. Gordienko, and T. Baeva, 2003, Phys. Rev. Lett. **91**, 173002.
Pukhov, A., and J. Meyer-ter-Vehn, 2002, Appl. Phys. B: Lasers Opt. **74**, 355.
Purnell, J., E. M. Snyder, S. Wei, and A. W. Castleman, Jr., 1994, Chem. Phys. Lett. **229**, 333.
Radcliffe, P., 2004, Ph.D. thesis (Universität Rostock).
Radcliffe, P., T. Döppner, M. Schumacher, S. Teuber, J. Tiggesbäumker, and K.-H. Meiwes-Broer, 2005, Contrib. Plasma Phys. **45**, 424.
Radcliffe, P., A. Przystawik, T. Diederich, T. Döppner, J. Tiggesbäumker, and K.-H. Meiwes-Broer, 2004, Phys. Rev. Lett. **92**, 173403.
Ramunno, L., C. Jungreuthmayer, H. Reinholz, and T. Brabec, 2006, J. Phys. B **39**, 4923.
Rayleigh, J. W. S., 1899, Philos. Mag. **47**, 375.
Reinhard, P.-G., and E. Suraud, 1998, Eur. Phys. J. D **3**, 175.
Reinhard, P.-G., and E. Suraud, 2001, Appl. Phys. B: Lasers Opt. **73**, 401.
Reinhard, P.-G., and E. Suraud, 2003, *Introduction to Cluster Dynamics* (Wiley, New York).
Richardson, H. H., Z. N. Hickman, A. O. Govorov, A. C. Thomas, W. Zhang, and M. E. Kordesch, 2006, Arch. Hist. Exact Sci. **6**, 783.
Rose-Petruck, C., K. J. Schafer, K. R. Wilson, and C. P. J. Barty, 1997, Phys. Rev. A **55**, 1182.
Rozet, J. P., M. Cornille, S. Dobosz, J. Dubau, J. C. Gauthier, S. Jacquemot, E. Lamour, M. Lezius, D. Normand, M. Schmidt, and D. Vernhet, 2001, Phys. Scr., T **T92**, 113.
Rullière, C., 2005, Ed., in *Femtosecond Laser Pulses: Principles and Experiments*, 2nd ed., Advanced Texts in Physics (Springer, New York).
Runge, E., and E. K. U. Gross, 1984, Phys. Rev. Lett. **52**, 997.
Saalmann, U., 2006, J. Mod. Opt. **53**, 173.
Saalmann, U., and J. M. Rost, 2003, Phys. Rev. Lett. **91**, 223401.
Saalmann, U., and J. M. Rost, 2005, Eur. Phys. J. D **36**, 159.
Saalmann, U., and J. M. Rost, 2008, Phys. Rev. Lett. **100**, 133006.
Saalmann, U., and R. Schmidt, 1996, Z. Phys. D: At., Mol. Clusters **38**, 153.
Saalmann, U., C. Siedschlag, and J. M. Rost, 2006, J. Phys. B **39**, R39.
Sakabe, S., M. Hashida, and S. Shimizu, 2006, Mod. Las. Phys. **16**, 551.
Sakabe, S., S. Shimizu, M. Hashida, F. Sato, T. Tsuyukushi, K. Nishihara, S. Okihara, T. Kagawa, Y. Izawa, K. Imasaki, and T. Iida, 2004, Phys. Rev. A **69**, 023203.
Santra, R., and C. H. Greene, 2003, Phys. Rev. Lett. **91**, 233401.
Saugout, S., C. Cornaggia, A. Suzor-Weiner, and E. Charron, 2007, Phys. Rev. Lett. **98**, 253003.
Schaadt, D. M., B. Feng, and E. T. Yu, 2005, Appl. Phys. Lett. **86**, 063106.
Schlegel, H. B., S. M. Smith, and X. S. Li, 2007, J. Chem. Phys. **126**, 244110.
Schlipper, R., R. Kusche, B. v. Issendorff, and H. Haberland, 2001, Appl. Phys. A: Mater. Sci. Process. **72**, 255.
Schmidt, M., and H. Haberland, 1999, Eur. Phys. J. D **6**, 109.
Schmidt, R., H. O. Lutz, and R. Dreizler, 1992, Eds., *Nuclear Physics Concepts in the Study of Atomic Physics* (Springer, Berlin).
Schroeder, W. A., T. R. Nelson, A. B. Borisov, J. W. Long-

worth, K. Boyer, and C. K. Rhodes, 2001, J. Phys. B **34**, 297.
Schroeder, W. A., F. G. Omenetto, A. B. Borisov, J. W. Longworth, A. McPherson, C. Jordan, K. Boyer, K. Kondo, and C. K. Rhodes, 1998, J. Phys. B **31**, 5031.
Schumacher, M., S. Teuber, L. Köller, J. Köhn, J. Tiggesbäumker, and K.-H. Meiwes-Broer, 1999, Eur. Phys. J. D **9**, 411.
Seideman, T., M. Y. Ivanov, and P. B. Corkum, 1995, Phys. Rev. Lett. **75**, 2819.
Senz, V., *et al.*, 2009, Phys. Rev. Lett. **102**, 138303.
Serra, L., and A. Rubio, 1997, Phys. Rev. Lett. **78**, 1428.
Serra, L. I., F. Garcias, M. Barranco, J. Navarro, and N. Van-Giai, 1991, Z. Phys. D: At., Mol. Clusters **20**, 277.
Shao, Y. L., T. Ditmire, J. W. G. Tisch, E. Springate, J. P. Marangos, and M. H. R. Hutchinson, 1996, Phys. Rev. Lett. **77**, 3343.
Siedschlag, C., and J. M. Rost, 2002, Phys. Rev. Lett. **89**, 173401.
Siedschlag, C., and J. M. Rost, 2003, Phys. Rev. A **67**, 013404.
Siedschlag, C., and J. M. Rost, 2004, Phys. Rev. Lett. **93**, 043402.
Siedschlag, C., and J. M. Rost, 2005, Phys. Rev. A **71**, 031401(R).
Siekmann, H. R., E. Holub-Krappe, B. Wrenger, C. Pettenkofer, and K.-H. Meiwes-Broer, 1993, Z. Phys. B: Condens. Matter **90**, 201.
Siekmann, H. R., C. Lüder, J. Faehrmann, H. O. Lutz, and K.-H. Meiwes-Broer, 1991, Z. Phys. D: At., Mol. Clusters **20**, 417.
Simberg, D., T. Duza, J. H. Park, M. Essler, J. Pilch, L. Zhang, A. M. Derfus, M. Yang, R. M. Hoffman, S. Bhatia, M. J. Sailor, and E. Ruoslaht, 2007, Proc. Natl. Acad. Sci. U.S.A. **104**, 932.
Skobelev, I. Y., *et al.*, 2002, J. Exp. Theor. Phys. **94**, 966.
Skruszewicz, S., J. Passig, A. Przystawik, J. Tiggesbäumker, and K.-H. Meiwes-Broer, 2009, unpublished.
Snyder, E. M., S. A. Buzza, and A. W. Castleman, Jr., 1996, Phys. Rev. Lett. **77**, 3347.
Spielmann, C., N. H. Burnett, S. Sartania, R. Koppitsch, M. Schnürer, C. Kan, M. Lenzner, P. Wobrauschek, and F. Krausz, 1997, Science **278**, 661.
Spitzer, L., 1956, *Physics of Fully Ionized Gases* (Interscience, New York).
Springate, E., S. A. Aseyev, S. Zamith, and M. J. J. Vrakking, 2003, Phys. Rev. A **68**, 053201.
Springate, E., N. Hay, J. W. G. Tisch, M. B. Mason, T. Ditmire, M. H. R. Hutchinson, and J. P. Marangos, 2000a, Phys. Rev. A **61**, 063201.
Springate, E., N. Hay, J. W. G. Tisch, M. B. Mason, T. Ditmire, J. P. Marangos, and M. H. R. Hutchinson, 2000b, Phys. Rev. A **61**, 044101.
Stanzel, J., F. Burmeister, M. Neeb, W. Eberhardt, R. Mitrić, C. Bürgel, and V. Bonačić-Koutecký, 2007, J. Chem. Phys. **127**, 164312.
Strickland, D., and G. Mourou, 1985, Opt. Commun. **56**, 219.
Stuik, R., E. Louis, A. E. Yakshin, P. C. Görts, E. L. G. Maas, F. Bijkerk, D. Schmitz, F. Scholze, G. Ulm, and M. Haidl, 1999, J. Vac. Sci. Technol. B **17**, 2998.
Sugano, S., and H. Koizumi, 1998, *Microcluster Physics* (Springer, Berlin).
Sukiasyan, S., C. McDonald, C. Van Vlack, C. Destefani, T. Fennel, M. Ivanov, and T. Brabec, 2009, Phys. Rev. A **80**, 013412.
Suraud, E., and P.-G. Reinhard, 2000, Phys. Rev. Lett. **85**, 2296.
Suzuki, T., 2006, Annu. Rev. Phys. Chem. **57**, 555.
Szasz, L., 1985, *Pseudopotential Theory of Atoms and Molecules* (Wiley, New York).
Taguchi, T., T. M. Antonsen, Jr., and H. M. Milchberg, 2004, Phys. Rev. Lett. **92**, 205003.
Tajima, T., Y. Kishimoto, and M. C. Downer, 1999, Phys. Plasmas **6**, 3759.
Tannor, D. J., R. Kosloff, and S. A. Rice, 1986, J. Chem. Phys. **85**, 5805.
Taylor, K. J., C. L. Pettiette-Hall, O. Cheshnovsky, and R. E. Smalley, 1992, J. Chem. Phys. **96**, 3319.
Tchaplyguine, M., R. R. Marinho, M. Gisselbrecht, J. Schulz, N. Mårtensson, S. L. Sorensen, A. N. de Brito, R. Feifel, G. Öhrwall, M. Lundwall, S. Svensson, and O. Björneholm, 2004, J. Chem. Phys. **120**, 345.
Tchaplyguine, M., *et al.*, 2007, Eur. Phys. J. D **45**, 295.
Teuber, S., T. Döppner, T. Fennel, J. Tiggesbäumker, and K.-H. Meiwes-Broer, 2001, Eur. Phys. J. D **16**, 59.
Thomas, L. H., 1927, Proc. Cambridge Philos. Soc. **23**, 542.
Thomson, J. J., 1907, Philos. Mag. **13**, 561.
Tiedtke, K., A. Azima, N. von Bargen, L. Bittner, S. Bonfigt, S. Düsterer, B. Faatz, U. Frühling, M. Gensch, Ch. Gerth, N. Guerassimova, U. Hahn, T. Hans, M. Hesse, K. Honkavaar, U. Jastrow, P. Juranic, S. Kapitzki, B. Keitel, T. Kracht, M. Kuhlmann, W. B. Li, M. Martins, T. Núñez, E. Plönjes, H. Redlin, E. L. Saldin, E. A. Schneidmiller, J. R. Schneider, S. Schreiber, N. Stojanovic, F. Tavella, S. Toleikis, R. Treusch, H. Weigelt, M. Wellhöfer, H. Wabnitz, M. V. Yurkov, and J. Feldhaus, 2009, New J. Phys. **11**, 023029.
Tiggesbäumker, J., L. Köller, and K.-H. Meiwes-Broer, 1996, Chem. Phys. Lett. **260**, 428.
Tiggesbäumker, J., L. Köller, K.-H. Meiwes-Broer, and A. Liebsch, 1993, Phys. Rev. A **48**, R1749.
Tiggesbäumker, J., and F. Stienkemeier, 2007, Phys. Chem. Chem. Phys. **9**, 4748.
Tisch, J. W. G., 2000, Phys. Rev. A **62**, 041802(R).
Tisch, J. W. G., T. Ditmire, D. J. Fraser, N. Hay, M. B. Mason, E. Springate, J. P. Marangos, and M. H. R. Hutchinson, 1997, J. Phys. B **30**, L709.
Tisch, J. W. G., N. Hay, K. J. Mendham, E. Springate, D. R. Symes, A. J. Comley, M. B. Mason, E. T. Gumbrell, T. Ditmire, R. A. Smith, J. P. Marangos, and M. H. R. Hutchinson, 2003, Nucl. Instrum. Methods Phys. Res. B **205**, 310.
Toma, E. S., and H. G. Muller, 2002, Phys. Rev. A **66**, 013204.
Trebino, R., 2002, *Frequency-Resolved Optical Gating: The Measurement of Ultrashort Laser Pulses* (Kluwer, Dordrecht).
Truong, N. X., P. Hilse, S. Göde, A. Przystawik, T. Döppner, Th. Fennel, Th. Bornath, J. Tiggesbäumker, M. Schlanges, G. Gerber, and K. H. Meiwes-Broer, 2010, Phys. Rev. A **81**, 013201.
Uehling, E. A., and G. E. Uhlenbeck, 1933, Phys. Rev. A **43**, 552.
Ullrich, C. A., P.-G. Reinhard, and E. Suraud, 1997, J. Phys. B **30**, 5043.
Varin, C., and M. Piche, 2006, Phys. Rev. E **74**, 045602(R).
Velotta, R., N. Hay, M. B. Mason, M. Castillejo, and J. P. Marangos, 2001, Phys. Rev. Lett. **87**, 183901.
Véniard, V., R. Taïeb, and A. Maquet, 2001, Phys. Rev. A **65**, 013202.
Verlet, J. R. R., A. E. Bragg, A. Kammrath, O. Cheshnovsky, and D. M. Neumark, 2004, J. Chem. Phys. **121**, 10015.
Verma, K. K., J. T. Bahns, A. R. Rajaei-Rizi, W. C. Stwalley,

and W. T. Zemke, 1983, J. Chem. Phys. **78**, 3599.
von Pietrowski, R., K. von Haeften, T. Laarmann, T. Möller, L. Museur, and A. V. Kanaev, 2006, Eur. Phys. J. D **38**, 323.
Vozzi, C., M. Nisoli, J. P. Caumes, G. Sansone, S. Stagira, S. De-Silvestri, M. Vecchiocattivi, D. Bassi, M. Pascolini, L. Poletto, P. Villoresi, and G. Tondello, 2005, Appl. Phys. Lett. **86**, 111121.
Wabnitz, H., *et al.*, 2002, Nature (London) **420**, 482.
Wahlström, C. G., J. Larsson, A. Persson, T. Starczewski, S. Svanberg, P. Salières, P. Balcou, and A. L. Huillier, 1993, Phys. Rev. A **48**, 4709.
Walker, B., B. Sheehy, K. C. Kulander, and L. F. DiMauro, 1996, Phys. Rev. Lett. **77**, 5031.
Walter, M., H. Häkkinen, J. Stanzel, M. Neeb, and W. Eberhardt, 2007, Phys. Rev. B **76**, 155422
Weast, R. C., 1988, *Handbook of Chemistry and Physics* (CRC, Boca Raton, FL).
Weiner, A. M., 2000, Rev. Sci. Instrum. **71**, 1929.
Weisgerber, S., and P.-G. Reinhard, 1992, Z. Phys. D: At., Mol. Clusters **23**, 275.
Weissbluth, M., 1978, *Atoms and Molecules* (Academic, San Diego).
Weisskopf, V., 1937, Phys. Rev. **52**, 295.
Wenzel, T., J. Bosbach, A. Goldmann, and F. Träger, 1999, Appl. Phys. B: Lasers Opt. **69**, 513.
Wertheim, G. K., 1989, Z. Phys. D: At., Mol. Clusters **12**, 319.
Whaley, K. B., and R. E. Miller, 2001, Eds., *Helium Nanodroplets: A Novel Medium for Chemistry and Physic*, special issue of J. Chem. Phys. **115**.
Wörner, J., V. Guzielski, J. Staplefeld, and T. Möller, 1989, Chem. Phys. Lett. **159**, 321.
Wrigge, G., M. A. Hoffmann, and B. v. Issendorff, 2002, Phys. Rev. A **65**, 063201.
Wu, B., and A. Kumar, 2007, J. Vac. Sci. Technol. B **25**, 1743.
Yabana, K., and G. F. Bertsch, 1996, Phys. Rev. B **54**, 4484.
Yannouleas, C., J. M. Pacheco, and R. A. Broglia, 1990, Phys. Rev. B **41**, 6088.
Zamith, S., T. Martchenko, Y. Ni, S. A. Aseyev, H. G. Muller, and M. J. J. Vrakking, 2004, Phys. Rev. A **70**, 011201(R).
Zewail, A. H., 1980, Phys. Today **33** (11), 27.
Zewail, A. H., 1994, *Femtochemistry* (World Scientific, Singapore), Vols. I and II.
Ziaja, B., T. Laarmann, H. Wabnitz, F. Wang, E. Weckert, C. Bostedt, and T. Möller, 2009, New J. Phys. **11**, 103012.
Ziaja, B., E. Weckert, and T. Möller, 2007, Laser Part. Beams **25**, 407.
Ziegler, T., C. Hendrich, F. Hubenthal, T. Vartanyan, and F. Träger, 2004, Chem. Phys. Lett. **386**, 319.
Zuo, T., and A. D. Bandrauk, 1995, Phys. Rev. A **52**, R2511.
Zweiback, J., T. E. Cowan, J. H. Hartley, R. Howell, K. B. Wharton, J. K. Crane, V. P. Yanovsky, G. Hays, R. A. Smith, and T. Ditmire, 2002, Phys. Plasmas **9**, 3108.
Zweiback, J., T. E. Cowan, R. A. Smith, J. H. Hartley, R. Howell, C. A. Steinke, G. Hays, K. B. Wharton, J. K. Crane, and T. Ditmire, 2000, Phys. Rev. Lett. **85**, 3640.
Zweiback, J., T. Ditmire, and M. D. Perry, 1999, Phys. Rev. A **59**, R3166.